Concept Study of an Electrical Variable Transmission for Off-Highway Applications

Steven Vanhee

Supervisors: Prof. dr. ir. Peter Sergeant, Ir. Thomas Vyncke (Dana-Spicer)
Counsellor: Joachim Druant

Master's dissertation submitted in order to obtain the academic degree of
Master of Science in Electromechanical Engineering

Department of Industrial Technology and Construction
Chairman: Prof. Marc Vanhaelst
Faculty of Engineering and Architecture
Academic year 2014-2015

UNIVERSITEIT GENT

CONFIDENTIAL UP TO AND INCLUDING 12/31/2024
IMPORTANT

Concept Study of an Electrical Variable Transmission for Off-Highway Applications

Steven Vanhee

Supervisors: Prof. dr. ir. Peter Sergeant, Ir. Thomas Vyncke (Dana-Spicer)
Counsellor: Joachim Druant

Master's dissertation submitted in order to obtain the academic degree of
Master of Science in Electromechanical Engineering

Department of Industrial Technology and Construction
Chairman: Prof. Marc Vanhaelst
Faculty of Engineering and Architecture
Academic year 2014-2015

UNIVERSITEIT GENT

Preface

A master thesis is the biggest challenge as a graduate student and a gateway to start a career in both the academic or the industrial sector. As a student in electromechanical engineering, I always pursued getting a compete and broad view of electrical power systems. During my exchange with Grenoble INP, I mainly focussed on electrical power transmission systems. Back in Belgium, I wanted to broaden my expertise of electrical applications. I joined Infrabel to study the influence of catenary voltage decreasing on the overall energy consumption of the Belgian railway system. Due to this internship, I am aware that -apart form energy- transportation is one of the big challenges in our society. Consequently, a master thesis combining energy and transportation was an evident choice. Moreover, since I grew up on a farm, where I gained many practical experiences with off-highway machinery, I got even more curious about studying the technology behind it.

This master thesis was done in corporation with Dana-Spicer, one of world's biggest producers of transmission systems. Dana is an US-based company with a corporate R&D-center in Bruges. One of the goals of this center is to increase revenue by innovation in off-highway vehicle markets such as tractors, cranes, fork lift trucks, etc. Conventional off-highway transmission systems include a hydraulic torque converter and a gearbox with a maximum overall efficiency of about 85 %. However, depending on the operating point, this can be significantly lower. The lower global efficiency of conventional drivetrains leads Dana to alternative concepts such as the replacement of the inefficient torque converter by a more efficient electrical device, the Electrical Variable Transmission (EVT). This device allows to decouple the rotational speed of the Internal Combustion Engine (ICE) and the wheels. Next to the increased efficiency of electrical devices over hydraulic devices, the infinite number of transmission ratios permits the ICE to work in a better operating point resulting in a significant reduced fuel consumption.

In this master thesis, I investigate the possibility of integrating the electromagnetic torque converter in off-highway transmissions. In particular, I study fuel savings compared to classical hydraulic torque converters. The study of transmission systems was meant to be very short, but rapidly enlarged, since I found a lot of interesting concepts. Furthermore, I met very soon the divergence between the theoretical model and the finite element model, which was one of the biggest challenges to overcome during this work. At last, I believe that the design of an electrical torque converter was the most interesting part of my study, since it is closely connected to practical implementation and numerous results are obtained.

First of all, I want to thank Ir. Joachim Druant, my counsellor, for both the technical and modelling advise he gave me. Although it was his first experience as a counsellor, I believe he did an excellent job. Secondly, I'm thankful to Prof. Dr. Ir. Peter Sergeant and Dr. Ir. Thomas Vyncke, supervisors

of this master thesis. I especially want to thank Prof. Sergeant for the numerous advices he gave me and to provide me access to the computer in his laboratory. Additionally, I thank Mr. Vyncke, currently working at Dana-Spicer, for the real torque converter data, which is the basis of this feasibility study. Subsequently, I am very thankful to my girlfriend, Céline, for the support during the last five years at Ghent University and for the proofreading of this master thesis. Furthermore, I am grateful to my colleges at EELAB. Emile, Thibaut, Thomas: thanks for the nice atmosphere at the lab. Moreover, your little tips and tricks saved me a lot of time. Finally, I want to thank my family who has always been supporting me during my studies and who made it possible in the first place that I am where I am now.

Steven Vanhee, 22 May 2015

Concept Study of an Electrical Variable Transmission for Off-Highway Applications

Steven Vanhee

Master's dissertation submitted in order to obtain the academic degree of
Master of Science in Electromechanical Engineering

Supervisors: Prof. Dr. Ir. Peter Sergeant, Dr. Ir. Thomas Vyncke
Counsellor: Ir. Joachim Druant

Department of Industrial Technology and Construction
Chairman: Prof. Dr. Ir. Mark Vanhaelst
Faculty of Engineering and Architecture, Ghent University (UGent)
Academic year 2014-2015

Summary

The design of an induction machine (IM) based electrical variable transmission (EVT) is considered in this work. The first part of this paper is dedicated to transmission systems. It is shown that power-split continuous variable transmission (PS-CVT) systems have several advantages over conventional gearbox systems. Chapter 3 introduces multiple electromagnetic PS-CVT systems, including the IM-based EVT. Although an IM-based EVT requires rotor slip rings, it only consists of two airgaps which is the principal advantage over other EVT systems. Moreover, cage machines are relatively cheap and robust compared to their PM equivalents.

After a short introduction to FE modelling in Chapter 4, Chapter 5 composes a coupled-circuit FE model of an IM-based EVT with parametrized geometry. Chapters 6 and 7 describe a geometrical optimization and operational analysis of a 9 kW IM-based EVT. It is shown that the rated power of the converters is halved compared to a serial electrical machine connection. Furthermore, although the fixed stator topology has the most simple design, the use of the moving stator topology increases the electromagnetic efficiency of the device by a few percent. Moreover, geometrical dependency of the efficiency is reduced and the electromagnetic power limit is increased by 20 % for the moving stator topology.

In Chapter 8, the feasibility of an electrical torque converter in a real transmission system model is studied. After a geometrical optimization, it is concluded that the maximum electromagnetic efficiency is about 95 %. Since three dimensional effects, skin effects, eddy currents and mechanical and ventilation losses are neglected, the real efficiency of the device could be a few present lower. In the second part of Chapter 8, an operational analysis concludes that the rated power of an air-cooled EVT is 120 kW. Although cooling methods are not studied in this paper, the rated power can be increased to more than 250 kW, if an appropriate water-cooled system is designed. In the last part of the chapter, the EVT is integrated into an existing transmission system. It is shown that even without changes to the gearbox, the global torque converter efficiency increases with 10 %. Moreover, since the EVT enables to reduce speed at partial load, fuel consumption is significantly reduced, to more than 20 % for the studied transmission system.

Overall, it is concluded that an electrical torque converter is a very feasible adaptation in off-highway transmission systems. Although much more research is required, the results of this first study are very positive.

Keywords: Electrical Variable Transmission, electric torque converter, hydraulic torque converter, Power-Split transmissions, finite elements, field oriented control, fuel savings, efficiency

Concept Study of an Electrical Variable Transmission for Off-Highway Applications

Steven Vanhee, Peter Sergeant, Joachim Druant, and Thomas Vyncke
Dept. Electrical Energy, Systems & Automation, Ghent University, B-9000 Ghent, Belgium

***Abstract*—The increasing pressure on fuel prices and greenhouse gas emissions leads transmission system constructors to new alternatives to decrease fuel consumption. Connected between the internal combustion engine (ICE) and the gearbox, the hydraulic torque converter (HTC) is the least efficient part of conventional off-highway transmission systems. An electrical variable transmission (EVT) used as a torque converter seems a prospective device to increase overall efficiency such vehicles. In this article, the design of EVT is optimised using an parametrised 2D quasi-static coupled-circuit finite element model. Using the same model, the efficiency of an EVT both in stand-alone mode and connected to an ICE are analysed. The results of the latter simulations are used to compare the performance of the EVT with a conventional HTC in a five shift off-highway vehicle. The simulations reveal that the size of the electrical converters of the EVT is reduced by 80 % compared to a serial electrical machine connection. More over, the EVT increases the torque converter efficiency by 10 %. Additionally, this paper concludes that the EVT significantly decreases engine torque ripple and leads to 20 % fuel savings due to the more optimal use of the ICE.**

***Index Terms*—electrical variable transmission, off-highway, electromechanical torque converter, hydraulic torque converter, power-split transmissions, finite elements, field oriented torque control, fuel savings, efficiency**

I. Introduction

Conventional off-highway transmission systems are characterized by a serial connection of an internal combustion engine (ICE), a hydraulic torque converter (HTC) and a gearbox connected to the wheel shaft as denoted in **Fig. 1**. The torque converter takes the place of a mechanical clutch in automotive vehicles, allowing the load to be separated from the power source. Although the HTC is a very simple device, its fluid coupling has two main disadvantages: 1) a relatively low efficiency when slip is high, and 2) an uncontrollable speed ratio resulting in a non-optimal engine use. Therefore, the HTC limits the overall efficiency of the drive line [1].

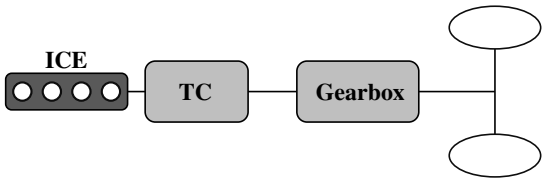

Figure 1: Off-highway powertrain.

Continuously variable transmission (CVT) systems are considered to be the first step in order to increase the overall transmission efficiency. The system enables to decouple the engine speed from the wheel speed and thus permits the ICE to operate in a more efficient working point. Mechanical and hydraulic CVT systems exist for many years. A push-belt CVT with energy storage in a flywheel is analysed in [2]. Paper [3] models and analyses the efficiency of a hydrostatic transmission aimed for off-road multiple axle vehicles. Even though these CVT systems broaden the range of transmission ratios, they suffer from [4, 5]:

- a small power limit, and
- an insufficient system efficiency.

The introduction of a power split (PS) increases both system's efficiency and power limit of conventional CVT systems. A PS-CVT consists of a mechanical power train connected in parallel to a CVT. The basic idea is to send only a part of the power through the CVT, while the remainder is going straight through the mechanical path with high efficiency. Therefore, PS transmissions boost both the efficiency and the power limit of conventional CVT systems [6, 7]. PS-CVTs are already well presented on the market (e.g. Fendt Vario, Dana Rexroth, Toyota Prius...). A commercial hydrostatic PS-CVT is discussed in [1]. The paper shows that depending on the power size, different transmission topologies are to be used. The use of hydrostatic PS-CVTs reduces fuel consumption up to. Nevertheless, the main criticisms for a further introduction of these systems into the off-highway market are robustness, maintenance cost, hydraulic leakage and power density.

The electrical variable transmission presented by [8, 9] is a new kind of PS-CVT system incorporating an electromagnetic-electric power-split and seems a very prospective device to be used as an electromagnetic torque converter. **Fig. 2** presents the lay-out of the system, consisting of an electromagnetic machine with two coupled rotors and two power electronic converters (PECs) with a common DC-bus. The inner rotor is connected to the ICE, whereas the outer rotor is connected to the gearbox. The single squirrel-cage outer rotor significantly increases the power density over other double rotor induction machines [8]. Moreover, the outer rotor cage omits the use of rare earth permanent magnets which reduces material cost. Additionally, the EVT incorporates an inherent overload protection, thanks to the magnetic gearing principle. Finally, the electrical connections offer a first step to introduce hybrid electrical vehicles (HEVs) in the off-highway industry.

In [10, 11], an overview of different EVT topologies can be found. [12]–[14] propose a double layer permanent magnet EVT intended for wind turbine applications. On the one hand, the advantages of a PM outer rotor over a squirrel-cage wind-

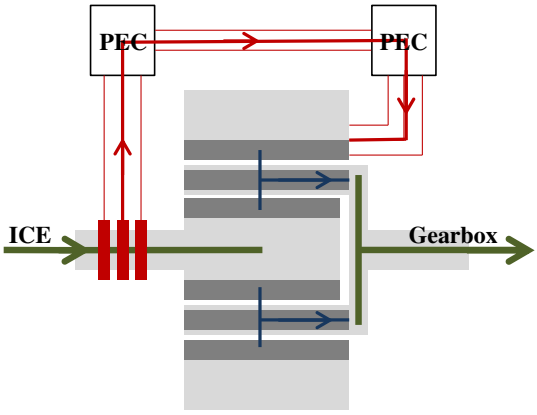

Figure 2: EVT: proposed compact design.

ing are: higher power density, high efficiency and easy control. On the other hand, a PM outer rotor is much more expensive than its induction equivalent, which limits its introduction into the automotive industry. [15]–[17] introduce a magnetic gear integrated PM magnet brushless EVT. The main advantage over other designs is the absence of slip rings, which significantly decreases the maintenance cost. Nevertheless, thanks to the magnetic gearing principle, the machines consist of three air gaps which reduces the overall efficiency. Moreover, the topology requires an auxiliary electrical machine to control the speed of the planetary gear.

In this paper, the EVT shown on **Fig. 2** is studied in detail. A conceptual design procedure focussing on off-highway applications is presented. Based on the magnetic field solutions of a 2D quasi-static coupled-circuit finite element model, the geometry of the device is optimized and efficiency maps are analysed. The goal of the simulations is to compare the performance of an EVT acting as a torque converter in a real off-highway vehicle to its hydraulic equivalent.

II. Working Principle

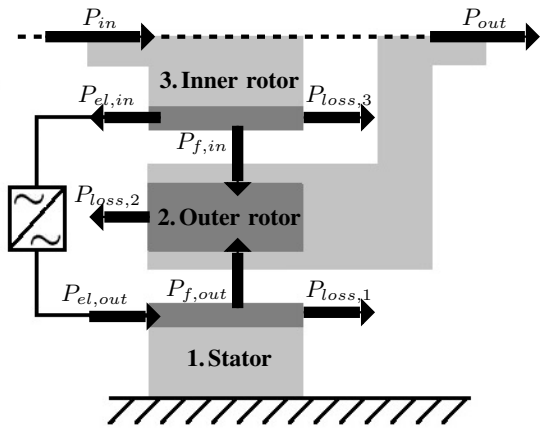

Figure 3: Power flow references in the EVT.

Fig. 3 depicts the power flow references in the EVT. As shown, mechanical power, coming from the ICE, enters the device through the inner rotor.

$$P_{in} = \Omega_{in}\, T_{in} \tag{1}$$

with Ω_{in} and T_{in} the input (rotor) speed and torque respectively. The rotor functions as a power-split device. A part of the power ($P_{el,in}$) leaves the rotor electrically through the converters, another part ($P_{f,in}$) leaves the rotor electromagnetically through the inner air gap, whereas a third part ($P_{loss,3}$) is dissipated due to iron and copper losses:

$$P_{f,in} = \frac{\omega}{p} * T_{in} \tag{2}$$

$$P_{el,in} = \left(\Omega_{in} - \frac{\omega}{p}\right) * T_{in} - P_{loss,3} \tag{3}$$

with ω is the pulsation of the magnetic field and p the number of pole pairs. **Eq.** (**3**) shows that the inner rotor is regarded as an induction machine in generation mode. Neglecting the inner rotor losses, the electrical power fraction is linearly deceasing with the output speed [18].

The PECs are considered to be lossless since their efficiency is very high.

$$P_{el,out} = P_{el,in} \tag{4}$$

Subsequently, the stator receives power from the PECs subtracted by the stator losses ($P_{loss,1}$) and transforms it into electromagnetic power ($P_{f,out}$) by means of its windings:

$$P_{f,out} = P_{el,out} - P_{loss,1} \tag{5}$$

Finally, the inner and the outer air gap power is summed in the outer rotor. The resulting power, subtracted by the outer rotor losses ($P_{loss,2}$), is then transferred to the output shaft of the EVT (P_{out}). Since the two power flows are added at the output shaft, the EVT is classified as an output-coupled power-split transmission [6, 19].

$$P_{out} = P_{f,in} + P_{f,out} - P_{loss,2} \tag{6}$$

III. EVT Circuit Model

Paper [9] derives the voltage equations of a double rotor induction machine in the qd-reference frame rotating with the magnetic field. The article neglects core saturation and slot effects in its model. Other assumptions are:

- A three phase symmetrical machine,
- Sinusoidally distributed windings,
- No skin- or proximity effects, and
- No influence of the slots on the field.

Since this article builds a model in agreement with FE solutions, core saturation is taken into account. Instead of a three winding equivalent model, a six winding model is considered (three windings for each axis). The relation between currents and magnetic fluxes in the machine is given as:

$$\begin{bmatrix} \Psi_{1q} \\ \Psi_{2q} \\ \Psi_{3q} \\ \Psi_{1d} \\ \Psi_{2d} \\ \Psi_{3d} \end{bmatrix} = \begin{bmatrix} L_{11qq} & L_{12qq} & L_{13qq} & L_{11qd} & L_{12qd} & L_{13qd} \\ L_{12qq} & L_{22qq} & L_{23qq} & L_{12qd} & L_{22qd} & L_{23qd} \\ L_{13qq} & L_{23qq} & L_{33qq} & L_{13qd} & L_{23qd} & L_{33qd} \\ L_{11qd} & L_{12qd} & L_{13qd} & L_{11dd} & L_{12dd} & L_{13dd} \\ L_{12qd} & L_{22qd} & L_{23qd} & L_{12dd} & L_{22dd} & L_{23dd} \\ L_{13qd} & L_{23qd} & L_{33qd} & L_{13dd} & L_{23dd} & L_{33dd} \end{bmatrix} \begin{bmatrix} I_{1q} \\ I_{2q} \\ I_{3q} \\ I_{1d} \\ I_{2d} \\ I_{3d} \end{bmatrix} \tag{7a}$$

The subscript 1 is used for the stator quantities, 2 for the outer rotor and 3 for the inner rotor. Ψ_{ij} is the flux linked

with the j-axis of the i-th winding and I_{ij} is the current in the j-axis of the i-th winding. Or similarly:

$$\boldsymbol{\Psi_{123qd}} = \mathsf{L}_{\mathsf{ind}}\ \boldsymbol{I_{123qd}} \tag{7b}$$

with

$$\mathsf{L}_{\mathsf{ind}} = \begin{bmatrix} \mathsf{L}_{\mathsf{qq}} & \mathsf{L}_{\mathsf{qd}} \\ \mathsf{L}_{\mathsf{dq}} & \mathsf{L}_{\mathsf{dd}} \end{bmatrix} \tag{7c}$$

L_{qq} and L_{dd} correspond to the inductance matrices in q- and d-axis respectively, whereas L_{qd} and L_{dq} represent the influence of d-axis currents on q-axis fluxes and vice versa.

A. Field oriented torque control (FOC)

Similar to a single rotor machine, the electromagnetic torque in the rotating parts is expressed as in **Eq.** (**8**). Since the magnitude of the electromagnetic torque not only depends on both the magnitude of the magnetic flux and the winding currents, but also on their relative angle, the torque can be controlled using field oriented control (FOC).

$$\begin{cases} \tau_2 = (I_{2q}\Psi_{2d} - I_{2d}\Psi_{2q}) \\ \tau_3 = (I_{3q}\Psi_{3d} - I_{3d}\Psi_{3q}) \end{cases} \tag{8}$$

with $\tau_2 = \frac{2}{3N_p} T_2$ and $\tau_3 = \frac{2}{3N_p} T_3$.

Fig. 4 denotes the direction of the flux and current phasors in both the inner rotor, the outer rotor and the stator. The

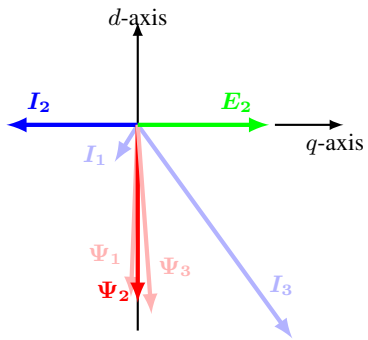

Figure 4: Field Oriented torque Control

relative phase of the qd-reference frame for FOC can be chosen freely. The authors of [20] choose the outer rotor flux Ψ_2 along the negative d-axis, which is also a typical convention in FOC for asynchronous machines.

$$\Psi_{2q} \equiv 0 \tag{9}$$

From **Eq.** (**8**), the torque on the outer rotor simplified as:

$$\tau_2 = \Psi_{2d} I_{2q} \tag{10}$$

Since this article performs a quasi-static analysis of the EVT, the outer rotor current is directed along the q-axis [20]:

$$I_{2d} \equiv 0 \tag{11}$$

A coupled-circuit FE model requires current input for each winding [21, 22]. Accordingly, there are 6 independent variables:

$$I_{1q},\ I_{1d},\ I_{2q},\ I_{2d},\ I_{3q},\ I_{3d} \tag{12}$$

Eqs. (**8**), (**9**) and (**11**) provide already four constraints. Two degrees of freedom remain available. A fifth constraint is generated if the magnitude of the outer rotor flux is controlled.

$$\Psi_{2d} = \Psi_{2d,set} \tag{13}$$

The main reason to control the flux magnitude is that it determines the saturation state of the machine and therefore both copper and iron losses [20]. From **Eq.** (**10**) and **Eq.** (**13**) the outer rotor current (I_{2q}) is directly calculated.

The last constraint can be fixed if the solution with minimal losses is selected. The FOC model is converted to a multi-constraint Lagrange problem with four variables. The corresponding cost function includes the joule losses in the stator and the inner rotor:

$$\text{minimize}\ \ R_1\left(I_{1q}^2 + I_{1d}^2\right) + R_3\left(I_{3q}^2 + I_{3d}^2\right) \tag{14a}$$

subjected to the following constraints:

$$\begin{cases} \Psi_{2q} & = 0 \\ \Psi_{2d} & = \Psi_{2d,set} \\ I_{3q}\Psi_{3d} - I_{3d}\Psi_{3q} & = \tau_3 \end{cases} \tag{14b}$$

The resulting Lagrangian function yields:

$$\begin{aligned} L = & R_1\left(I_{1q}^2 + I_{1d}^2\right) + R_3\left(I_{3q}^2 + I_{3d}^2\right) + \lambda\left(\Psi_{2q}\right) + \\ & \mu\left(\Psi_{2d} - \Psi_{2d,set}\right) + \nu\left(I_{3q}\Psi_{3d} - I_{3d}\Psi_{3q} - \tau_3\right) \end{aligned} \tag{15}$$

with variables $I_{1q}, I_{1d}, I_{3q}, I_{3d}$ and Lagrange multipliers λ, μ, ν. According to the theorem of Lagrange, the derivatives with respect to each variable and the Lagrange multipliers of **Eq.** (**15**) result in a system of 7 equations with 7 variables. Since the relation between currents and fluxes is expressed with the complete inductance matrix (**Eq.** (**7**a)), the system of equations is highly nonlinear and cannot be solved analytically. Instead, the Lagrange problem is solved numerically using MATLAB.

B. Iterative FOC using a non-linear EVT model

The FOC procedure presented in the previous section requires all machine parameters. Because the geometry is optimized, and thus variable, and core saturation is taken into account, the inductance matrix depends on both the geometry and the operating point (N_{out},T_{out}). This section proposes an iterative FOC method based on FE solutions shown in **Fig. 5**. Firstly, the geometric model is built and meshed using a commercial FE software program. In parallel, machine currents are evaluated performing the non-linear torque control method of the previous section based on an estimated inductance matrix. Secondly, the FE model is solved. Using the obtained field solution, the flux and the torque are calculated respectively. Subsequently, the inductance matrix is evaluated based on a linearised saturation characteristic. The spatial distribution of the relative permeability is saved. Then a perturbation current is applied in each winding separately to determine the (tangential) inductance. If the torque error is less than 2 % of its set-point, the procedure is ended. If not, the model is updated using the new inductance matrix and another iteration is executed.

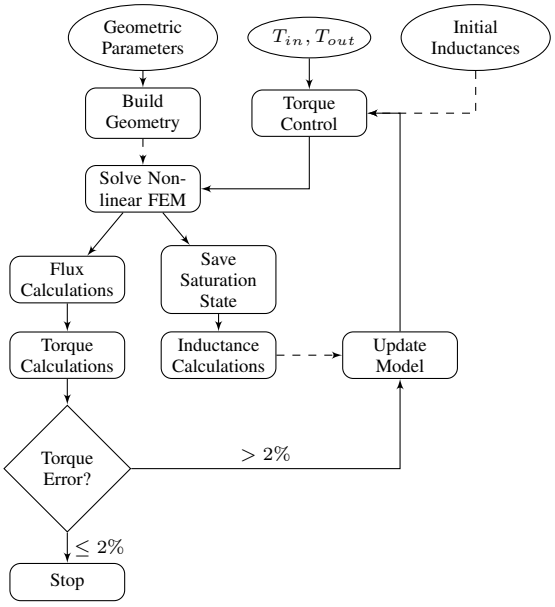

Figure 5: Flowchart of the iterative field oriented torque control algorithm.

IV. Optimization of the Outer Rotor Geometry

The algorithm presented in **Fig. 5** is used to optimize the design of the outer rotor. Only the influence of the inner and outer radius of the outer rotor is investigated. The number and the shape of the slots are not included in the optimization. Some parameters of the corresponding machine are listed in **Table I**. The stator and inner rotor are basically scale models of a real induction machine. The outer rotor is consists of a squirrel cage winding with 40 slots. The air gap widths (g_{12} and g_{23}) are fixed at $0.5\,\mathrm{mm}$. The axial length of the machine yields $300\,\mathrm{mm}$ The yoke hight in the stator and the inner rotor is respectively 50 and $60\,\mathrm{mm}$. The hight of the iron bridges in the outer rotor is restricted to $1\,\mathrm{mm}$ in order to limit flux leakage.

	Stator	Interrotor	Rotor
number of pole pairs p	2	-	2
number of slots N_i	48	40	36
number of windings w_i	144	cage	144
outer radius R_i [mm]	240	R_2	$r_2 - g_{23}$
inner radius r_i [mm]	$R_2 + g_{12}$	r_2	20
yoke high yh_i	50	1	60
tooth thickness Tw_i [mm]	10	$\frac{N_1}{N_2} Tw_1$	$\frac{N_1}{N_3} Tw_1$

Table I: EVT geometric parameters

The simulations are evaluated for a fixed engine speed ($N_{in} = 1\,\mathrm{pu}$) and gearbox working point (N_{out}, T_{out}). The input torque results from a power balance:

$$P_{out} = T_{out} * \Omega_{out} \tag{16a}$$

$$P_{in} = P_{out} + P_{cu} + P_{fe} \tag{16b}$$

$$T_{in} = \frac{P_{in}}{\Omega_{in}} \tag{16c}$$

with P_{cu} and P_{fe} respectively the total copper and iron losses in the EVT. The copper losses are calculated in agreement with [23], whereas the iron losses are evaluated using a method presented in [24]. Since a 2D static FE model is used, end-region effects, eddy currents and skin effects are neglected. An example field solution based on a FE simulation is shown in **Fig. 6a**. **Fig. 6b** shows a close up of the magnetic flux density in the inner air gap. $\Psi_{2d,set}$ is selected such that the flux density in the teeth reaches $1.6\,\mathrm{T}$. Additionally, the figure shows that the outer rotor bridges strongly saturate, which limits flux leakage in the outer rotor cage.

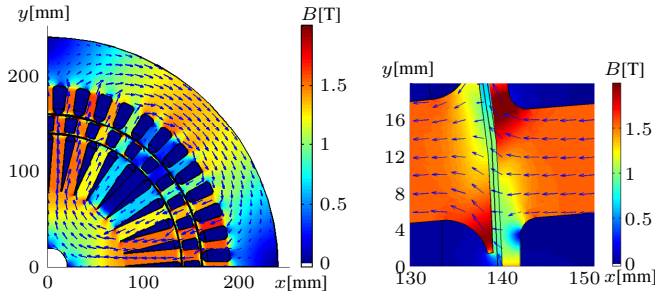

(a) **(b)** Close up

Figure 6: Magnetic field density in the EVT.

Fig. 7 presents the results of a geometrical optimization for two different output speeds, but equal output power. On the x- and y-axis the variation of the inner (r_2) and outer (R_2) radius of the outer rotor is represented. For both cases, the maximum electromagnetic efficiency is around $95\,\%$. In practice, the efficiency is lowered due to eddy currents and skin effects, and mechanical and ventilation losses. A comparison between **Figs. 7a** and **7b** shows that the optimal geometry is strongly dependent on the operating point. **Fig. 7a** presents the result of an overdrive operating point when the speed of the output shaft (outer rotor) exceeds the speed of the input shaft (inner rotor) whereas **Fig. 7b** considers direct-drive mode. The optimal outer rotor radii of the direct-drive simulation are pushed towards higher r_2 and R_2, since the stator torque (and thus current) is very small.

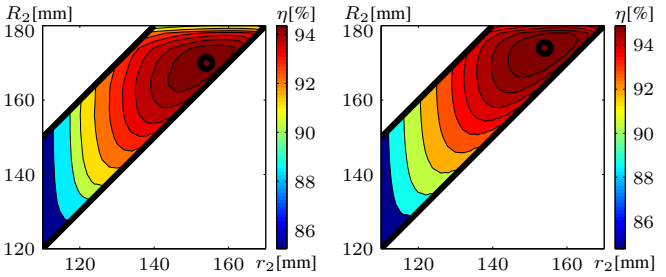

(a) $N_{out} = 1.3\,\mathrm{pu}$ **(b)** $N_{out} = 1\,\mathrm{pu}$

Figure 7: Geometrical Optimization for an overdrive and direct-drive working point.

In conclusion, the design of the EVT is strongly dependent on the application. The design based on the overdrive mode yields less losses in the regenerative mode, but increases losses when the slip between input and output shaft is low. The design based on the direct-drive mode certainly increases the losses in under- and overdrive mode since the stator copper section is very limited in this case.

V. Operational analysis: Stand-alone

In this section, the operational efficiency is analysed based on the optimal geometry of **Fig. 7a**. The output speed and torque are varied between 0.1 and $2.5\,\mathrm{pu}$, and 0.1 and $3.5\,\mathrm{pu}$ respectively. The corresponding efficiency map is presented in **Fig. 8**. The efficiency is very high in a large operating

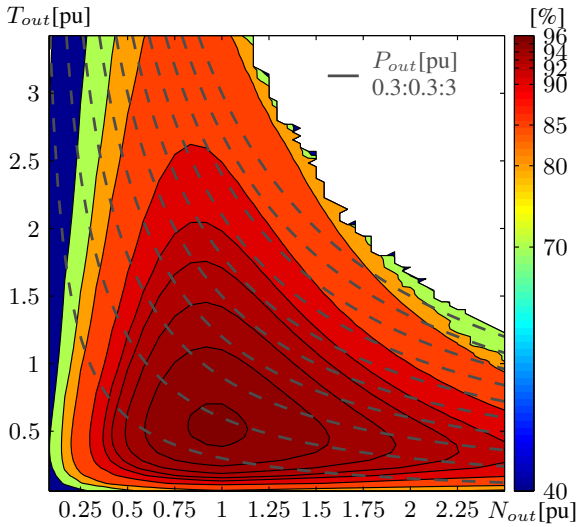

Figure 8: Efficiency map of stand-alone EVT.

region. The maximum efficiency is reached at $N_{out} = 1\,\mathrm{pu}$ when the input speed equals the output speed, since the stator torque and currents in direct-drive mode are very small. The interface between the coloured and white region represents an electromagnetic power limit. **Fig. 9** presents the power balance algorithm of **Eq.** (**16**) more in detail. The figure displays the power flow in function of the input torque for a constant output speed ($1.67\,\mathrm{pu}$). Because the input speed is fixed as well ($1\,\mathrm{pu}$), the input power varies linearly with the input torque. As the figure considers constant output torque values, the presumed output power is constant too and is represented by horizontal lines. The total machine loss is represented by the dashed lines and has a quadratic behaviour. The losses are only a little dependent on the output torque, since the variation of the input torque is much larger. The dash-dotted lines depict the effective output power, i.e. the input power minus the machine losses. The effective output power reaches its maximum when the slope of the machine loss equals the slope of the input power. Consequently, the effective output power decreases for very high input torque values. The working point yields from the intersection of the presumed and effective output power depicted by the circle on **Fig. 9**. When the presumed output power exceeds the maximum effective output power, there is no intersection point any more. The presumed output power can thus not be delivered at the considered input and output speed.

A. Electrical power through the PECs

Figs. 10a and **10b** represent the electrical power and electrical power fraction through the converters respectively. The figure denotes that the electrical power fraction is linearly

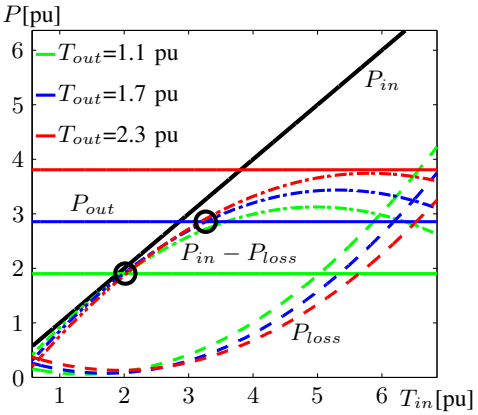

Figure 9: Power limit at fixed input speed.

decreasing with the output speed in agreement with **Eq.** (**3**). The power fraction is also little dependent on the output torque since the outer rotor slip increases with the output torque. Moreover, the electrical power fraction turns negative when the speed of the output shaft exceeds the speed of the input shaft ($1\,\mathrm{pu}$). Because the inner rotor slip is positive in this operation region, the rotor functions as an induction motor and adds the electrical power from the PECs to the input power, which is then electromagnetically transferred through the inner air gap. Consequently, both $P_{el,out}$, $P_{el,in}$ and $P_{f,out}$, have negative values. Since the recirculating power is increasing very fast in overdrive mode, the maximum output speed needs to be limited. **Fig. 10** denotes that if the operational speed

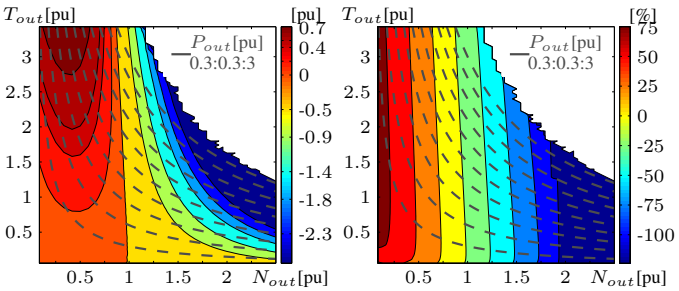

(a) $P_{el,in}$ **(b)** $x_{el} = P_{el,in}/P_{in}$

Figure 10: Electrical power through the converters.

is restricted between $0.5\,\mathrm{pu}$ and $1.5\,\mathrm{pu}$, the power fraction through the converters is included between $50\,\%$ and $-50\,\%$. In conclusion, the rated power through the converter is halved compared to a serial connection of two electrical machines.

VI. Operational analysis: ICE - EVT configuration

In the previous section, the EVT is analysed in standalone mode, i.c. the input speed is assumed constant. This section studies the EVT when the device is connected to an ICE. Instead of a constant input speed, the speed of the input shaft is selected so that the ICE operates at least specific fuel consumption (sfc). This section also compares the performance of the EVT functioning as a torque converter to that of a HTC.

Fig. 11 presents a normalized fuel map of a commercial off-highway engine. The optimal engine line, i.c. line of minimum

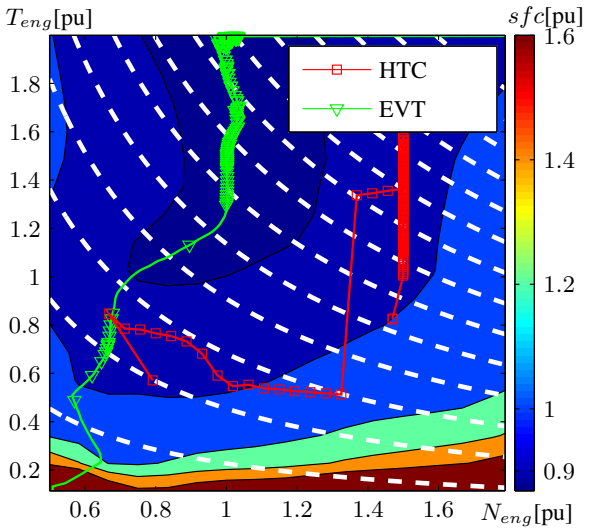

Figure 11: Fuel map of ICE including EVT and HTC operation points.

specific fuel consumption, is denoted in green. The considered engine has two specific speeds: $0.7\,\mathrm{pu}$ for low power demand, and $1\,\mathrm{pu}$ for high power demand. Furthermore, the engine torque is limited to $2\,\mathrm{pu}$ in the simulations. The connection of the ICE to the EVT, changes the power balance equations (**Eq.** (**16**c)) to:

$$T_{in} = F_{sfc}\left(P_{in}\right) \tag{17a}$$

$$\omega_{in} = \frac{P_{in}}{T_{in}} \tag{17b}$$

with F_{sfc} a function that represents the torque at the optimal engine line in function of the engine power. Similar to **Section V**, an efficiency map in function of the output operating point is built. The efficiency map of ICE-EVT configuration

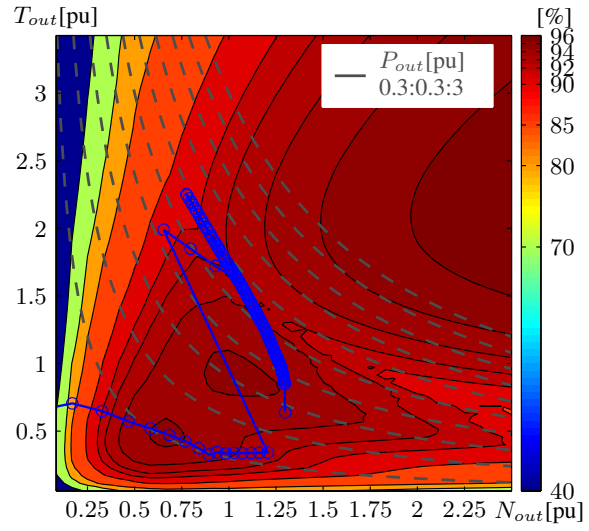

Figure 12: Efficiency map of ICE-EVT configuration including representative driving cycle

has two local maxima, corresponding to the characteristic speeds of the engine. Unlike **Fig. 8**, **Fig. 12** does not include a power limit, since the engine is torque limited. Instead, the efficiency is increasing for a very high power demand as the machine losses are strongly correlated to the engine torque.

A. Driving cycle analysis

This section compares the performance of the EVT to that of a HTC using a representative driving cycle (i.c. an acceleration from standstill) of an off-highway vehicle including a five shift gearbox. The comparison is based on a backward analysis of the drivetrain, i.c. the speed and torque at the output of the converter are equal for both configurations. The driving cycle is added to **Fig. 12**. The distance between the markers represents $0.1\,\mathrm{s}$. The figure shows that the complete driving cycle is located in a very high efficiency region. The efficiency drops below $70\,\%$ only for a very short time during start-up.

Fig. 13 displays the engine speed and torque of the considered duty cycle for both the HTC and the EVT configuration. Because the EVT is able to operate in overdrive mode, the speed of the engine is significantly decreased compared to the HTC configuration. Moreover, thanks to the increased efficiency of the EVT, especially during the shifts, the torque ripple in the engine is reduced as well. The engine operating points for both configurations are added to **Fig. 11** which yield the same results.

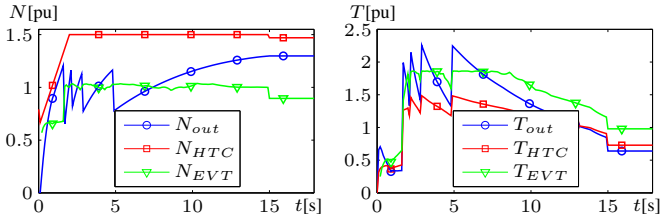

(a) Speed **(b)** Torque

Figure 13: Comparison of engine speed and torque between EVT and HTC.

Since the EVT has a very high efficiency in all operation points (around $95\,\%$), **Fig. 14a** only displays the efficiency gain between the EVT and HTC configurations. The spikes correspond to the shifts of the gearbox. The efficiency of the EVT exceeds the efficiency of the HTC by $10\,\%$ in all operating points. Moreover, at full speed, the efficiency is even $17\,\%$ higher, due to the relatively bad efficiency of a partial loaded HTC. Therefore, a lock-up clutch in the EVT configuration may not be necessary any more.

Fig. 14b displays the electrical power through the converters in relation to the input power. The figure denotes that the electrical power fraction is high during start up. Nevertheless, since the starting power is relatively low, the electrical power through the PECs is limited to $0.4\,\mathrm{pu}$ during the complete driving cycle. Consequently, the use of a five shift gearbox in combination of an EVT limits the power through the PECs to one fifth of the driving power and thus much smaller PECs can be chosen.

The fuel consumption of both configurations is compared in **Fig. 15**. Since the EVT allows the engine to operate at

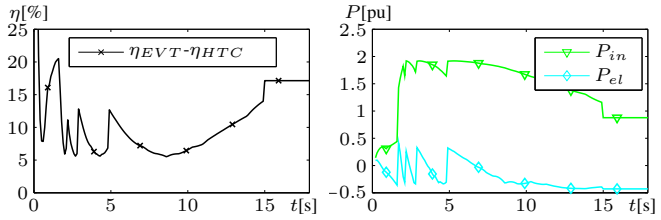

(a) Efficiency increase **(b)** Power through the converters

Figure 14: Efficiency increase and electrical power of the EVT configuration.

the optimal power line, the fuel consumption is significantly reduced. The sfc is decreased by almost 15 %. Moreover, the total fuel consumption is decreased even more thanks to the very high efficiency of the EVT in all operating points. The simulations reveal that the fuel savings for the considered driving cycle are upto 20 %. It can thus be concluded that the EVT functioning as a torque converter is a very promising solution for off-highway transmission systems.

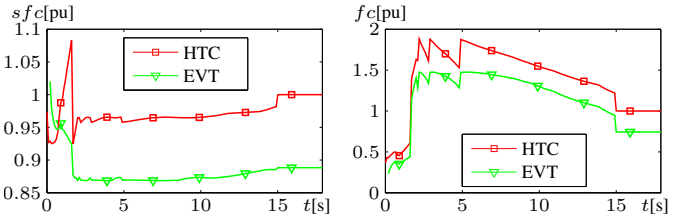

(a) Specific fuel consumption **(b)** Fuel consumption

Figure 15: Comparison of specific fuel consumption and fuel consumption between EVT and HTC.

VII. Conclusion

In this paper, a parametrized 2D quasi-static coupled-circuit finite element model of the EVT is built, including an iterative field oriented control algorithm. The model is used to evaluate the performance of an EVT both in standalone mode and connected to an ICE. It is concluded that the use of EVT as a torque converter is a very promising solution for off-highway transmission systems. In combination with a five shift gearbox, the size of the electrical converters of the EVT is reduced by 80 %, compared to a serial electrical machine connection. Furthermore, it is shown that the replacement of a HTC by an EVT system in an off-highway vehicle increases the torque converter efficiency by 10 %. Additionally, the EVT configuration significantly decreases engine torque ripple and leads to 20 % fuel savings thanks to a more optimal engine use.

References

[1] Bosch Rexroth, *Energy System Design for Optimized Power Management*. Bosch Rexroth, 2012, pp. 76 – 83. [Online]. Available: http://apps.boschrexroth.com/microsites/mobile2012/downloads/cornolti_art.pdf

[2] K. van Berkel, T. Hofman, B. Vroemen, and M. Steinbuch, "Optimal control of a mechanical hybrid powertrain," *Vehicular Technology, IEEE Transactions on*, vol. 61, no. 2, pp. 485–497, Feb 2012.

[3] M. Comellas, J. Pijuan, X. Potau, M. NoguÃ©s, and J. Roca, "Analysis of a hydrostatic transmission driveline for its use in off-road multiple axle vehicles," *Journal of Terramechanics*, vol. 49, no. 5, pp. 245 – 254, 2012. [Online]. Available: http://www.sciencedirect.com/science/article/pii/S002248981200047X

[4] N. Beachley and A. Frank, *Continuously variable transmissions: theory and practice*. California Univ., Livermore (USA), Aug 1979. [Online]. Available: http://www.osti.gov/scitech/servlets/purl/5529813

[5] B. Bonsen, T. Klaassen, K. Van de Meerakker, M. Steinbuch, and P. Veenhuizen, "Analysis of slip in a continuously variable transmission," in *ASME 2003 International Mechanical Engineering Congress and Exposition*. American Society of Mechanical Engineers, 2003, pp. 995–1000.

[6] K. T. Renius and R. Resch, *Continuously variable tractor transmissions*. American Society of Agricultrual Engineers, 2005.

[7] A. Macor and A. Rossetti, "Optimization of hydro-mechanical power split transmissions," *Mechanism and Machine Theory*, vol. 46, no. 12, pp. 1901 – 1919, 2011. [Online]. Available: http://www.sciencedirect.com/science/article/pii/S0094114X11001418

[8] M. J. Hoeijmakers and J. A. Ferreira, "The electric variable transmission," *Industry Applications, IEEE Transactions on*, vol. 42, pp. 1092–1100, 2006.

[9] J. Druant, P. Sergeant, F. De Belie, and J. Melkebeek, "Modeling and control of an induction machine based electric variable transmission," in *Young Researchers Symposium, Proceedings*, 2014, p. 5.

[10] K. Chau and C. Chan, "Emerging energy-efficient technologies for hybrid electric vehicles," *Proceedings of the IEEE*, vol. 95, no. 4, pp. 821–835, April 2007.

[11] L. Chen, F. Zhu, M. Zhang, Y. Huo, C. Yin, and H. Peng, "Design and analysis of an electrical variable transmission for a series/parallel hybrid electric vehicle," *Vehicular Technology, IEEE Transactions on*, vol. 60, no. 5, pp. 2354–2363, Jun 2011.

[12] X. Sun, M. Cheng, W. Hua, and L. Xu, "Optimal design of double-layer permanent magnet dual mechanical port machine for wind power application," *Magnetics, IEEE Transactions on*, vol. 45, no. 10, pp. 4613–4616, 2009.

[13] X. Sun, M. Cheng, Y. Zhu, and L. Xu, "Application of electrical variable transmission in wind power generation system," *Industry Applications, IEEE Transactions on*, vol. 49, pp. 1299–1307, 2013.

[14] S. Eriksson and C. Sadarangani, "A four-quadrant hev drive system," in *Vehicular Technology Conference, 2002. Proceedings. VTC 2002-Fall. 2002 IEEE 56th*, vol. 3. IEEE, 2002, pp. 1510–1514.

[15] Y. Liu, S. Ho, and W. Fu, "Novel electrical continuously variable transmission system and its numerical model," *Magnetics, IEEE Transactions on*, vol. 50, pp. 757–760, 2014.

[16] S. Niu, S. Ho, and W. Fu, "Design of a novel electrical continuously variable transmission system based on harmonic spectra analysis of magnetic field," *Magnetics, IEEE Transactions on*, vol. 49, pp. 2161–2164, 2013.

[17] K. Atallah, J. Wang, S. Calverley, and S. Duggan, "Design and operation of a magnetic continuously variable transmission," *Industry Applications, IEEE Transactions on*, vol. 48, no. 4, pp. 1288–1295, July 2012.

[18] M. J. Hoeijmakers and M. Rondel, "The electrical variable transmission in a city bus," in *Power Electronics Specialists Conference, 2004. PESC 04. 2004 IEEE 35th Annual*, vol. 4. IEEE, 2004, pp. 2773–2778.

[19] P. Linares, V. Méndez, and H. Catalán, "Design parameters for continuously variable power-split transmissions using planetaries with 3 active shafts," *Journal of Terramechanics*, vol. 47, no. 5, pp. 323–335, 2010.

[20] J. Druant, P. Sergeant, F. De Belie, and J. Melkebeek, "Field oriented control for an induction machine based electrical variable transmission," in *IEEE Transactions on Vehicular Technology [submitted]*, 2015.

[21] S. Williamson, L. Lim, and A. Smith, "Transient analysis of cage-induction motors using finite-elements," *Magnetics, IEEE Transactions on*, vol. 26, no. 2, pp. 941–944, 1990.

[22] P. Zhou, J. Gilmore, Z. Badics, and Z. J. Cendes, "Finite element analysis of induction motors based on computing detailed equivalent circuit parameters," *Magnetics, IEEE Transactions on*, vol. 34, no. 5, pp. 3499–3502, 1998.

[23] P. Trickey, "Induction motor resistance ring width," *Electrical Engineering*, vol. 55, no. 2, pp. 144–150, Feb 1936.

[24] D. Kowal, L. Dupre, P. Sergeant, L. Vandenbossche, and M. De Wulf, "Influence of the electrical steel grade on the performance of the direct-drive and single stage gearbox permanent-magnet machine for wind energy generation, based on an analytical model," *Magnetics, IEEE Transactions on*, vol. 47, no. 12, pp. 4781–4790, Dec 2011.

Contents

List of Figures

List of Tables

Nomenclature

Acronyms

AC	Alternating Current
CVT	Continuously Variable Transmission
DC	Direct Current
EMCA	Equivalent Magnetic Circuit Analysis
EMF	Electromagnetic Force
EVT	Electrical Variable Transmission
FC	Fuel Consumption
FEA	Finite Element Analysis
FEM	Finite Element Model
FMP	Ferromagnetic Polepieces
FOC	Field Oriented torque Control
GHG	Greenhouse Gasses
HFT	Maxwell stress Harmonic Filter Torque
HTC	Hydraulic Torque Converter
HVT	Hydraulic Variable Transmission
ICE	Internal Combustion Engine
MMF	Magnetomotive Force
PGT	Planetary Gear Train
PM	Permanent Magnet
PS-CVT	Power-Split Continuously Variable Transmission
SFC	Specific Fuel Consumption
THS	Toyota Hybrid System

Electrical Parameters

α_i	electrical displacement between successive slots
A_z	magnetic vector potential
B_x,B_y	magnetic vector potential
η	efficiency
f	stator supply frequency
I	current
J_z	current density
K_{ring}	Trickey end-ring correction factor
λ, μ, ν	Lagrange multipliers
$\mathsf{L_{dd}}$	d-axis inductance matrix
$\mathsf{L_{ind}}$	complete inductance matrix
$\mathsf{L_{qq}}$	q-axis inductance matrix
m_i	number of phases
N_i	mechanical speed

N_{eng}	engine speed
N_p	number of pole pairs
ω	stator supply pulsation
Ω_i	mechanical speed
P_{cu}	copper loss
P_d	direct power through the EVT
P_e	electrical power through the EVT
P_{eng}	engine power
P_{fe}	iron loss
$P_{f,in}$	input airgap power
$P_{f,out}$	output airgap power
ϕ_i	physical flux
P_{in}	input power
P_m	power through mechanical path in PS transmissions
P_{out}	output power
P_{rated}	rated power
Ψ_i	coupled flux
P_{tot}	total loss
P_v	power through variable path in PS transmissions
q_i	number of slots per pole pair per phase
Res_{bar}	interrotor bar resistance
Res_i,R_i	winding resistance
ρ_{al}	aluminium specific resistance
ρ_{cu}	copper specific resistance
s_i	slip
$\boldsymbol{\sigma}$	Maxwell stress tensor
T_e	electromechanical torque in an airgap
T_{eng}	engine torque
T_i	torque
T_{in}	input torque
T_{out}	output torque
V_i	terminal voltage
w_i	number of turns
x_i	winding distribution factors

Geometrical Parameters

$A_{wire,i}$	cross section of a wire
D_i	end-ring internal diameter
D_r	rotor bar pitch circle diameter
F_r	slot fillrate
g_{12}	outer airgap width
g_{23}	inner airgap width
L_{ax}	axial machine length
$l_{wire,i}$	total wire length of phase wire
N_i	number of slots
R_i	outer radius
r_i	inner radius

R_{gi}	inner airgap boundary radius for Maxwell HFT
R_{go}	outer airgap boundary radius for Maxwell HFT
R_i	inner airgap radius
R_o	outer airgap radius
R_t	transmission ratio
Rt_i	tooth base radius
R_{tm}	mechanical transmission ratio
S_{ag}	cross sectional airgap area
sc_D	radial scaling factor
sc_L	axial scaling factor
sc_Ψ	flux scaling factor
Scu_i	slot surface area
t	thickness of the end-rings
τ_i	pole pitch of a winding
To_i	tooth opening width
Tw_i	tooth width

Electromagnetic Parameters

$\boldsymbol{B}$	magnetic flux density
$\boldsymbol{B}_r$	remanent magnetic flux density
$\boldsymbol{D}$	electric flux density
Δ	Laplace operator
∇	del operator
$\boldsymbol{D}_r$	remanent electrical displacement
$\boldsymbol{E}$	electric field intensity
ϵ_0	permittivity of vacuum
ϵ_r	relative permittivity
$\boldsymbol{H}$	magnetic field intensity
$\boldsymbol{J}$	current density
μ_0	permeability of vacuum
μ_r	relative permeability
ρ	electric charge density
t	time

Subscripts

1	stator
2	interrotor
3	rotor
in	input
out	output

Chapter 1

Introduction

1.1 Motivation

In order to reduce the impact of climate change and global warming, the European Union has set itself ambitious targets. These targets are listed in 'the 2020 climate and energy package'[1] of the European Union and include:

- A 20 % reduction in EU greenhouse gas (GHG) emissions from 1990 levels;
- Raising the share of EU energy consumption produced from renewable resources to 20 %;
- A 20 % improvement in the EU's energy efficiency.

The transport sector is responsible for about a quarter of the EU greenhouse gas emissions, making it the second biggest greenhouse gas emitting sector after energy production. The EU has policies in place to reduce emissions from a range of modes of transport, such as directives on emission regulation.

The first directive (directive 2000/25/EC) for off-highway vehicles has already been presented in the beginning of the 21^{st} century. This directive deals with the requirements concerning emissions by agricultural and forestry tractors. Since then, the European Union increased pressure to reduce emissions in off-highway vehicles. In order to limit global warming by 2 °C, GHG emissions need to be reduced 60 % by 2050 compared to the 1990's levels[2]. To meet these challenging targets, radical changes are required in the transportation sector.

Although a lot of research is being performed in order to reduce fuel consumption and thus pollution, a good alternative for the petrol fuelled vehicle is not yet immediately available. The massive production of electrical cars is obstructed by the unsatisfactory performance of battery technologies and the high cost of fuel cells. Moreover, present-day batteries are not yet capable to deliver high power and are thus not yet suited for heavy-duty applications. As a first step, hybrid vehicles have been considered as the best intermediate choice on the way to a clean and energy efficient future.

[1] http://ec.europa.eu/clima/policies/package/index_en.htm
[2] http://ec.europa.eu/clima/policies/roadmap/perspective/index_en.htm

This master thesis is done in corporation with Dana-Spicer, one of the world's biggest producers of transmissions systems. Dana is an US-based company with a corporate R&D-center in Bruges. As all other actors in the transportation industry, they are continuously looking for innovative technology to increase revenue by boosting their system's efficiency and thus reducing CO_2-emissions. Dana Bruges mainly develops *powershift* transmissions in which the torque flow is not interrupted during the shifts. A conventional transmission for off-highway vehicles consists of a conventional gearbox driven by a hydraulic torque converter. The powershift is realized by the overlapped closing and releasing of wet plate clutches in the gearbox. Although these transmissions are frequently used in the off-highway market, they have some inherently disadvantages:

- Still a torque reduction during shifting;
- Non-optimal engine operating point due to fixed transmission ratios;
- Relatively low efficiency compared to electrical devices. The overall efficiency of a conventional transmission system lies around 85 %. However, depending on the operating point, this can be significantly lower, resulting in a global efficiency of about 80 %.

This relatively low overall efficiency is the main driver behind the research of alternative concepts. A promising concept from the literature is the Electrical Variable Transmission (EVT), an electromagnetic machine with two coupled rotors and two inverters (stator and one rotor) in back-to-back configuration. The principle allows to have both speed and torque variations with high efficiency. The main power path in such a device is magnetic, which has an inherently higher efficiency as its hydraulic equivalent. Furthermore, the EVT allows vehicle operation with an infinite number of transmission ratios and thus permits the Internal Combustion Engine (ICE) to work at a better operating point, resulting in a significantly reduced fuel consumption.

1.2 Objectives

The main goal of this research is a feasibility study the replacement of a hydraulic torque converter by an electrical variable transmission. In order to reach this goal the following objectives were set:

- In the first place, the research is limited to the electromagnetic design using a two dimensional finite element analysis. Three dimensional effects and thermal, mechanical and manufacturing issues are only mentioned briefly. Moreover, only static magnetic fields are studied. Consequently, conclusions reported in this paper counts only for static and quasi-static machine operation.
- Secondly, the finite element model is parametrized, enabling to study the influence of different geometrical parameters on the system's efficiency.

- At last, procedures are developed in order to study the system's efficiency at a broad range of operating points. The procedures include torque control and parameter estimation for different operating points. The obtained parameters can be used in other models to study both transients and faulty analyses. Furthermore, the efficiency map is also used in a real-life simulation of the integration of an electrical torque converter in an off-highway transmission system.

1.3 Outline

The structure of this thesis comprises three major parts: the study of present-day transmission systems, the study and set-up of the finite element model, and the geometrical and operational analyses for different EVT sizes.

As the main goal of this master thesis is a feasibility study of the replacement of a hydraulic torque converter by an EVT, a brief study of the hydraulic torque converter can not be skipped. Because the use of the EVT is not limited to a torque converter only, Chapter 2 also includes a broad range of clutch and transmission systems. It introduces topologies and working principles of different continuously variable transmissions with the focus on power split transmissions. Chapter 3 deals with electrical continuously variable transmissions (EVTs). In literature, several EVT topologies are presented and some of them are already prototyped. The chapter introduces the proposed EVT design for compact implementation, based on the work of Druant et al. (2014) and Hoeijmakers et al. (2006), which is studied in this paper.

The second major part comprises a finite element (FE) model of the EVT and is discussed in Chapters 4 and 5. Chapter 4 describes the basic equations of FE analysis and several reference papers. The subsequent chapter deals with the finite element model of compact design EVT introduced in Chapter 3. Both geometric and electric parameters are described here. Furthermore, the chapter presents and compares different methods for torque calculation and develops a field oriented torque control on the double rotor induction machine.

The last part is dedicated to simulation results. In Chapter 6, a geometrical optimization of the EVT is performed. The EVT dimensions are based on a 9 kW induction motor which is also described in Druant et al. (2015). Closely related to the geometrical optimization, an operational analysis is performed in Chapter 7. An efficiency map in function of the output speed and torque is presented in this stage. In the last chapter of this thesis, the process of optimization and operation analysis is repeated for a real implementation. Based on the dimensions of a 250 kW torque converter of Dana-Spicer, a larger EVT is studied. The corresponding geometry is optimized including ICE characteristic. Furthermore, the chapter includes an operational analysis which takes into account the optimal performance of the ICE. The presented method allows to compare the overall fuel consumption of a vehicle including a classical hydraulic torque converter and a vehicle including the EVT.

Chapter 2

Clutch and Transmission and systems

Since the EVT is supposed to replace the clutch and/or transmission system in off-highway machinery, this chapter describes the different systems. Clutch and transmissions systems exist in many different kinds and sizes.

In the first section, three different clutch systems are described: from a simple friction clutch, over a hydraulic torque converter, to the more advanced VariGlide from DANA. In the subsequent sections, transmission systems are discussed. Transmission systems used in vehicles can be grouped into two main types: step and stepless ratio transmissions. The traditional multi-ratio transmissions, standard and automatic, are used in combination with a clutch system or a hydraulic torque converter respectively. Stepless transmissions, also known as continuous variable transmissions (CVT), are less familiar to most readers and do not always need a clutch system any more. The EVT is a prospective device to be applied as a continuous variable transmission system. Therefore only the CVT systems are described in the transmission section.

2.1 Clutch systems

2.1.1 Friction clutch

Mounted between the internal combustion engine and the gearbox, the clutch is a very simple device to overcome small speed differences while shifting gears. A gradual coupling of these two axes is necessary to depart from a standstill, since the engine has a minimum speed and does not produce enough torque at lower speeds. A clutch is mostly used in passenger cars and light duty vehicles in which the transmission is not used extensively. The main advantage of the clutch system is its simple design. Basically, it consists of two circular plates pressed against each other as schematically shown in Fig. 2.1.

At no-load, the plates are separated with a small gap. The combustion engine and gearbox are disengaged. If a force is gradually applied to the plates (releasing the pedal), the plates touch each other and start to slip as there is a difference in speeds between the driving axes (ICE) and driven axes (wheels). If the force is increased, slip between the plates reduces and eventually the two axes are fully coupled. The speed of the driving and driven axes are now equal.

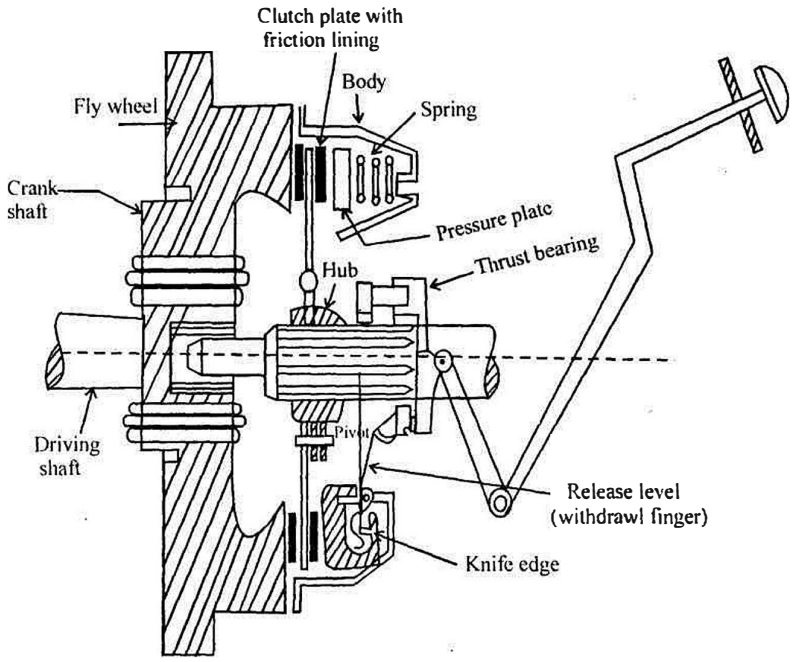

Source: http://www.ululu.in[1].

Figure 2.1: Single plate clutch system (schematic)

The main advantage of the clutch is its simple design. On the other hand, the main disadvantage is heat generation. While slipping, friction between the plates generates heat which limits the power transfer. Thus, with a clutch system, it is only possible to overcome little speed differences and the usage is limited in time. In order to overcome the heating problem, different modifications can be made. Firstly, if the plates are made bigger, the head dissipation takes place over a bigger surface and is thus less critical. Secondly, it is possible to use multiple friction surfaces in series. The heat dissipation is again distributed over a bigger surface. The advantage of the latter in comparison to the former is its compactness. Finally, it is also possible to use wet friction surfaces. In this case, the friction plates are cooled using oil. On the other hand, a larger friction surface is necessary, since the friction coefficients of the plates is much less.

A secondary disadvantage of a clutch system is its loss of torque during gear shifting. For heavy duty applications it is not possible to switch gears while the machine is working. At last, since the clutch system intents to make a mechanical coupling between the combustion engine and the wheel axes, vibrations are transferred in both ways, which are disagreeable for both the driver and the ICE. Torsional damper springs are added in the friction plates to limit the transfer of vibrations.

2.1.2 Hydraulic torque converter

Another kind of transmission system is a hydraulic torque converter as shown in Fig. 2.2. The torque converter is generally a type of fluid coupling that is used to transfer rotating power from the internal combustion engine to the wheels. This coupling system uses the pump-turbine working

principle in order to transfer power. The pump (impeller) is located at the driving axes, the turbine is connected to the gearbox and a stator is placed in between.

Oil is guided outwards in the pump by centrifugal forces. As the oil hits the turbine, the energy content of the oil decreases and the oil is returning to the center, whereas mechanical power is transferred to the turbine. When the oil is returning to the center, the direction of the flow is different from the flow direction in the impeller. The oil would hit the impeller blades which reduces the output torque. The stator redirects the oil-flow to reduce such impact losses in the returning flow. Consequently, the output couple is increased in the high slip region. When the slip decreases, the relative direction between the turbine output flow and pump input flow decreases. If the stator was fixed, the turbine output flow would impact the back of the stator blades which causes a couple reduction. In order to overcome this phenomenon, the stator is mounted on a freewheel. The stator-wheel will turn together with the turbine- and impeller-wheels.

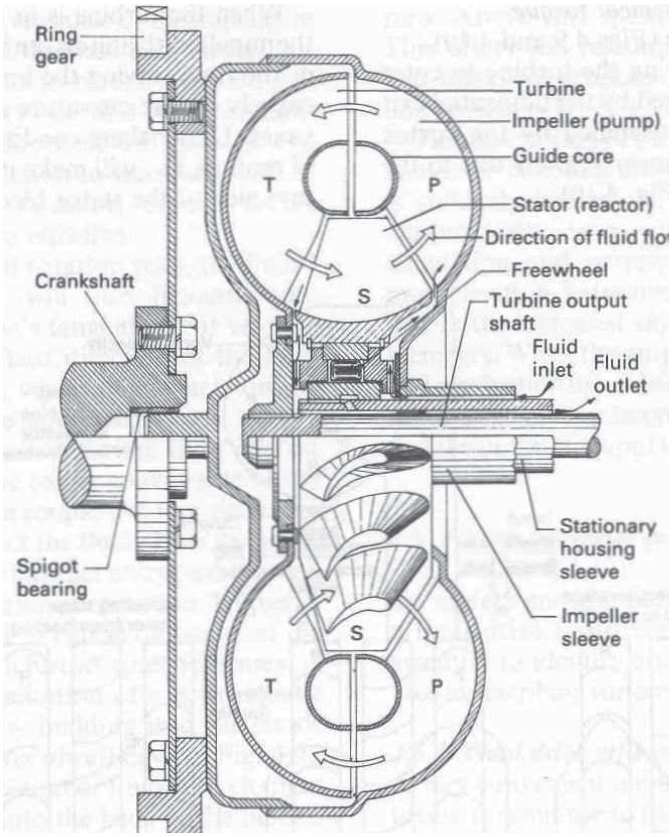

Source: Verhelst (2013, page 59).

Figure 2.2: Hydraulic torque converter

Basically, the torque converter has three stages of operation:

- Stall: the engine is providing power to the impeller but the turbine can not rotate. At stall, the torque converter can produce maximum torque multiplication if sufficient input power is applied.

- Acceleration: the vehicle is accelerating but there is still relatively large difference between the impeller and turbine speed. The torque multiplication is less than under stall conditions and depends on the actual speed difference and design factors.
- Coupling: the speed of the turbine is about 90% of the speed of the impeller. The torque converter does not multiply the torque any more and behaves like a simple fluid coupling. In most automotive application a lock-up clutch is applied. In this way, there are no slip losses in the device any more.

The torque multiplication ratio and efficiency of a typical torque converter is given in Fig. 2.3.

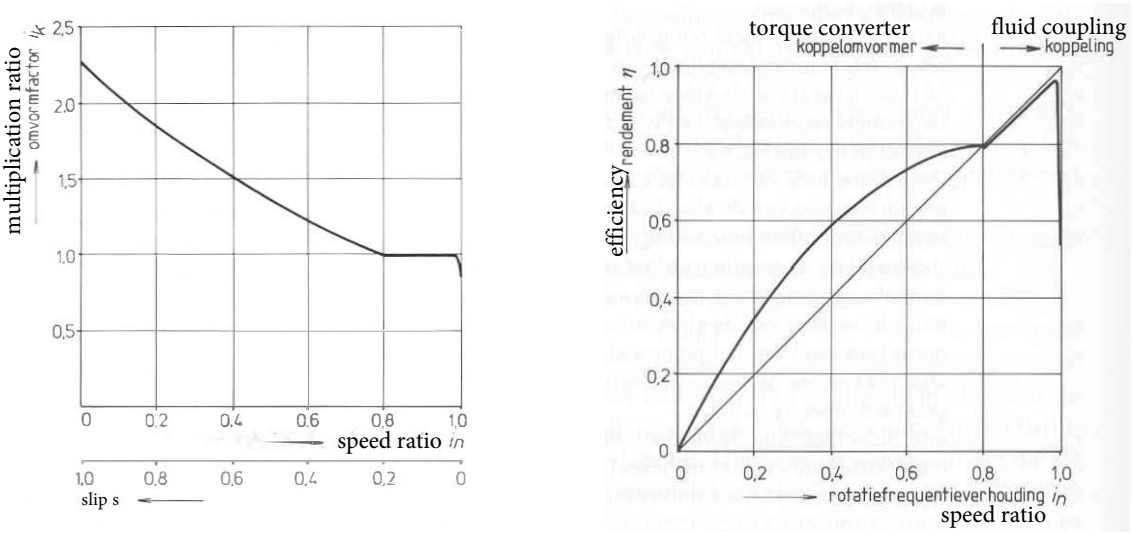

Source: Verhelst, 2013, page 61.

Figure 2.3: Torque converter multiplication ratio(a) and efficiency(b)

The hydraulic coupling between the shafts reduces the transfer of vibrations. On the other hand, its efficiency is quite low: zero efficiency at stall, increasing efficiency during acceleration and low efficiency in the coupling phase (around 80% is usual). The efficiency is related to the slip as can be seen in Fig. 2.3. During start-up, when slip is high, the power delivered by the ICE is much higher than the useful power to accelerate the vehicle. Moreover, a hydraulic torque converter requires a bit of slip to be able to transfer torque. Consequently, there is always a power loss while using it, unless a lock-up device is integrated in the transmission system.

The hydraulic torque converter is mostly used in automatic transmission systems, in contrast to the friction clutch, which is frequently used with manual gearboxes. Switching gears using an automatic transmission allows a smooth transmission from one gear to another. Unlike the clutch system there is no complete torque loss while switching gears. By use of electronic control, it is possible to engage partially two different gears. The torque to the wheels is not completely lost during switching, but there is still a torque loss which can cause driving problems.

2.1.3 VariGlide

Very recently Dana Corporation introduced a new device to overcome the speed difference between the engine and the wheels in off-highway machinery: the VariGlide[2]. The VariGlide is a new kind of transmission system that resembles both a planetary gear set and a special roller bearing. It can be seen as a continuous variable planetary gear set in which sun and ring gears are replaced with rings and in which the planets are balls; or it can be seen as a roller bearing in which the outer ring is split into two parts as shown in Fig. 2.4. The power enters the VariGlide through the red ring.

Source: `http://www.variglide.com/`.

Figure 2.4: Dana's VariGlide: continuously variable planetary technology

Similar to a planetary gear set, the power is transmitted to the planets (i.e. balls). The balls in the variator transmit the power to the other outer ring (blue). When the rotation axis of the balls is changed, as shown in Fig. 2.5, there is a speed difference between the outer rings. Both underdrive and overdrive transmission ratios can be reached using the device.

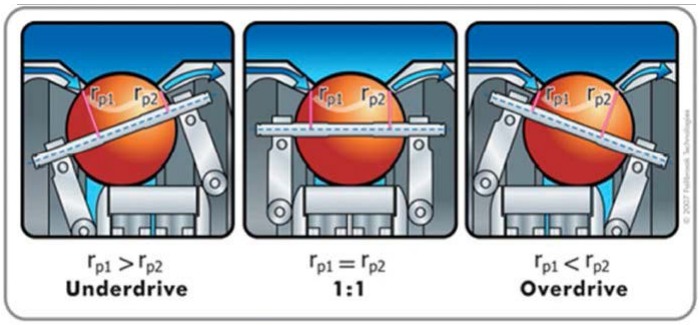

Source: `http://www.variglide.com/`.

Figure 2.5: Dana's VariGlide: working principle

[2] `http://www.variglide.com/`

The variator is mostly used in combination with a traditional gearbox. It allows a wider range of gear ratios such that the engine can be operated in a more efficient operating point. In this way, the VariGlide can be seen as the first step to a continuous variable transmission in high-duty machinery. According to Dana, the fuel savings using the VariGlide instead of an usual torque converter are up to 20 %. Moreover, it enhances the comfort of the driver. To avoid a metal-to-metal contact between the ball and the rings, the transmission is filled with a special traction fluid. Consequently, the power is transferred by shear forces in the liquid which limits the maximal torque that can be transmitted through the device.

2.2 Continuously Variable Transmission systems

In gearbox systems, the clutch or hydraulic torque converter is only used temporally while switching gears. This means that in regime the speed of the vehicle is related to the speed of the ICE by means of discrete transmission ratios. Consequently, for a given power consumption it is not always possible to operate the ICE in its most efficient working point. To overcome this issue, a whole different kind of transmission system is required, the continuously variable transmission (CVT). Its speed ratio may take any value between its operational limits, i.c. an infinite number of fixed speed ratios. A CVT system also implies that the speed ratio may be controlled independently of the output torque of the device. Consequently, the torque converter, which is able to cover an infinite number of transmission ratios, can not be classified as a CVT as the speed ratio is not controllable (Beachley et al., 1979).

Many CVT design principles have been proposed in literature from very easy concepts, like a belt driven CVT, to quite advanced topologies, like power-split CVT systems. In the next sections the most popular CVT configurations are described. Their operating principles are explained and the main (dis)advantages are reported.

2.2.1 Belt driven CVT

A CVT can operate at a wider range of transmission ratios, so that the engine can be operated more efficiently than with a stepped transmission (Bonsen et al., 2003). Moreover, the CVT does not interrupt the torque while shifting. The most simple design of a CVT is a belt driven device. The transmission consists of two pulleys of which the sides are movable (variators) by means of a mechanic device or a hydraulic control cylinder. A V-belt is clamped in between the disks. The torque is transferred between the pulleys by friction. The layout of the CVT and the V-belt are shown in Fig. 2.6. A sufficiently high clamping force is necessary to prevent slip in the variators. According to Bonsen et al. (2003) higher clamping force levels cause more losses in the CVT since more power is consumed by the hydraulic clamping pomp, by micro-slip between the pulleys and the belt, and by the deformation of the belt and the pulleys. If the clamping force is too low, the transmission is not able to transfer the required power as slip turns into a macro-slip phenomenon.

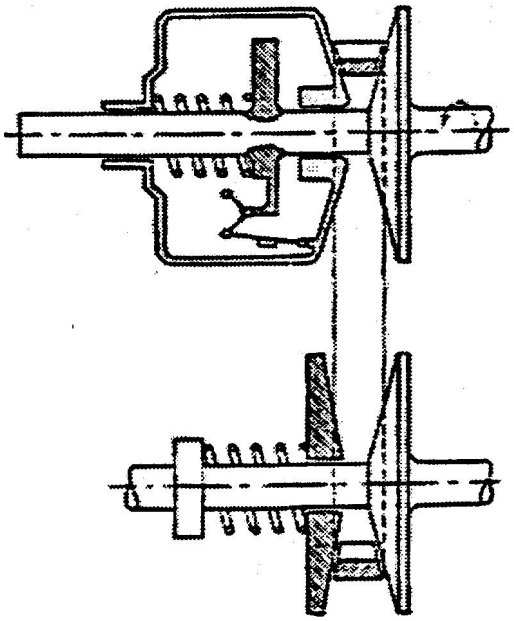

Source: Lu (1998, page 9).

Figure 2.6: V-belt CVT

For optimal use of the transmission, a clamping force depending on the transmitted torque is necessary. A V-belt CVT is mostly used for passenger car applications as the power transfer is limited. Moreover, the continuous existence of micro-slip causes a relative short lifetime of the belt. As already highlighted, the principal disadvantage of a belt driven CVT is the low torque transfer. Especially at low speeds, this kind of transmission system is the limiting factor in the power train. Moreover, the low efficiency (around 70%) reduces the effect of a more optimal use of the engine.

Belt driven CVTs also exist in other forms. A metal pushing V-belt is frequently used in vehicle applications. These belts allow a larger torque transfer. Furthermore, as the metal belt consists of a large number of slightly movable blocs around two steel band, the belt is less deformed and thus the efficiency is increased up to 80% (Lu, 1998).

2.2.2 Hydrostatic transmission system

A hydrostatic transmission consist of hydraulic pump and hydraulic motor connected in series with high-pressure lines (typically 350 bar) presented in Fig. 2.7. The pump creates hydraulic power (pressure and flow rate) while the motor converts the hydraulic power into mechanical power (torque and speed). In Fig. 2.7, the hydrostatic transmission is composed by a variable displacement pump and a fixed displacement motor. Nowadays most hydrostatic transmission include two variable units. In this way a complete independent control of the ICE speed and wheel speed is allowed. It is even possible to operate the pump as a motor and vice versa. This allows hydrostatic breaking. The main advantage of a hydrostatic transmission is its simplicity. It is composed of very reliable components which are well known on the market. Besides, it provides pressure energy for auxiliary

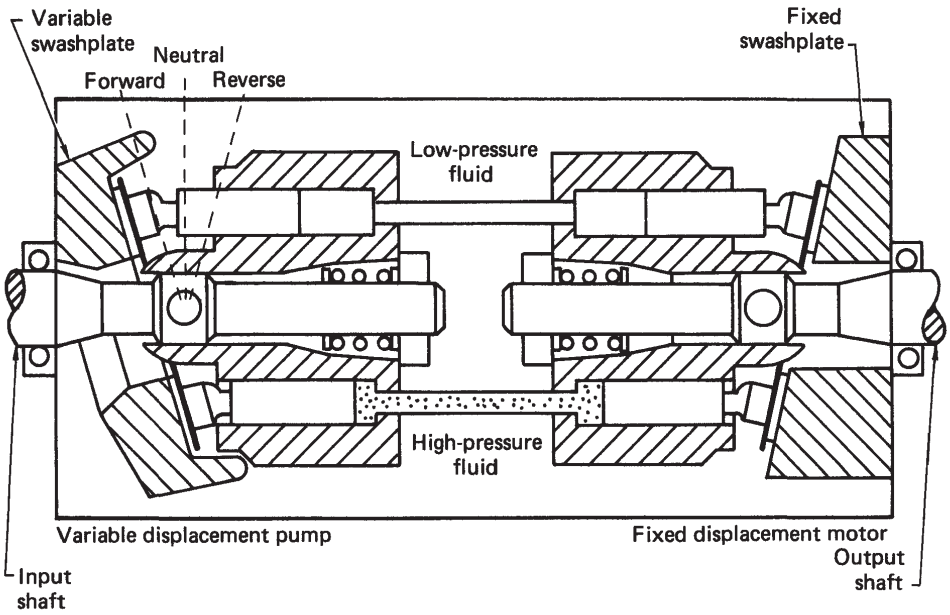

Source: Beachley et al. (1979, page 4).

Figure 2.7: Typical hydrostatic transmission system

hydraulic devices which is especially practical for off-highway applications. Additionally, using a hydrostat eliminates the use of a driving axis. The pump can be located close to the ICE, while the hydraulic motor is mounted close to the wheels. The main disadvantage of hydraulic transmission systems is their low efficiency, especially compared to gears (around 70 % in stead of 95 %). Another disadvantage of a hydraulic system is leakage. Consequently, hydraulic transmissions are less fitted for environments where leakage is an issue (Beachley et al., 1979).

2.2.3 Diesel-Electric-Electric transmission system

An electric generator-motor combination also makes a CVT (Fig. 2.8). This topology is quite similar to the hydrostatic transmission. The generator converts mechanical power into electrical power. The electrical power is then fed to an electrical motor, which converts it back to mechanical power. In the 1970's the first electrical transmissions were made including DC machines. Back then, the main disadvantages were the weight and size of two electrical machines. Right now, AC machines are used (i.e synchronous or asynchronous) connected to a DC bus via electrical converters. The power density the AC version is increased compared to the DC one but the converters are large since all power is converted twice. The efficiency of the electric system will be better than that of a hydraulic one. But as all power flows through the converters, the efficiency is relatively low compared to other electrical configurations (i.e. electrical-mechanical power-split).

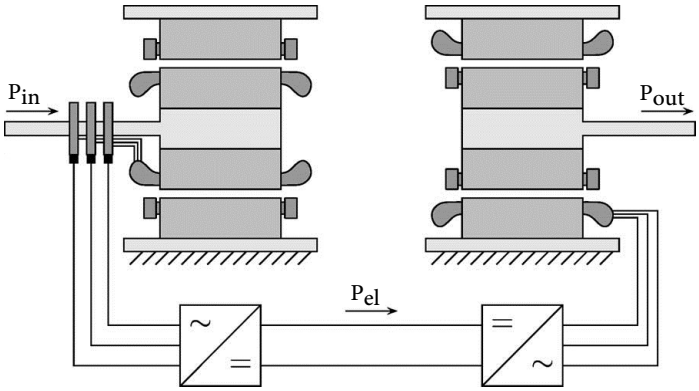

Source: Hoeijmakers et al. (2006).

Figure 2.8: Diesel-electric-electric transmission system

2.3 Power-split transmissions

Power-split transmissions usually consist of a mechanical power train in parallel to a variator (a CVT system) interconnected by a planetary gear train (PGT). The basic idea is to send only a part of the power through the continuously variable unit, while the remainder of the power is going straight through the mechanical path with high efficiency (Beachley et al., 1979). Depending on the position of the PGT, the system can be grouped into input-coupled (summing planetary) and output-coupled (divider planetary) systems as illustrated in Fig. 2.9.

(a) input-coupled **(b)** output-coupled

Source: Lu (1998, page 30).

Figure 2.9: Power-split arrangements

In the input-coupled power-split transmission, the PGT is at the output node and the coupling is at the input node. In the output-coupled type, the input node is the PGT and the output node is the coupling (Linares et al., 2010). According to Lu (1998), a power-split function makes it possible to expand the CVT application to heavy-duty vehicles (i.e belt driven CVT) or to lower the losses of CVT systems (i.e. hydrostat). For each configuration, there are 3 modes of operation:

- Non-regenerative (Power-split): the power flow in each of the two paths is lower than the input power.
- Mechanical regenerative (negative circulating power): power flow through the fixed path is larger than the input power, the power flow through the variable path is backwards.

- Variable regenerative (positive circulating power): power flow through the variable path is larger than the input power, the power flow through the fixed path is backwards.

Many studies (Beachley et al., 1979; Linares et al., 2010; Lu, 1998; Renius et al., 2005) have been performed on the operation of power-split transmissions. These studies show that the operation principle of the two types is completely different. Figs. 2.10a and 2.10b discuss the operating principle of the divider and the summing planetary type respectively in function of the transmission ratio R_t.

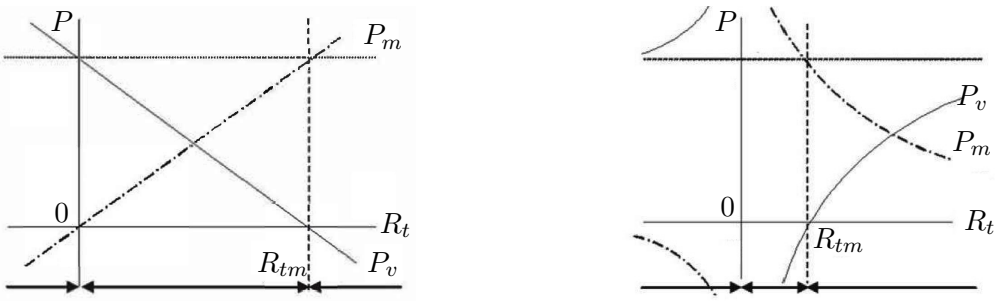

(a) Divider platetary (output-coupled)

(b) Summing platetary (input-coupled)

Source: Linares et al. (2010, page 6).

Figure 2.10: Operating principles of power-split transmissions

In divider planetaries, the power is non-generative up to the lock-up point (when all power is transferred through the mechanical path). At very low transmission ratios R_t (i.e. output speed divided by input speed), the power flow only uses the variable path, P_v. When transmission ratios higher than the lock-up point (R_{mt}) are reached, the power flow through the mechanical path (P_m) is higher than the input power (mechanical regeneration). The power excess is fed back to the input through the variator (negative variator power). In Fig. 2.10a, it is seen that the power distribution is a linear function of the transmission ratio. This is advantageous for the control of the system.

On the contrary, very low transmission ratios using summing planetaries require a high portion of mechanical regeneration. The power flow through the variable unit is strongly backwards. In this case, the transmission ratio at the lock-up point is lower than that of the mechanical path. When the transmission ratio is further increased, the power flow tents to be transferred by the variable unit. Renius et al. (2005) makes a theoretical estimation of the efficiency of both input- and output-coupled systems based the following efficiencies of the subsystems:

- 97 % for the straight mechanical path
- 85 % for the variable unit (including the PGT)

Figs. 2.11a and 2.11b present the results of input- and output-coupled systems respectively.

For input-coupled systems, the efficiency is typically hyperbolic increasing. The low efficiency near start-up is due to the huge amount of circulating power. The efficiency for output-coupled systems

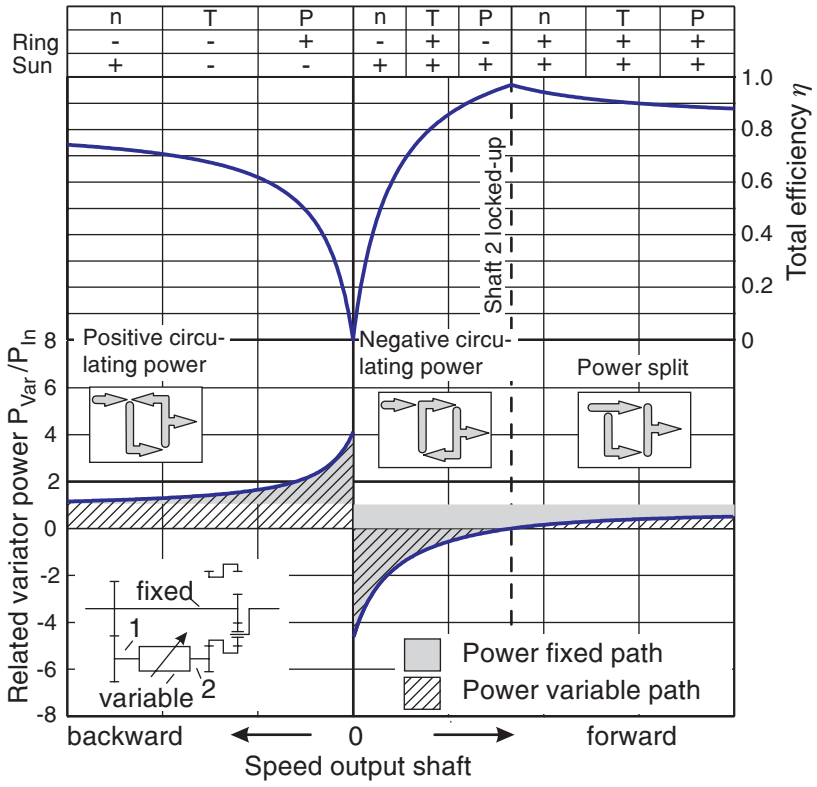

(a) Input-coupled

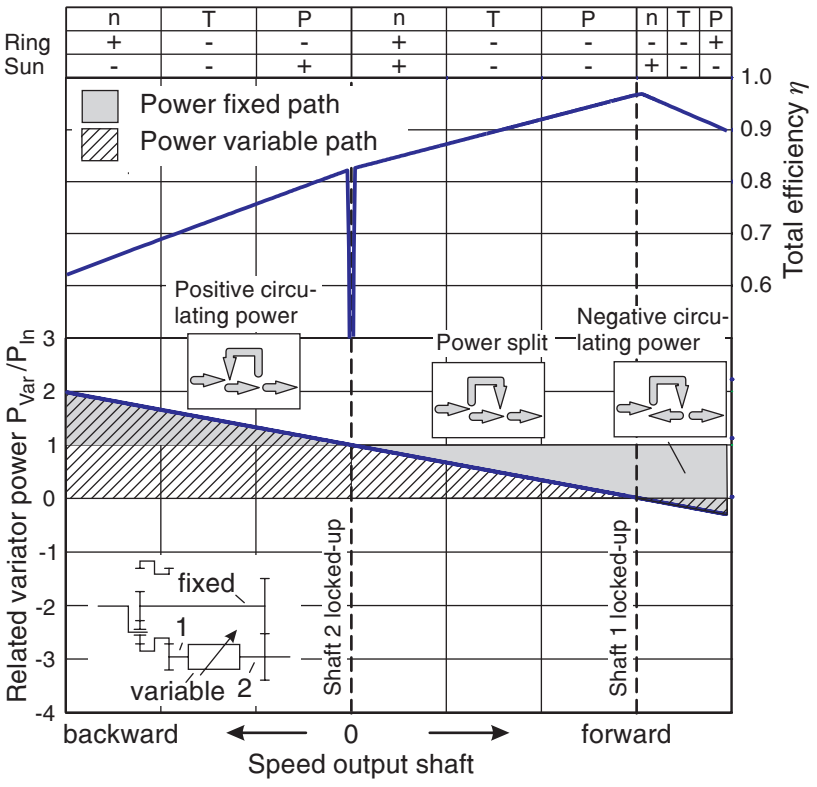

(b) Output-coupled

Figure 2.11: Power characteristics and efficiency for power-split systems

Source: Renius et al., 2005.

is linear increasing to the lock-up point as the fraction of power through the variator decreases linearly. According to Lu (1998), input-coupled (summing planetaries) systems have higher overall efficiencies, mainly because of two reasons:

- The variable unit is located at the high speed (input) side, which tents to be a more efficient unit.
- An appropriate design allows the operation region to be restricted close to and beyond lock-up point. In this region, input-coupled systems transfer more power through the mechanical path than their output-coupled equivalent.

A disadvantage of input-coupled systems is the need for a clutch system after the power-split unit, as the unit can not be operated at very low output speeds due to the very low efficiency.

As explained in this section, both input- and output-coupled systems have their advantages. The choice of the system depends mostly on the application. In the following sections some examples of power-split continuous variable transmission systems are discussed.

2.3.1 Belt driven power-split CVT

In Lu (1998), a complete model of a power-split transmission using a belt driven continuously variable transmission (PS-CVT)is made . As explained in section 2.2.1, the belt is the limiting factor for power transfer in vehicles. Especially at low speeds when the torque is high, the use of a belt is very disadvantageous. An input-coupled power-split transmission is the best choice for this variator, as the power transmitted through the variator is low at low output speeds and the belt driven CVT is located at the high speed side of the power-split unit. Lu (1998) studies a complete car model using the PS-CVT as shown in Fig. 2.12 .

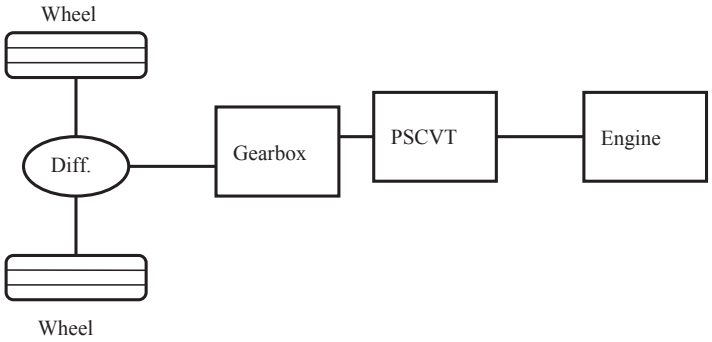

Source: Lu (1998, page 69).

Figure 2.12: Car model PS-CVT

The paper investigates the acceleration of a certain car. It is concluded that the transmission efficiency using PS-CVT is between 85 % and 93.5 %, compared to 70 % - 90 % of a shaft-to-shaft CVT configuration. The use of a power-split thus certainly increases efficiency. Moreover, at low

speed, the belt carries only 44 % of the total input power which certainly decreases the load on the belt.

2.3.2 Fendt Vario

The first commercial power-split continuous variable transmission was produced by Fendt in 1996: the Fendt Vario. The Vario transmission system is an output-coupled hydrostatic CVT system. A schematic overview of the transmission unit is given in Fig. 2.13. The engine power (orange) is split into a hydraulic path (green) and a straight mechanical path (blue) by means of a planetary gear set. These three power flows are the basic elements of the power-split transmission. Additionally, there are two other power paths presented in Fig. 2.13: a four wheel drive (yellow) connected to the output shaft, and a PTO drive (purple) directly connected to the motor for auxiliary tools.

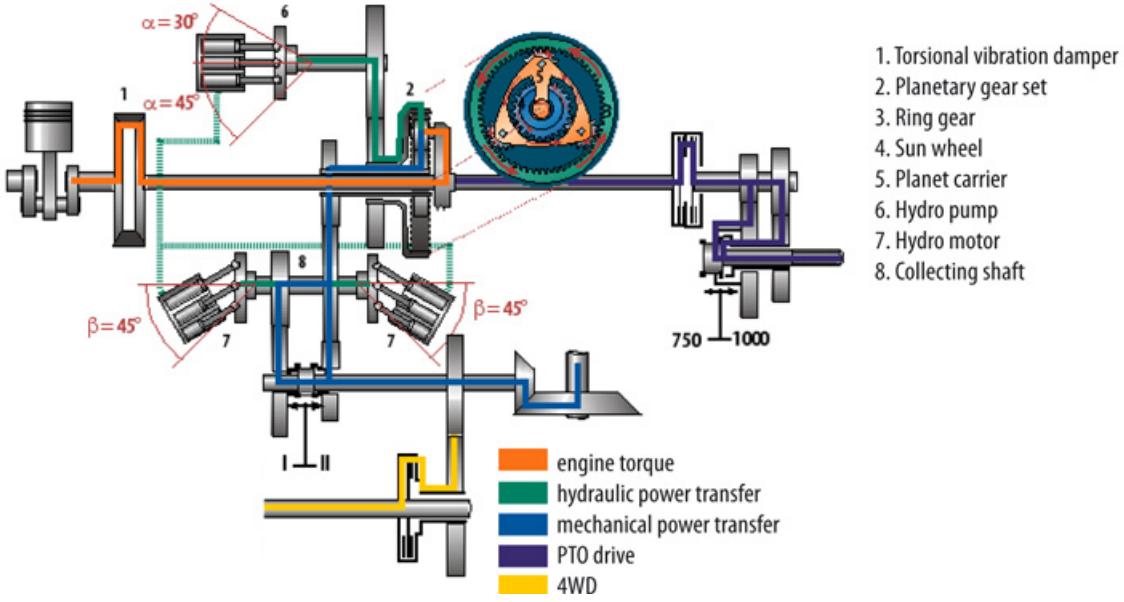

Source: http://www.fendt.co.uk/.

Figure 2.13: Fendt Vario transmission system

A more detailed explanation of the Fendt Vario's working principle is given using Fig. 2.14. The engine is connected to the sun wheel of the PGT, the wheels are connected to the planet wheel and the hydraulic pump is connected to the ring wheel of the PGT. At standstill (Fig. 2.14a), there is no deflection of the pump. The hydraulic path is the path of least resistance and all power is transmitted hydraulically. But, because the pump does not deliver oil, the wheels do not move. When the pump swings out (Fig. 2.14a), it delivers oil and feeds the hydro-motor which is at maximum deflection. The wheels start to move, but the power is still transferred more or less hydraulically. In the first phase of acceleration, the hydro-pump is swung out further, which means that it delivers more oil. The hydro-motor receives more oil and the tractor moves faster. When the pump reaches its maximum deflection angle, as shown in Fig. 2.14c, tractor can only be accelerated more by decreasing the deflection angle of the hydro-motor (Fig. 2.14d). This increases

the resistance of the hydraulic path. The ring wheel of the PGT slows down, whereas the planet wheel is accelerating and so is the tractor. When the deflection of the hydro-motor reaches its zero value (Fig. 2.14e), there is no more oil flowing through the hydraulic path and all power is transferred mechanically.

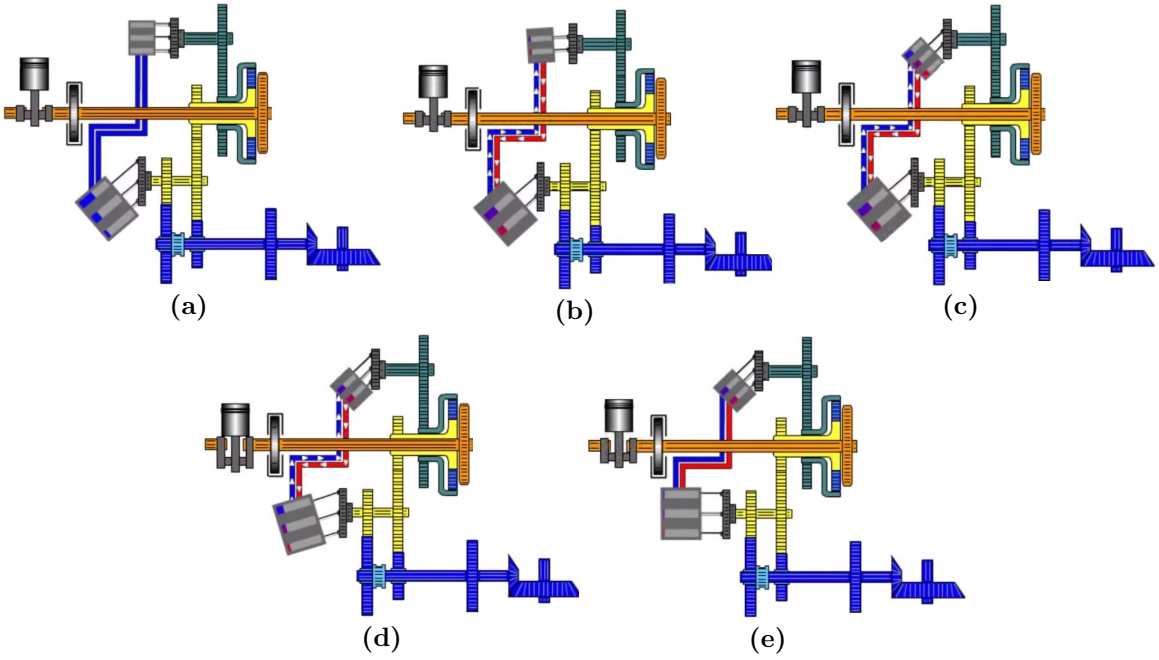

Source: https://www.youtube.com/watch?v=b_-LL0sCT-k.

Figure 2.14: Fendt Vario operation principle

As described in previous paragraph, the hydrostatic power portion is near 100 % in the starting point, but zero at top speed. The total speed range to the wheels of a Fendt Vario tractor is divided into two parts or ranges in addition to the power-split device. Range 'Low' covers speeds upto 32 km/h, range 'High' up to 50 km/h. The top speeds are near the lock-up points. Speed potential above the lock-up point is not used in order to prevent circulating power in the forward mode. Being an output-coupled unit, the Vario system requires very high maximum hydrostatic power (especially at low speeds) and thus consists of large units. Until 1995, all commercial units of such a high power had been quoted to be too poor in efficiency to meet overall efficiency targets. Therefore, Fendt developed its own hydraulic units: 45 degree variable bent axis units, with efficiencies up to 95 % in their best operating point. This led to a very high overall efficiency of the power train, even with high hydrostatic power fractions at low speeds.

Fig. 2.15 shows the overall efficiency at full load of the Fendt 926 Vario, the first commercial tractor using a Vario transmission system. The target on the figure is the total drive line efficiency (engine to wheels) for full load of stepped powershift transmissions. Renius et al. (2005) states that the efficiency of a continuously variable transmission should reach at least this value to be competitive on the tractor market. As seen on Fig. 2.15, the efficiency of the Fendt Vario is well above the proposed target. Therefore, the Vario system is known to be a very good CVT system.

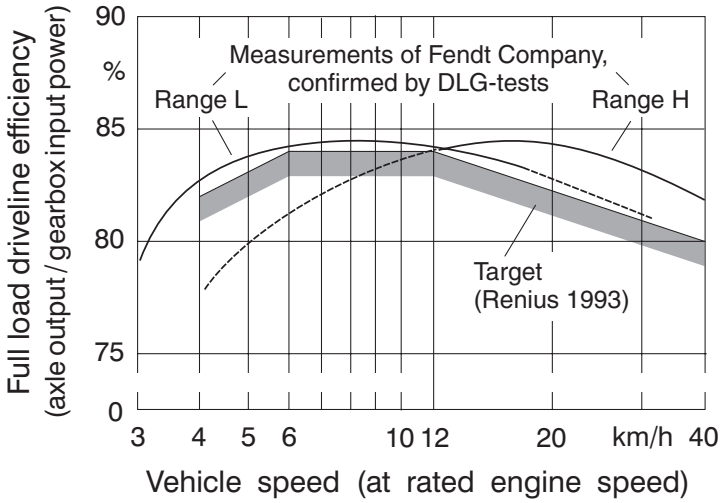

Source: Renius et al. (2005).

Figure 2.15: Fendt Vario transmission system efficiency

2.3.3 Dana Rexroth HVT

Unlike the Fendt Vario, the Dana Rexroth HVT is an input-coupled power-split transmission. Fig. 2.16 reveals that the power of hydrostatic unit and the power of the mechanical path is added in a PGT at the output axis. According to Fig. 2.11a, the power thought the hydrostatic unit of an input-coupled PS transmission is highly negative at standstill. Consequently, the efficiency is

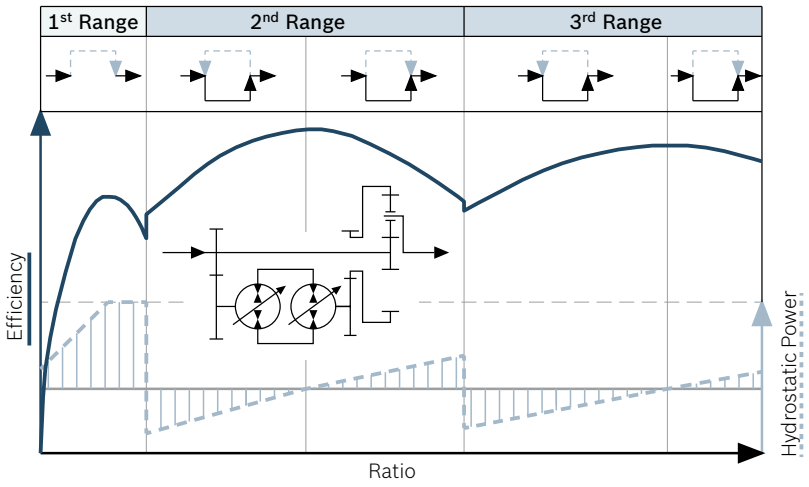

Source: boschrexroth.com.

Figure 2.16: Dana Rexroth Three Range HVT

very bad at low output speeds. To overcome this issue the HVT form Dana-Spicer is combined with a three range classical powershift gearbox. As seen on Fig. 2.16, the first range of the gearbox is designed such that the HVT works in overdrive mode. Both power through the mechanical and hydrostatic path are positive. In the remaining two stages the lock-up point is located in the

middle of the ranges. Because of this, the power through the hydrostatic units is strongly reduced. Therefore, the hydrostatic units are much smaller -and thus cheaper- than in a Fendt Vario system. Due to the low hydrostatic power fraction in all operating speeds, the Dana Rexroth has a very high efficiency, even at very low vehicle speeds. Furthermore, Dana has proven that the design of the first range reduces the power required from the ICE with 30 % to achieve maximum tractive effort at standstill. This is a considerable advantage over a hydraulic torque converter.

Fig. 2.17 compares the a HVT to a classical torque converter transmission. Whereas the torque converter can only work in a part of the engine map, the HVT covers both the complete speed and torque range of the ICE. Moreover, the torque can even be negative, which allows to hydrostatic braking. Fig. 2.17b compares a full and a partial load situation at constant vehicle speed. As seen, using a classical torque converter the engine speed is not changed at partial load, since the speed of the engine is directly related to the speed of the wheels. On the contrary, HVT optimizes the operating point of the diesel engine by decoupling the engine speed from the drive speed, resulting in considerable fuel savings.

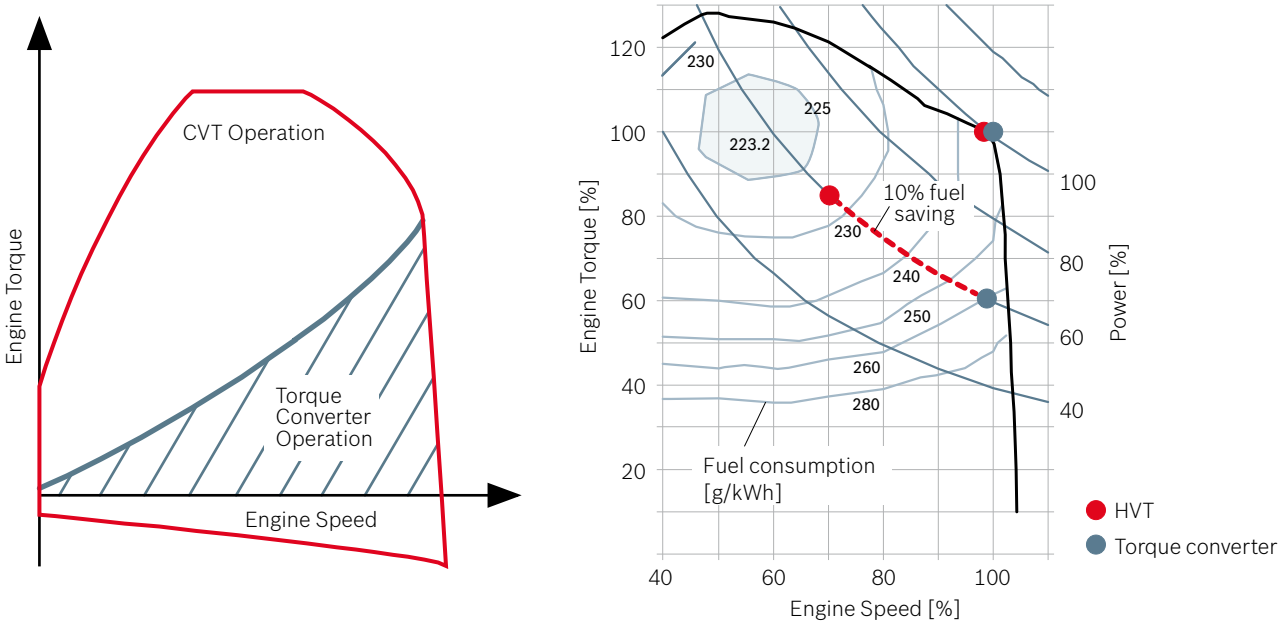

(a) Input-coupled

(b) Output-coupled

Source: boschrexroth.com.

Figure 2.17: Example of CVT/HVT potential compared to torque converter transmission

2.3.4 Toyota's Hybrid Powertrain

One of most well known power-split transmissions for vehicles is the hybrid powertrain of Toyota, first used in the Toyota Prius series. The transmission unit is an output-coupled electro-mechanical power-split system presented in Fig. 2.18. The planetary gear set divides the engine's drive force into two forces: one that is transmitted via the ring gear to drive the axle shaft and the other

that drives the generator through the sun gear. The electrical force, produced in the generator, is reconverted into mechanical force through the motor which is connected to the ring gear of the planetary gear set.

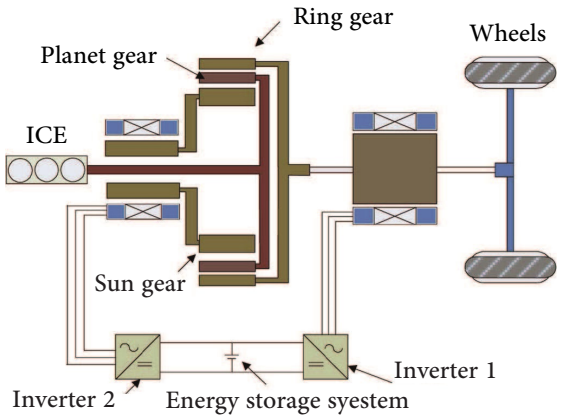

Source: Niu et al. (2013).

Figure 2.18: Schematic representation of the Toyota Hybrid System

Toyota's powertrain is likely to be today's best developed power-split transmission, since it has been in production for more than a decade and has proven its effectiveness many times. According to Sasaki (1998), Toyota's Hybrid System realized approximately twice the fuel economy of the conventional model and exhibited a high level of potential in terms of minimizing exhaust emissions. The powertrain includes a battery which has several advantages over a hydraulic variator (without energy storage):

- The engine can be started and stopped at any time while the vehicle is being driven;
- The engine can be controlled always in its optimum power point;
- To meet breaking demand, the system balances regenerative and mechanical operation.

Although the electro-mechanical power-split transmission of Toyota has become well-established technology in the passenger car market, it has some shortcomings to be adopted by the off-highway market. The main obstructions are:

- Robustness;
- High torque at low speeds requires high currents;
- Two electrical machines dimensioned for the full power range of the machine are heavy and expensive for increasing power units.

2.4 Conclusions

Concluding this chapter, Table 2.1 gives an overview of the main (dis)advantages of the described transmission systems.

	Advantages	Disadvantages
Friction clutch	• simple design • cheap	• heat generation • torque loss while shifting • transfer of vibrations
Hydraulic torque converter	• simple design • vibrational damping • overload protection	• low efficiency • leakage • torque reduction during shifts
VariGlide	• wider range of speed ratios • more efficient use of ICE	• traction fluid • limited power transfer
Belt driven CVT	• infinite number of transmission ratios • optimal engine use	• increased wear • low efficiency (70 %) • limited torque transfer
Hydrostat	• optimal engine use • hydrostatic breaking • simplicity • high reliable components	• low efficiency • leakage
Diesel-Electric	• optimal engine use • flexibility	• large converters • relatively low electrical efficiency
Belt driven PS-CVT	• increased torque and power limit • increased efficiency	• still high wear
Fendt Vario	• optimal engine use • no powershifts • very high efficiency in all operating points • fuel savings	• large hydrostatic units • large portion of hydraulic power at low speed and high torque
Dana Rexroth HVT	• optimal engine use • smaller hydrostatic units • fuel savings	• no fully continuously variable transmission
Toyota Hybrid System	• optimal engine use • compact • hybrid vehicle	• less suited for off-highway • two electrical machines

Table 2.1: Overview of transmission systems

Chapter 3

Electromagnetic continuously variable transmission

In Chapter 2, transmissions systems are studied. In section 2.3.4 an electrical-mechanical power-split transmission is already presented by means of the Toyota Hybrid Powertrain. This chapter describes several other electrically continuous variable transmissions.

3.1 Previous work

As already explained in section 2.2.3, a CVT can be made connecting two electrical machines in series (Fig. 2.8). In this case, an unconventional generator with the squirrel-cage winding on the stator is used. The electrical power is withdrawn from the rotor by means of sliprings. The electrical power is then rectified in the inverter and added to the DC-bus. This DC-bus is connected through another inverter to an induction motor which converts the electrical energy back to mechanical energy (Hoeijmakers et al., 2006). The configuration holds all advantages of a CVT. Additionally, the system is easy to be controlled, because the generated power equals the engine power. Although it is an easy system, the configuration is quite heavy and expensive for off-road applications. Two electrical motors are required and, moreover, all power is converted twice in the inverters, which leads to tremendous electrical losses.

When the stator of the generator is connected to the rotor of the motor an electrical-electromagnetic power-split is realised, as shown in Fig. 3.1. This is the basic idea of an EVT. The power is partially transferred electromagnetically through the airgaps in the device, partially electrically through the converters. The device consists of a primary machine which receives the power P_{in} and functions as a power-split device, and a secondary machine in which the power flows of the two paths (direct and electric) are summed again. It can thus be concluded that an EVT is inherently an output-coupled device. For further explanation the machine is considered to be lossless. The electrical power withdrawn from the primary machine is written as:

$$P_e = (\Omega_{in} - \Omega_{out})\, T_{f,in} = (\Omega_{in} - \Omega_{in})\, T_{in} \tag{3.1}$$

with:

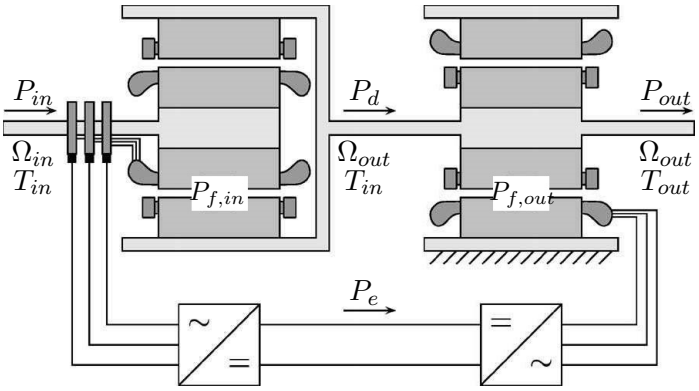

Source: Hoeijmakers et al. (2006, page 2).

Figure 3.1: Machine interconnection: basic idea of EVT

- Ω_{in} and Ω_{in}: the rotational speed of the input and output shaft respectively;
- T_{in}: the mechanical input torque;
- $T_{f,in}$: the electromagnetic torque in the primary machine.

The fraction of the power that is transmitted directly to the secondary shaft is:

$$P_d = \Omega_{out} T_{f,in} = \Omega_{out} T_{in} \tag{3.2}$$

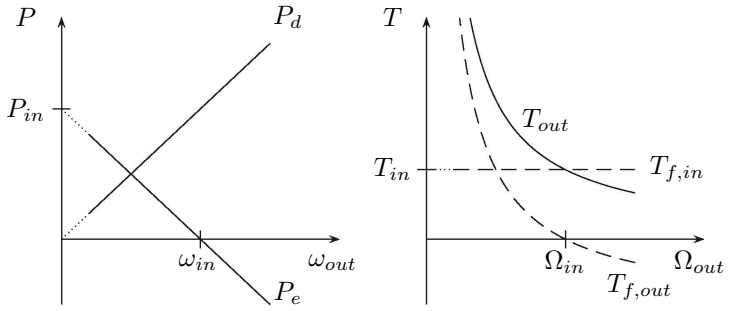

Source: Hoeijmakers et al. (2006, page 2).

Figure 3.2: Basic idea of EVT: power and torque flow

The power P_e is the power flow through the electrical converters with relative high losses. The power P_d is the power flow directly passed from the primary rotor to the secondary rotor with relatively low losses. The output torque of the device T_{out} is consequently composed out of the electromagnetic torque $T_{f,out}$ of the secondary machine and the air-gap torque the primary machine $T_{f,in}$:

$$T_{out} = T_{f,in} + T_{f,out} = T_{in} + \frac{P_e}{\omega_{out}} = T_{out} + \frac{\omega_{in} - \omega_{out}}{\omega_{out}} T_{in} = \frac{\omega_{in}}{\omega_{out}} T_{out} \tag{3.3}$$

Eq. (3.3) corresponds to the output shaft torque if losses are neglegted. The equations agrees with the power balance of the system. The power and torque fractions, presented in previous equations, are shown in Fig. 3.2 in function of the output speed. It is noticed that the power fraction transferred electrically linearly decreases until the output speed reaches the input speed. This characteristic corresponds, as already mentioned, to an output-coupled power-split device (Fig. 2.10a).

For practical implementation, the two electrical machines can be integrated into one device, as displayed in Fig. 3.3. The machine consequently consists of a stator and two rotors. In the following, the outer rotor will be called 'the interrotor', while the inner rotor will be referred to as 'the rotor'. Corresponding to the interconnected machines of Fig. 3.1, the input and output shaft of the integrated device are connected to the rotor and interrotor respectively. Hoeijmakers et al. (2006) studies this device in detail. Although the two machines are integrated into one single device, the machine is electromagnetically still treated as two separated machines, since it consists of two cage windings and a considerably wide yoke in the interrotor. Consequently, the conclusions for both the interconnected and the integrated configuration are similar.

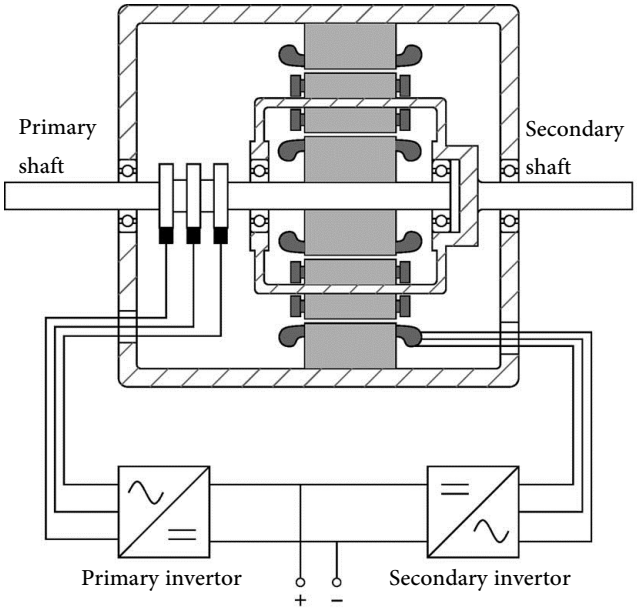

Source: Hoeijmakers et al. (2006, page 5).

Figure 3.3: EVT by Hoeijmakers

3.2 Proposed EVT design for compact implementation

An updated design of the EVT by Hoeijmakers et al., 2006 is proposed by Druant et al., 2014 and shown on Fig. 3.4 . In this design, the interrotor is constructed by only one squirrel-cage. The device can not be treated any more as two electromagnetically isolated machines. Instead a new control algorithm is developed. Being a CVT system and an electrical machine, this transmission system is expected to have the following advantages over usual transmission systems and previous

electrical CVT systems:

- High efficiency in all operating points;
- Possibility to switch gears under torque load;
- Wider range of output torque and speed;
- Overload protection (no mechanical connection between wheels and ICE);
- An electromagnetic-electric power-split leads to smaller electrical converters;
- Very high power density, since only one cage is used;
- Relatively cheap, since no expensive permanent magnets are used.

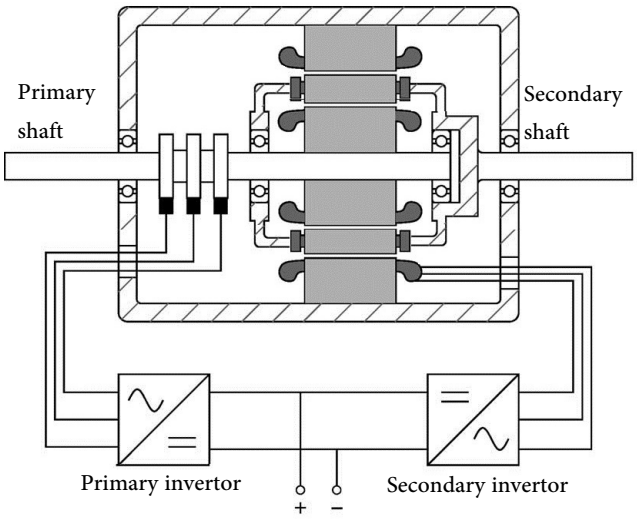

Source: based on Hoeijmakers et al. (2006, page 5).

Figure 3.4: EVT: proposed design for compact implementation

3.3 Other EVT configurations

The literature describes several other EVT systems. This section gives a short overview of several lay-outs, together with their basic working principles and (dis)advantages. For a more detailed explanation is referred to the corresponding papers.

3.3.1 Double layer permanent magnet EVT

Sun et al. (2009) proposes a double layer permanent magnet electrical variable transmission. Fig. 3.5 shows a schematic overview of the core design. The device consists of three parts, namely a three-phase stator, a wound three-phase inner rotor, and a PM outer rotor. As the device is intended to

be adopted in wind turbines, a PM outer rotor has been chosen. The advantages of a PM outer rotor over a squirrel-cage winding are: higher power density, high efficiency and easy control. On the other hand, a PM outer rotor is much more expensive than its induction equivalent, which makes it less interesting to be adopted in the automotive industry. Moreover, the PMs are less reliable during shock load and demagnetisation constitutes a problem. The working principle is basically the same as the EVT proposed by Hoeijmakers et al. (2006) explained in section 3.1.

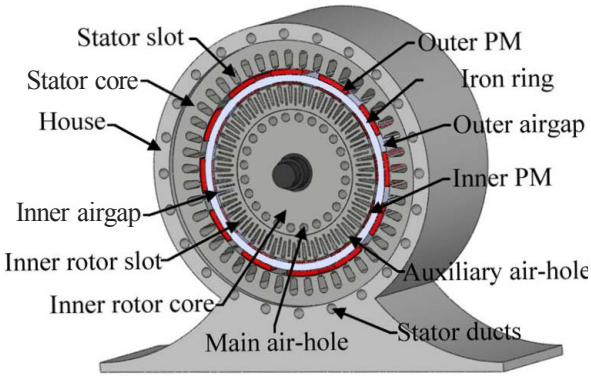

Source: Sun et al. (2013, page 2).

Figure 3.5: Double layer permanent magnet EVT

3.3.2 Magnetic gear integrated permanent magnet brushless machine

Liu et al. (2014) introduce another EVT topology. The main advantage over previous designs is the absence of the slip rings which significantly decreases maintenance. The overall structure and core design is presented in Fig. 3.6.

The design of the machine is mainly derived from a coaxial magnetic gear. The stator embeds two sets of windings. Additionally, there are three rotors in the machine: a PM outer rotor, a PM inter rotor and a flux-modulating ring of ferromagnetic polepieces (FMPs). Winding 1 and the inner PM rotor constitute a conventional PM motor with a low number of pole-pairs N_{ri} (i.c 5 pole-pairs), whereas winding 2 and the outer PM rotor constitute a PM motor with a high number of pole-pairs N_{ro} (i.c 22 pole-pairs). As the inner rotor, the FMPs and the outer rotor compose a magnetic gear, the number of FMPs is:

$$N_{FMPs} = N_{ri} + N_{ro} \tag{3.4}$$

Due to the introduction of N_{FMPs} FMPs, the harmonic field of the inner rotor is modulated to produce the dominant harmonic field of the outer rotor. Consequently, torque can be transmitted from the inner rotor or the FMPs to the outer rotor. Additionally, power of the rotor can be extracted without use of any brushes. On the other hand, the introduction of harmonics leads to tremendous harmonic losses, which is the main obstruction for practical implementation.

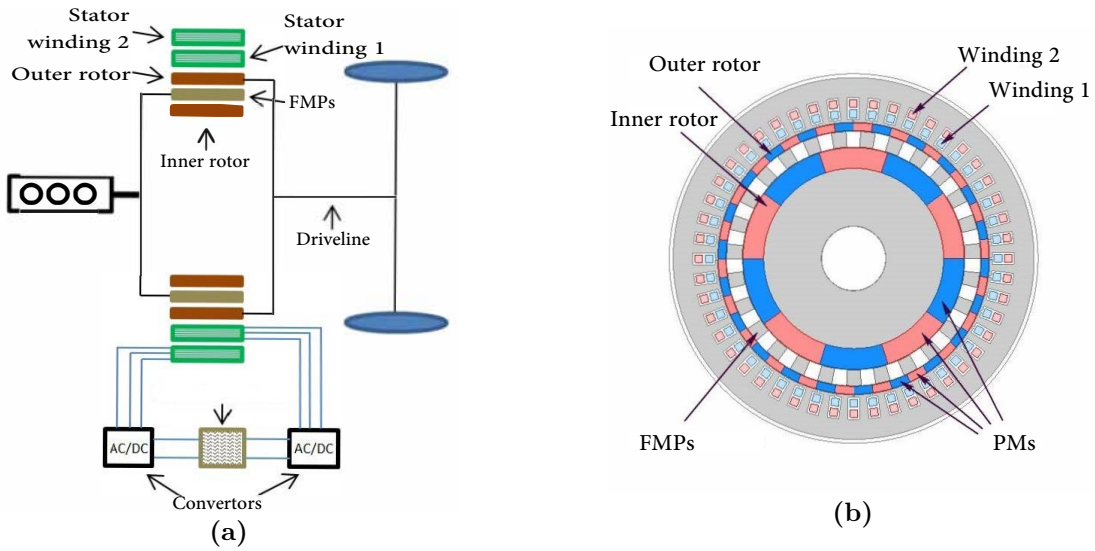

Source: Liu et al. (2014, page 2).

Figure 3.6: Magnetic gear integrated permanent magnet brushless machine

3.3.3 Doubly fed dual-rotor permanent magnet machine

Similar to the previous paragraph, Niu et al. (2013) present a another brushless EVT system. The structure and lay-out of the core are displayed in Fig. 3.7. Unlike the design of Liu et al. (2014), the device does not have a FMP ring. Instead, the PM rotors are of a special type. The PMs in the rotors have the same direction of magnetization (radially outward) alternated with equally inset ferrite segments. The number of pole-pairs of the primary stator are chosen such that the inner rotor, outer rotor and primary stator form a magnetic gear. In this way, the stator poles can modulate the low harmonic component of the inner airgap magnetic field to produce the specific high harmonic component in the outer airgap. The magnetic gearing effect introduces thus a power-split. A part of the power is transmitted directly from the input shaft (outer rotor) to the output shaft (inner rotor), while the remainder is converted into electrical power and then fed to the secondary stator winding which is designed to assists the torque on the output shaft.

The advantage of this system over the system with a FMP ring is the reduced number of airgaps. On the other hand, one has to take in account harmonic interaction effects to be able to control both input and output shaft speed independently.

3.4 Possible applications

The presented EVT systems are prospective for diverse applications. In series connection, it is possible to replace the hydrodynamic torque converter or eventually the whole transmission system. In parallel, the EVT could be used as a variator in power-split transmission. For example, the EVT could replace the hydrostatic unit in a hydro-mechanical power-split transmission. Although the focus in this master paper is on vehicle application, the EVT system could also be used in other

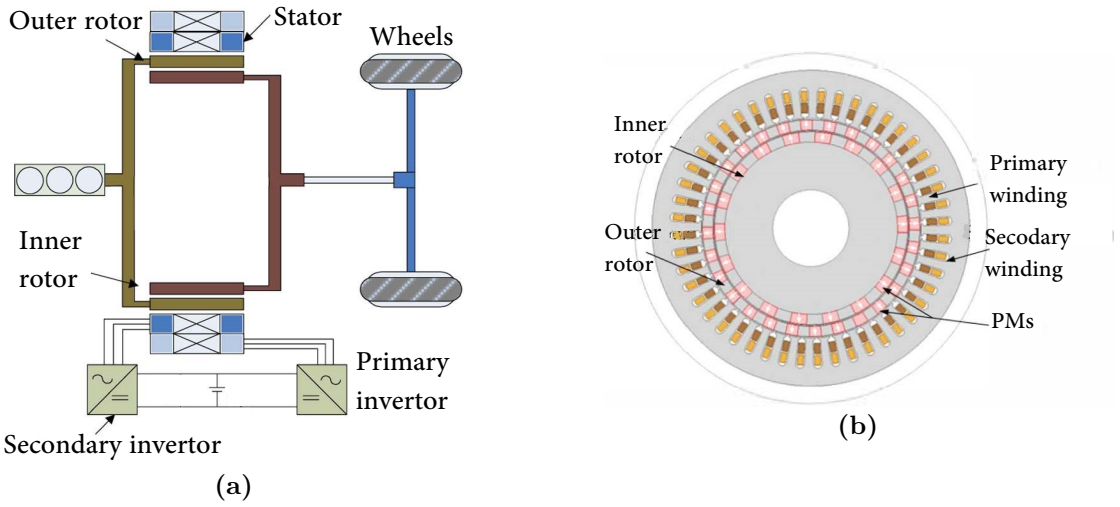

Source: Niu et al. (2013, page 2).

Figure 3.7: Doubly fed dual-rotor permanent magnet machine

applications. As already highlighted in section 3.3.1, Sun et al. present the use of an EVT in wind power generation systems, but also applications in the industry, where currently a CVT is adopted, are possible.

Since this master paper is in cooperation with Dana-Spicer, it focusses mainly on off-highway vehicle applications. Moreover, in this work, the design focusses on the replacement of a hydrodynamic torque converter in off-highway transmission systems. The main reasons to focus on this kind of applications are:

- The present-day hydrodynamic torque converter is the component of the transmission system where most of the losses occur.
- The replacement of a torque converter by an EVT is only a small change in current transmission systems, the well developed gearbox system could be maintained.
- A series implementation allows to take full advantage of the benefits of an EVT system. In a parallel connection, the EVT is only partially used and thus the gain over other existing systems would be less.

Chapter 4

Finite element analysis on electrical machines

For the last 25 years, electrical machines have been studied in detail using finite element analysis (FEA). The development of solution methods and the growth of computer capacities have made it possible to solve more and more complex problems. The FEM has proven to be very efficient when dealing with complicated geometries (Arkkio et al., 1987).

This chapter gives an overview of recent studies. Since in this master thesis a finite element analysis is performed on an electrical device, a review of existing studies is the basis of the model set-up for the EVT. The modelling methods introduced in the next sections are intended to give the reader different strategies on performing a finite element analysis. For an analytic description of these methods, the reader is referred to Chapter 5 where the strategies are applied on the investigated EVT.

4.1 Mean idea

The main idea of FEA is to divide a large and complex problem into small and simple problem areas. The small problem area is defined as an element. The solution in each element is approximated using a function, generally a polynomial. The polynomial turns the complex problem into a simple matrix representation for each element. Combining the elemental matrices leads to the global system matrix. When the boundary conditions are applied, the global system matrix can be solved (Silwal et al., 2012).

4.2 Equations of the electromagnetic field

All electromagnetic phenomena are covered by Maxwell's equations subjected to certain boundary conditions. Maxwell's equations are a set of equations, written in differential or integral form, stating the relationships between the fundamental electromagnetic quantities. These quantities are:

- The electric field intensity, $\boldsymbol{E}$

- The electric displacement or electric flux density, $\boldsymbol{D}$
- The magnetic field intensity, $\boldsymbol{H}$
- The magnetic flux density, $\boldsymbol{B}$
- The current density, $\boldsymbol{J}$
- The electric charge density, ρ

Because the finite element method uses differential equations, the Maxwell equations are formulated in differential form. For general time-varying fields, the equations are:

$$\nabla \times \boldsymbol{H} = \boldsymbol{J} + \frac{\partial \boldsymbol{D}}{\partial t} \tag{4.1a}$$

$$\nabla \times \boldsymbol{E} = -\frac{\partial \boldsymbol{B}}{\partial t} \tag{4.1b}$$

$$\nabla \cdot \boldsymbol{D} = \rho \tag{4.1c}$$

$$\nabla \cdot \boldsymbol{B} = 0 \tag{4.1d}$$

The first two equations are mostly referred to as Maxwell-Ampère's law and Faraday's law respectively. The last two are the Gauss' laws in the electric and magnetic form respectively.

Another fundamental relationship is the equation of continuity:

$$\nabla \cdot \boldsymbol{J} = -\frac{\partial \rho}{\partial t} \tag{4.1e}$$

Out of these five equations only three are independent. Eqs. (4.1a) and (4.1b) completed with either eq. (4.1c) or eq. (4.1e) form independent systems.

4.2.1 Constitutive relationships

A closed system representation requires additional constitutive relationships describing the macroscopic properties of the medium. For nonlinear materials, these relationships are written in their generalized form.

$$\boldsymbol{D} = \epsilon_0 \epsilon_r \boldsymbol{E} + \boldsymbol{D}_r \tag{4.2a}$$

$$\boldsymbol{B} = \mu_0 \mu_r \boldsymbol{H} + \boldsymbol{B}_r \tag{4.2b}$$

$$\boldsymbol{J} = \sigma \boldsymbol{E} \tag{4.2c}$$

where $\boldsymbol{D}_r$ is the remanent displacement, which is the displacement when no electric field is present. The field $\boldsymbol{B}_r$ is the remanent magnetic flux density, which is the magnetic flux density when no magnetic field is present. ϵ_0 is the permittivity of vacuum, μ_0 is the permeability of vacuum, and σ is

the electric conductivity. In the SI system, the permeability of a vacuum is $4\pi \cdot 10^{-7}\,\mathrm{H/m}$, whereas the permittivity of vacuum equals $\frac{1}{36\pi} \cdot 10^{-9}\,\mathrm{F/m}$. The relative material properties are dependent on the material. Moreover, μ_r is also dependent on the saturation state of the material.

4.2.2 Two dimensional magnetostatic problem statement

In this paper only static magnetic fields are studied. The time dependent factors in eq. (4.1) are eliminated. Ampere's law for the static case equals:

$$\nabla \times \boldsymbol{H} = \boldsymbol{J} \tag{4.3}$$

Since the magnetic field $\boldsymbol{B}$ is divergence-free, the magnetic field density can be derived of a magnetic vector potential $\boldsymbol{A}$.

$$\boldsymbol{B} = \nabla \times \boldsymbol{A} \tag{4.4}$$

Consequently, the electrical field $\boldsymbol{E}$ can be written in function of an electric (scalar) potential.

$$\boldsymbol{E} = -\nabla\phi - \frac{\partial \boldsymbol{A}}{\partial t}\,, \tag{4.5}$$

which is reduced in a static analysis to:

$$\boldsymbol{E} = -\nabla\phi \tag{4.6}$$

In a general three-dimensional case, there are four unknown quantities (components of the vector potential and the scalar potential). These quantities depend on the three spatial coordinates and time. Because of the complexity of an electrical machine and the non-linearity of the problem, the task requires a lot of calculation force. Therefore, in the first analysis of an electrical machine, the model is simplified to a true two-dimensional problem. This approximation is only valid if the electrical machine would have an infinite axial length. In practice, there is need for adoptions of the two-dimensional model to include rotor skew and end-region effects.

In a two dimensional analysis, the magnetic field density can be expressed as:

$$\boldsymbol{B} = B_x \boldsymbol{e}_x + B_y \boldsymbol{e}_y \tag{4.7}$$

The magnetic vector potential is thus aligned with the z-axis.

$$\boldsymbol{A} = A_z \boldsymbol{e}_z \tag{4.8}$$

Therefore, eq. (4.4) is thus reduced to:

$$B_x = \frac{\partial A_z}{\partial y} \quad B_y = -\frac{\partial A_z}{\partial x} \tag{4.9}$$

4.2.3 Boundary conditions

Finite element analysis requires the imposition of the correct boundary conditions at the geometry edges and material properties to the different subdomains. Basically, there are two main boundary conditions, depending on whether the magnetic field is continuous or insulated.

The continuity boundary condition or Neumann condition implies the continuity of the tangential component of the magnetic field and is expressed as:

$$\boldsymbol{n} \times (\boldsymbol{H_1} - \boldsymbol{H_1}) = 0 \tag{4.10}$$

This condition is set to all interfaces between two different materials.

The magnetic-insulation boundary condition or Dirichlet boundary condition expresses that there is no flux through the boundary. As the flux density $\boldsymbol{B}$ is the rotation of the magnetic vector potential $\boldsymbol{A}$, the condition in 2D can be expressed as:

$$A_z = 0 \tag{4.11}$$

This condition is applied to all outside borders of the studied geometry as it is supposed no flux passes outside the machine.

4.3 Review of the field analysis

A detailed historical review of FEMs is described in Arkkio et al. (1987, page 18). The first efforts to solve magnetic field problems by FEA were made in the late 1960's. The study of electrical machines by finite elements was first applied on synchronous machines and DC-machines, as the regime operation of these machine types can be modelled by stationary fields. Nowadays, all kinds of electrical machines are modelled using FEM. The exponential growth of computing capacity has made it possible to investigate not only regime solutions but also transient phenomena. Moreover, since the early 1990s, it has been possible to model electrical machines in three dimensions as the computing capacity reached a sufficiently high level.

Although 3D models are frequently used these days, this chapter only describes 2D models because the EVT model is considered to be two-dimensional. As mentioned in the previous section, 2D models only agree with their 3D equivalent if their axial length is high in comparison to the other dimensions. In reality, the axial length of an electrical machine is mostly in the same order of magnitude as its diameter. The solution of 2D models has to be adapted in order to take into account 3D effects. The effect of end region reactances can be considerably high. Moreover the rotor is usually skewed, i.c. the rotor slots are not parallel to the shaft, in order to reduce torque harmonics.

4.4 FEM 'schools'

The literature describes both static and transient analyses. According to Dolinar et al. (1997), Williamson et al. (1990, 1991), and Zhou et al. (1998), there are two distinct categories or schools of finite elements methods of induction machines, depending on how they deal with the rotor currents.

In the first one, sometimes called the *'coupled circuit school'*, both stator and rotor currents are regarded as input currents for the finite element model. The field solution is then used to update the parameters of the model and to make a better estimate of the rotor currents in the next iteration. All effects of time variation are moved into the circuit equations. Besides, the effects of stator end-windings and rotor end-rings are dealt with in the same manner: by adding an appropriate impedance to the relevant circuit element. Moreover, as stator and rotor currents are input parameters of the model, it is easy to incorporate rotor skew into the model. The field solution of different rotor segments, which are shifted in phase, can be solved in parallel which significant reduces computing time (Williamson et al., 1990). The system is know to be weakly coupled as field and circuit equations are solved independently.

In the second category, the *'eddy-current school'*, only the stator currents are regarded as a source for the FE model. The rotor currents are treated as induced currents. The eddy-current formulation is incorporated into the finite element model. Circuit equations are then only used to relate the induced EMF in the stator winding to the currents flowing in that winding, and to the applied terminal voltage. Rotor end-ring effect require more careful consideration, as rotor currents are direct results of the FEA. The system is known to be strong coupled as both field and circuit equations are solved simultaneously.

Zhou et al. (1998) states there is a third category of finite elements method where only a single slot model is used to estimate the equivalent circuit parameters. As only a single slot for stator and rotor is modelled, the computing time is significantly reduced but the model needs periodic boundary conditions which requires considerable experience with FEM.

Both methods have their advantages and disadvantages. The circuit approach is claimed to be faster and more capable of incorporating 3D effects like end-ring resistances/reactances and rotor skew. On the other hand, it does not include deep bar effect (skin effect) in the rotor. Bar resistance and slot leakage reactance must be modified after the field solution is calculated. The eddy current approach is able to include deep bar effects into the model, but requires a longer calculation time and cannot accommodate rotor skew and additional impedances without difficulties. In order to include end resistances two possibilities exist:

- Electrical connection of the rotor bars by rotor loop equations;
- Modification of the rotor bar conductivity to include the effect of end-ring resistances.

4.5 2D assumptions

In different papers (Arkkio et al., 1987; Sprooten et al., 2007), only a 2D finite element analysis is made to reduce the calculation time. This hypothesis is acceptable when rotor and stator windings are not skewed and when the presence of inter-bar currents is not considered. Next to this, the following assumptions are made:

- Three phase balanced current flows;
- Uniform current distribution in the slots;
- Magnetic flux does not leak from the outer surface of the stator or the inner surface of the rotor core;
- Losses due to eddy currents are neglected. The eddy current loss varies with the square of the flux density, the frequency, and the thickness of the lamination. As the magnetic core of an electrical machine is made out of thin sheet isolated from each other, the eddy-current loss in the core material is usually low.
- Hysteresis losses are neglected. In reality, iron has significant hysteresis in its saturation characteristic. Consequently, the reluctivity is not a single-value function of the flux density but depends on the history of the material. However, it is believed that introducing hysteresis would complicate the model significantly. Therefore, effects of hysteresis are mostly included into the saturation characteristic and loss estimation of the material.

4.6 Saturation

The effects of saturation of the main flux path on the performance of electrical machines have been discussed in many papers in the literature, but there is no generalized analytic treatment of these effects. Some authors (Melkebeek, 2013) assume that the state of saturation is equal in both q- and d-axes, others (Brown et al., 1983) introduce fictitious fluxes/inductances to deal with saturation differences in both axes. In the latter case, the self-inductances in orthogonal axes are no longer equal. This cross-coupling between the two axes because of saturation of the main flux path is called inter-saturation or cross-saturation. In practice, there is a recognition of the importance of saturation and the existence of inter-saturation effects (Brown et al., 1983). One of the consequences of the difference of self-inductances is the existence of a reluctivity torque in turbo electrical machines.

4.7 Torque

The torque is a very important parameter in the design and analysis of an electrical machine. The finite element method provides an accurate way to evaluate the torque based on the electromagnetic

field distributions. The literature describes several methods to calculate the torque on an electrical device. In the following sections, a short overview of these different methods is given.

4.7.1 Maxwell stress tensor

The first and probably the easiest method to evaluate the torque yields the Maxwell stress tensor. This calculation requires only the local flux density distribution along a specific contour around the air-gap of the machine (Gerling, 2005). Unfortunately, the Maxwell stress tensor needs a very fine mesh in the airgap, since the tensor multiplies radial with tangential component of the magnetic flux density in the airgap. Under the teeth, the field is almost radial whereas, between the teeth, the tangential component of the flux is relatively high. The maximum sensitivity of the tangential component of the flux density on the discretization occurs in the area where the normal component has its maximum gradient, i.c. between the teeth (Mizia et al., 1988). For this reason, the product of radial and tangential components is even more sensitive to the discretization density. This causes spikes in the product of radial with tangential quantities. In order to calculate the torque well, one spike should cover multiple mesh elements and therefore the mesh density needs to be high. In section 5.6, an example is presented.

A method to improve the quality of the torque calculation consists of averaging the torque calculation on multiple closed contours in the airgap. A second method to improve the torque quality is presented by Arkkio et al. (1987). His paper proposes an evaluation of the Maxwell tensor on the complete airgap volume instead of on one single contour. Basically, this method averages an infinite number of torque calculations on different contours in the airgap.

4.7.2 Principle of virtual work

A second approach to torque calculation uses the magnetic co-energy method or the principle of virtual work. The electromagnetic torque equals the derivative of the magnetic co-energy with respect to the angular position at constant current. Gerling (2005) and Mizia et al. (1988) show that the magnetic co-energy is less dependent of the element mesh than the Maxwell tensor. The drawback of this approach is the need of two solutions with a little phase shift between the rotor positions which prolongs the calculation time significantly. Moreover, this method has numerical difficulties in distinguishing small changes in the large energy values (Mizia et al., 1988).

4.7.3 Magnetizing currents

A third approach is proposed by Kabashima et al., 1988. In this paper the force is determined by use of the magnetizing currents and the flux densities on the lines forming elements. The method is basically equivalent to the Biot-Savart Law and needs only one solution of the magnetic field. The technique of magnetizing currents has the advantage that the force distribution acting on the

object can be obtained (i.e. the force on each bar of a cage rotor can be calculated) and therefore can be used for a structural and vibrational analysis.

4.7.4 Maxwell stress harmonic filter

Another method described in literature is called the Maxwell stress harmonic filter (HFT) method, presented by Popescu (2006). The methods presented in above sections are all applicable to electromagnetic devices but non of them exploit the origin of the torque generation. The method described by Popescu (2006) allows to identify the source of the torque in function of the space harmonics. It is essentially an improved Maxwell stress torque computation as a direct derivation of the flux densities components form an analytical expression of the air-gap magnetic vector potential. As the numerical solution of the magnetic vector potential is approached by analytical expression, the torque computation is less dependent on the meshing density in the airgap. On the other hand, the method is strongly dependent on the number of harmonics that is used in the analytical approximation.

4.7.5 qd-Formulation

A last method to evaluate the torque is based on the qd formulation of an electrical machine:

$$T_e = \frac{3}{2} N_p \left(\psi_d i_q - \psi_q i_d\right) \tag{4.12}$$

where the qd flux linkage $\psi_{d;q}$ and the currents $i_{d;q}$ have been determined by applying the Park transformation on the phase quantities. This method is equal to the Maxwell HFT method restricted to the first harmonic. Besides, from a theoretical point of view, the qd theory supposes a perfectly sinusoidally distributed winding and excitation currents and so will overestimate the real torque in the machine.

4.8 Overview of recent studies

In previous sections, the most important parameters and their different calculation methods have been described. The implementation of these method is described using the EVT model in Chapter 5. In this section, an overview is given of different studies dealing with the FE modelling of an electrical device. These studies prove the importance of finite elements in the design of an electrical machine and are the foundations of the EVT model described in the next chapter.

Time-harmonic FEM model with core saturation: Belmans et al. (1993), Escarela-Perez et al. (2008), Ito et al. (1981), and Williamson et al. (1983, 1985a) present a numerical method for performance characteristic calculation of three phase squirrel cage induction motors, which is based on magnetic field analysis. The magnetic field is analysed over a radial cross-section of a

motor with a time-harmonic FE model taking into account core saturation. Transient analysis of induction motors using FEM are described in Martinez et al. (2012) and Williamson et al. (1990). The authors use a coupled circuit model in order to shorten computation time and include effect of end-windings, end-rings and skew in their model.

Combined magnetic field and electrical circuit equations: In his doctoral thesis, Arkkio et al., 1987 proposes a new method for the analysis of induction motors. The analysis is based on the combined solution of the magnetic field equations and the circuit equations of the windings. The equations are discretized by the finite element method. The author studies a two-dimensional model. Three-dimensional effects, such as rotor skew and and region effects, are taken into account within the two-dimensional formulation.

Equivalent model parameters: Dolinar et al. (1997), Faiz et al. (2002), Williamson et al. (1991), and Zhou et al. (1998) determine in their papers detailed equivalent model parameters of a cage induction machine using FEM. Core saturation is taken into account in the calculation of the flux distribution by a static non-linear vector potential solution. A linear time harmonic vector potential field solution is used for the inductances computations and the accuracy of the FE model is verified with measurements.

Single slot FE model: Andersen (2002) studies different rotor slot shapes of an induction motor using FEM. The author describes how finite element analysis of induction motors can be limited to one rotor slot pitch where conditions repeat with sufficient accuracy, and how this makes it possible to analyse fast and efficiently both no load, normal running and starting conditions. The use of a single slot model makes it possible to mesh the geometry very fine without increasing calculation time extensively. Especially for locked rotor condition, this is an interesting feature since a strong tangential magnetic field in the rotor close to the airgap requires a very fine element grid.

Three dimensional effects: Although a two-dimensional numerical analysis of an electrical machine provides an accurate solution of the electromagnetic field in the machine, a three-dimensional study is required to understand the actual phenomena such as end winding effects. Unfortunately, 3D models require a lot of computing resources, since the number of degrees of freedom is immense. Arkkio et al. (1987) state that end-winding inductances have only a small effect on no-load conditions, but in locked-rotor conditions 5 to 15 % of the coupled flux is caused by end-winding inductance. The easiest way to add the effect of end-region field into the voltage equations is to model the end-windings as resistances and constant inductances, whose values are determined by simple analytical methods or by measurements.

Williamson et al. (1985b) and Williamson et al. (1986) propose analytical models of respectively rotor-bar resistances and reactances, and end-ring resistances and reactances in order to include 3D effects. On the other hand, Silwal et al. (2012) and Yamazaki (1999) propose a coupled 2D-3D

model to solve the problem more accurately. Whereas a non-linear 2D model solves the problem using a coupled circuit approach, a 3D linear finite elements model calculates flux linkage between stator and rotor end-windings, which is added to the lumped parameter coupled circuit model.

Faulty induction motors: Many papers study faulty induction motors. The study of a faulty induction motor requires a very accurate model of the healthy one, which provide excellent references for this master paper. In Hanafy et al. (2014), Weili et al. (2007), and Xie (2012), broken bars in induction motors are studied. The induction motor is modelled using a time-stepping coupled finite-element approach. The effects of broken bars on the stator current, rotor bar currents distribution, the forces exerted on the rotor bars, the motor speed/torque and space harmonics are investigated. The papers conclude that broken bars introduce a pulsating torque. Moreover, tangential forces are not any more equally distributed over the rotor bars, whereas asymmetry in the radial forces will increase the mechanical stress on the rotor shaft. Sprooten et al. (2007) do not only investigate broken bars, but analyse also other kind of faults, i.e. stator short circuits. The study focusses on detecting and identifying faults in order to prevent damage to electrical devices.

Saturation and cross-saturation: Core saturation in electrical machines has been studied in many papers. The flux distribution along the airgap is the main design parameter of an electrical machine. An analytical generalized approach for various electrical machines types is proposed in Hsu et al. (2009). An equivalent magnetic circuit analysis (EMCA) is developed for an electrical device, based on the magnetic connection of simple geometric shapes (i.e. air-gap, stator and rotor tooth, and stator and rotor yoke). The following assumptions are made:

- The permeability of the iron core is variable;
- The flux flowing through one stator toot flows through the airgap uniformly within a slot pitch;
- The rotor is treated slotless;
- All the flux is strictly constrained in the magnetic circuit.

The advantage over EMCA over FEA is its computation time to optimize the design of an electrical device. If the design parameters are changed using FEA, the model has to be reconstructed, which is extremely time consuming.

Ide et al., 1999; Jianhui et al., 2003; Shima et al., 2002 study cross-saturation of electrical machines. The direct-axis and quadrature-axis inductances of a turbo electrical motor are usually considered as equal in an electrical device. But in fact, both the d-axis and q-axis inductances vary with the load condition because of magnetic circuit saturation. Analytical models are presented and equivalent model parameters are fixed using a numerical analysis of the electrical machine.

Chapter 5

EVT finite element model

Finite element simulations offer unique opportunities to understand the EVT machine-behaviour, and to perform both a geometrical optimization and an operational analysis. This chapter deals with the general description of the EVT's FE model according to a coupled circuit approach (section 4.4). The implementation of the model into different simulations cases is treated in the subsequent chapters.

Firstly, this chapter describes a geometric representation of the EVT system and its COMSOL model. Secondly, all model definitions and assumptions are included, using one specific geometry and operating point. Subsequently, a field oriented torque control (FOC) algorithm on both a linear and non-linear EVT model is presented. And finally, an iterative procedure is proposed in order to perform the FOC using the FE model in COMSOL.

5.1 Geometry

In this section, a general description of the geometry of the EVT is given. FE simulations of electrical machines require several hypotheses in order to reduce the model complexity and therefore computational time. As already mentioned, the machine is considered as a 2D entity in this paper. This assumption is only acceptable if it is supposed that:

- Both stator, interrotor and rotor conductors are not skewed;
- The axial length is sufficient to consider that end-region effect do not significantly contribute to the behaviour of the machine.

Moreover, in this work only a static analysis is performed, resulting in some additional assumptions:

- Skin effects are neglected;
- Eddy currents are neglected;
- Ventilation and mechanical losses are not considered.

The stator yoke geometry is based on a 4 pole 9 kW induction motor. The complete machine geometry is included in the FE model. As explained in section 4.8, it is possible to reduce the size of the problem by introducing symmetry. But, as this work only studies stationary field solutions, it is believed that a size reduction is not necessary.

The EVT geometry changes during this master thesis. Therefore, only symbolic dimensions are used. For specific dimensions, the reader is referred to the corresponding simulation models in Chapters 6 and 8. Fig. 5.1 presents an extruded view of the machine under study. The iron cores are modelled using the Soft Iron (without losses) material of the COMSOL library. Due to the presence of isolated iron sheets in both stator, interrotor and rotor cores, the magnetic hysteresis effect is not modelled here. However, flux saturation is taken into account, since it influences the currents in the machine and, thus, the resistive losses. The saturation characteristic of Soft Iron is presented in Fig. 5.2.

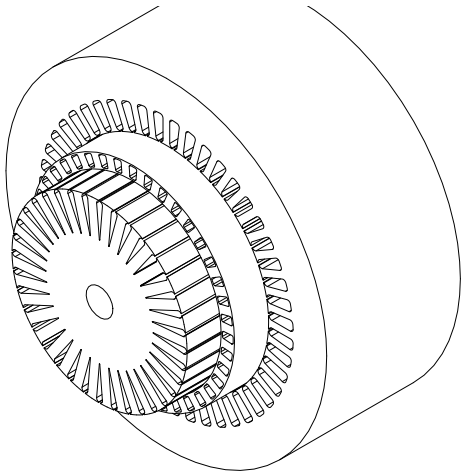

Figure 5.1: EVT: extruded view

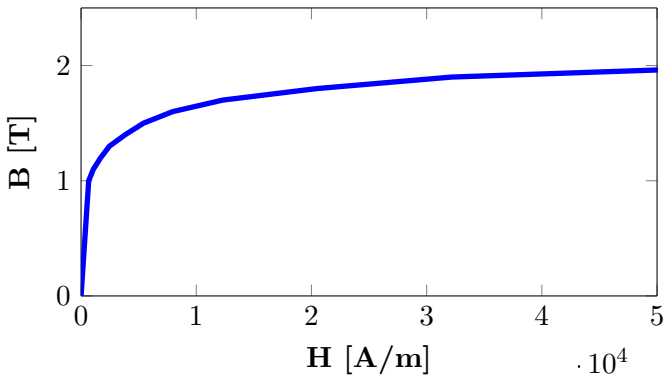

Figure 5.2: BH characteristic Soft Iron (without losses)

Fig. 5.3 shows a technical drawing of the iron core of the machine. In Table 5.1 the principal machine parameters are listed. As this paper focusses on a feasibility study of the EVT for off-highway applications, the main geometrical variables for which the machine is optimized include

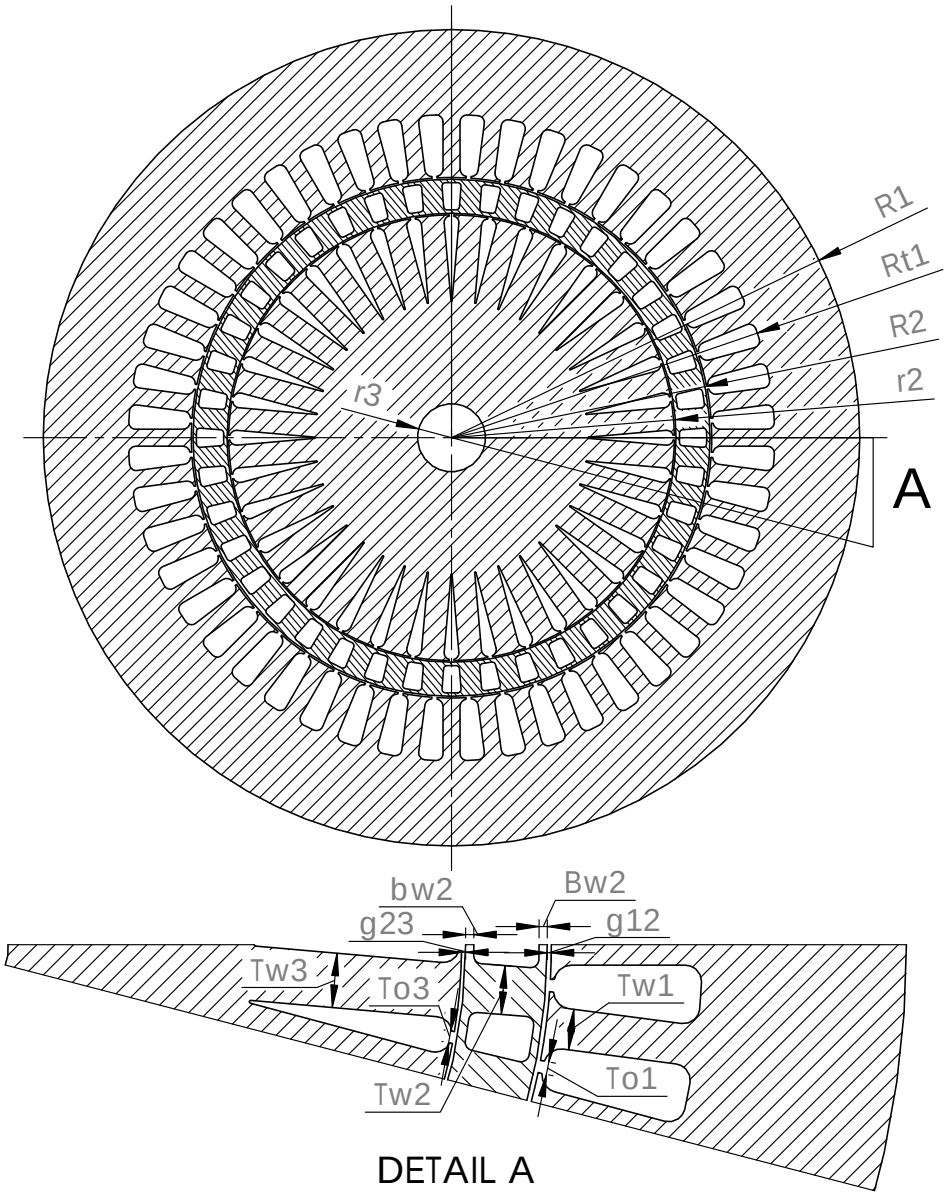

Figure 5.3: EVT: principal dimensions

the interrotor inner and outer radius (r_2 and R_2 respectively). All other dimensions are linked to this two principle variables. The airgap widths stator-interrotor (g_{12}) and interrotor-rotor (g_{23}) are fixed to 0.5 mm, which is a typical value for induction machines of the same size. The stator tooth width is 5 mm, similar to the reference stator core. Since the main flux linkage passes through the three parts, the total tooth surface for stator, interrotor and rotor should be equal. Consequently, the interrotor and rotor tooth wide are:

$$Tw_2 = \frac{N_1}{N_2} Tw_1 \tag{5.1a}$$

$$Tw_3 = \frac{N_1}{N_3} Tw_1 \tag{5.1b}$$

The slot opening of the wound stator and wound rotor is fixed to 1.5 mm in order to push the wires into the slots. Additionally, all slot corners are rounded to limit local saturation effects. The stator yoke hight is set to 25 mm, which makes the stator tooth base radius (Rt_1) 95 mm. Due to geometric constraints, the rotor tooth base radius (Rt_3) is minimum 40 mm, which makes the rotor yoke hight 30 mm. As the interrotor is of the squirrel cage type, the interrotor slots are completely enclosed

	Stator	Interrotor	Rotor
number of slots N_i	48	40	36
outer radius R_i [mm]	120	R_2	$r_2 - g_{23}$
inner radius r_i [mm]	$R_2 + g_{12}$	r_2	10
teeth radius Rt_i	95	-	40
Tooth thickness Tw_i [mm]	5	$\frac{N_1}{N_2} Tw_1$	$\frac{N_1}{N_3} Tw_1$
Tooth opening width To_i [mm]	1.5	-	1.5

Table 5.1: EVT: geometric parameters

by its iron core. The thickness of the iron bridges (bw_2 and Bw_2) is a very important geometrical parameter, since it strongly influences magnetic leakage in the machine. If the bridges are to wide, they are not saturated enough and an important part of the flux leaks through it; if they are too small, there may be mechanical strength problems. In this paper, the thickness is estimated to be 1 mm.

5.2 Mesh

The mesh is provided by the COMSOL mesh generator. In Fig. 5.4 a typical mesh is presented. A simple triangle mesh using the Delaunay algorithm[1] is executed. The mesh presented on the figure contains 1240 vertexes and 88350 mesh elements. These are typical values found in all performed simulations.

Practice has shown that there should be a detailed finite element mesh in the airgap regions in order to get accurate results (i.e. for torque calculations). Therefore, the airgap regions are meshed

[1] for more information: `http://en.wikipedia.org/wiki/Delaunay_triangulation`

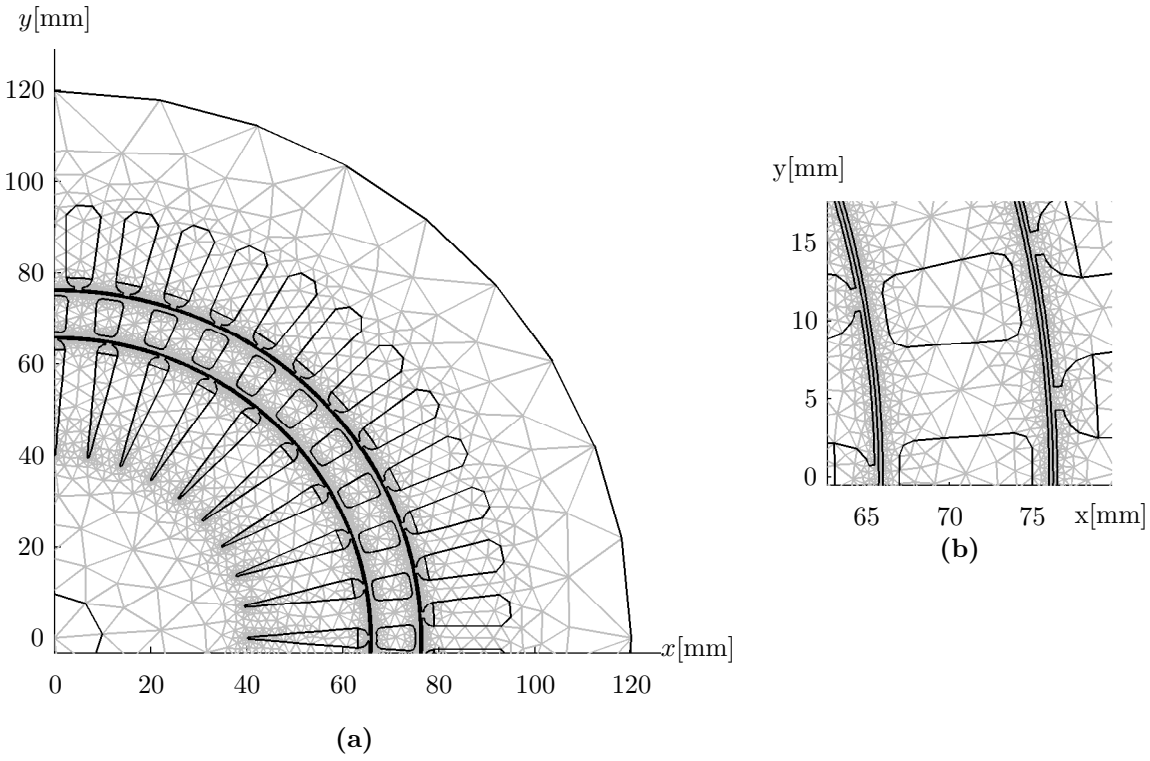

Figure 5.4: EVT: mesh

separately using finer conditions. The maximum mesh size in the airgaps is chosen at 0.25 mm. Since the width of the airgaps is 0.5 mm, an airgap encloses at minimum two mesh elements (shown on Fig. 5.4b), which gives relatively accurate results.

Note that only the machine and its internal structure are studied. The air regions around the stator core and within the rotor core are not modelled. Indeed, this regions have a very high reluctance and thus no flux is crossing them. The Dirichlet boundary condition, presented in section 4.2.3, is set on the mesh points at the outer-stator and inner-rotor radii.

5.3 Electrical machine parameters

In previous sections, the geometry and its mesh are described. This section deals with the electrical parameters of the device. These include wire connections, resistances, distribution factors, etc.

5.3.1 General

As described in section 5.1, the EVT design is based on a two pole pair 9 kW induction motor. Consequently, the number of pole pairs (N_p) of both stator, interrotor and rotor are chosen at two. The total number of stator winding per phase (w_1) yields 144 (based on the reference machine).

Since the stator and rotor are connected to the same DC bus bar, it is evident that the total number of rotor windings (w_2) equals 144 as well. The interrotor is of the squirrel-cage type. Since the interrotor contains 40 slots distributed over two pole pairs, it is regarded as a multi-phase winding with m_2 phases (each phase-winding is composed out of 2 slots):

$$m_2 = \frac{N_2}{2Np} = 10 \tag{5.2}$$

The cage winding can also be presented by its 3-phase equivalent winding. In this case, the number of slots per phase per pole pair (q_{2eq}) does not equal 1 any more. Instead, it is calculated by the following equations:

$$q_1 = \frac{N_1}{2Npm_1} = 4 \tag{5.3a}$$

$$q_2 = \frac{N_1}{2Npm_2} = 1 \tag{5.3b}$$

$$q_{2eq} = \frac{N_2}{2Npm_{2eq}} = \frac{10}{3} \tag{5.3c}$$

$$q_3 = \frac{N_3}{2Npm_3} = 4 \tag{5.3d}$$

The distribution factors or zone factors, which corresponds to a MMF decrease due to the distributed winding, are determined as:

$$\xi_i = \frac{\sin q_i \frac{\alpha_i}{2}}{q_i \sin \frac{\alpha_i}{2}} \tag{5.4}$$

With α_i the displacement between successive coil sides converted to electrical radians:

$$\alpha_i = \frac{2\pi}{N_i} Np \tag{5.5}$$

In order to have the same fundamental magnetic field amplitude of both the 10-phase interrotor winding and its 3-phase equivalent, the number of turns of the equivalent winding are (Melkebeek, 2013):

$$w_{2,eq} = \frac{10}{3} \frac{w_2 \xi_2}{\xi_{2,eq}} \tag{5.6}$$

5.3.2 Current transformations

Hereafter, the qd rotating reference frame is always used. An overview of the reference frames is given in Fig. 5.5. The phase currents I_a, I_b and I_c can be transformed into the $\alpha\beta$-frame using:

$$\begin{bmatrix} I_\alpha \\ I_\beta \end{bmatrix} = \frac{2}{3} \begin{bmatrix} 1 & \frac{-1}{2} & \frac{-1}{2} \\ 0 & \frac{\sqrt{3}}{2} & \frac{-\sqrt{3}}{2} \end{bmatrix} \begin{bmatrix} I_a \\ I_b \\ I_c \end{bmatrix} \tag{5.7}$$

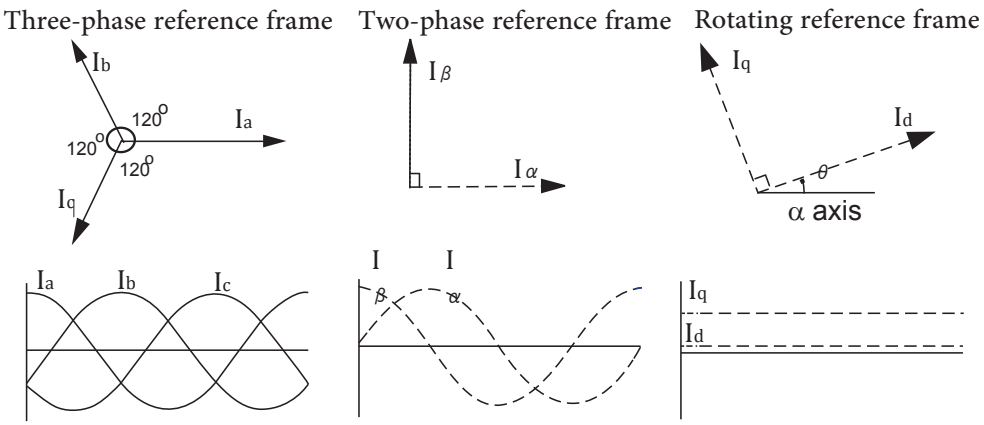

Figure 5.5: Clarke and Park transformations

Using a rotation the currents can be derived in a rotating qd-frame:

$$\begin{bmatrix} I_d \\ I_q \end{bmatrix} = \begin{bmatrix} \cos\theta & \sin\theta \\ -\sin\theta & \cos\theta \end{bmatrix} \begin{bmatrix} I_\alpha \\ I_\beta \end{bmatrix} \tag{5.8}$$

Because only stationary fields are studied, the latter can be avoided if the rotation angle θ is chosen to be zero. In this case, the α- and β-axes equal the q- and d-axes respectively.

Since the coupled circuit approach is applied, the q- and d-components of the currents (stator, interrotor and rotor) are input variables of the finite element analysis. Using the inverse of eq. (5.7) the corresponding stator and rotor phase values can be calculated.

However, the stator and rotor coils are modelled considering their conductors to be equally distributed in the slots. Each slot has thus an uniform current density in the COMSOL model. These densities are determined as:

$$J_{i,j} = \frac{I_{i,j}\, w_i}{N_p\, q_i\, Scu_i} \tag{5.9}$$

with $i \in [1,3]$, $j \in [u,v,w]$ and Scu_i the slot surface of the corresponding part. These slot surfaces can either be calculated analytically by geometric relations, or numerically by a surface integral in the COMSOL model. The analytical procedure has been chosen during this master's thesis, since this enables to calculated the slot surfaces before the construction of the geometry.

The interrotor is presented by its 10-phase equivalent winding. The currents in each bar can not be determined as easy as for the stator and rotor. Instead, the following procedure is pursued:

- Track the geometric location of the current vector:

$$\phi_2 = \arctan \frac{I_{2d}}{I_{2q}} \tag{5.10}$$

- Calculate the current density in all interrotor slots:

$$I_2 = \sqrt{I_{2q}^2 + I_{2d}^2} \tag{5.11a}$$

$$I_{2,k} = I_2 \cos\left(\phi_2 - (i-1)\frac{2\pi\, N_p}{N_2}\right) \tag{5.11b}$$

$$J_{2,k} = \frac{I_{2,k}}{Scu_2} \tag{5.11c}$$

with k the slot number of the interrotor (counting counter-clockwise, starting at the positive q-axis).

5.4 Example FE solution

Using the parameters described in previous paragraphs, it is possible to execute the finite element model in COMSOL. This section presents an example solution. Based on this results, the post-processing algorithms, presented in the following sections, are verified. The introduced results are evaluated for $r_2 = 70\,\text{mm}$ and $R_2 = 80\,\text{mm}$. The currents in both stator, interrotor and rotor are evaluated using the field oriented control method that is explained in section 5.7 and equal:

$$I_{1,qd} = (-0.403\,\text{A}; -8.067\,\text{A}) \tag{5.12a}$$

$$I_{2,qd} = (-158.73\,\text{A}; 0\,\text{A}) \tag{5.12b}$$

$$I_{3,qd} = (8.357\,\text{A}; -11.12\,\text{A}) \tag{5.12c}$$

The corresponding set values of interrotor and rotor torque are respectively $20\,\text{Nm}$ and $-20.5\,\text{Nm}$. Fig. 5.6 displays the magnetic field solution of the considered example. The figure shows only a quarter of the complete geometry as the other parts are symmetrically to the presented part. Both stator, interrotor and rotor are in a saturated condition, since the BH-characteristic of Fig. 5.2 saturates when the flux density is around and above $1.5\,\text{T}$. Furthermore, the interrotor bridges are strongly saturated, which is necessary for a good operation of the device.

5.4.1 Resistances

Because a two dimensional formulation is chosen, end-rings and end-windings effects affect both winding resistances and leakage inductances. In this paper, only end-region resistive effects are taken into account.

The phase resistances of both stator and rotor are calculated in the same manner. Since the stator and the rotor are wounded, the resistances are calculated using the simple theorem of Pouillet:

$$Res_i = \rho_{cu}\frac{l_{wire,i}}{A_{wire,i}} \tag{5.13}$$

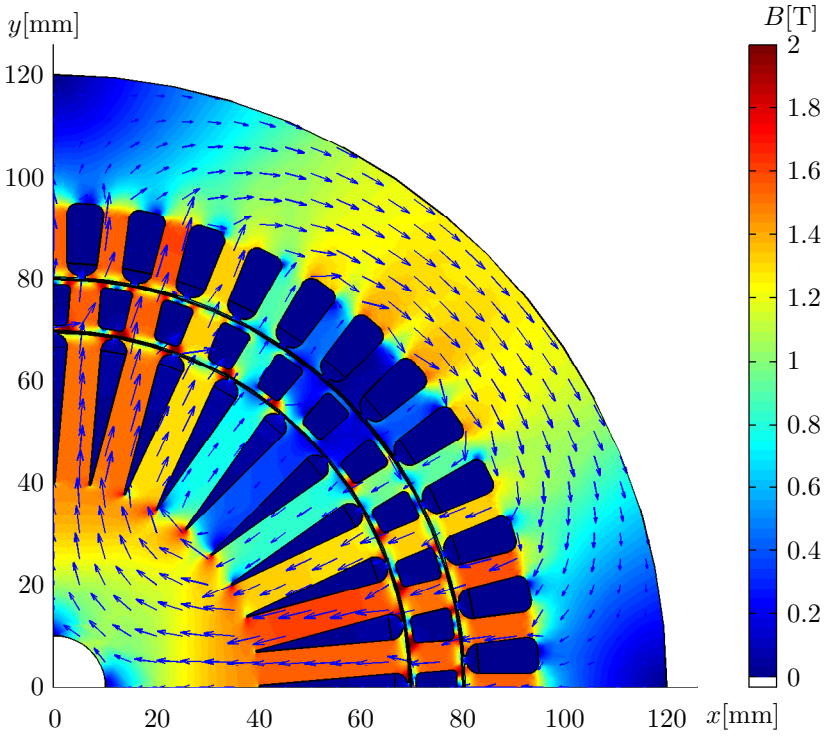

Figure 5.6: Example of magnetic field solution

with ρ_{cu} the specific resistance of the material (i.e. copper at 70 °C, $2 \times 10^{-8}\,\Omega$m), l_{wire} the total length of the phase wire and A_{wire} the cross section of the wire. The latter is calculated as:

$$A_{wire,i} = \frac{F_r\, Scu_i}{\frac{w_i}{N_p\, q_i}} \tag{5.14}$$

With F_r the fillrate of a slot. Typically, the fillrate of a winding yields 50 %. The remainder of the slot surface is occupied with wire isolation or with air, since the wires are round. Only when the wires are compressed into the slots, a higher fillrate can be achieved. The length of the wire is computed as:

$$l_{wire,i} = 2w_i \left(L_{ax} + \frac{\pi\tau_i}{2}\right) \tag{5.15}$$

τ_i is the pole pitch of the corresponding winding.

Again, the interrotor requires another approach. The resistance of one single bar is simply evaluated as:

$$Res_{bar} = \rho_{al} \frac{L_{ax}}{Scu_2} \tag{5.16}$$

In this case, ρ_{al} equals $3.36 \times 10^{-8}\,\Omega$m (i.e. aluminium at 70 °C). However, the interrotor currents which flow axially through the bars, complete their closed paths by passing circumferentially through the end-rings. The end-rings offer resistance to the passage of current, which is traditionally accounted for by making a modification to the bar resistance (Williamson et al., 1986). The bar

resistance is modified in such way that the joule losses in the real cage are equivalent to an equivalent cage with modified bar resistances and zero-resistance end-ring segments. By this technique, the effective bar resistance is given by (Vandevelde et al., 2014):

$$Res_{bar,equiv} = Res_{bar} + \frac{Res_{end}}{2N_2 \sin^2\left(\frac{\pi N_p}{N_2}\right)} \tag{5.17}$$

The end-ring resistance is estimated using a method described by Trickey (1936) and adopted in Sprooten et al. (2007):

$$Res_{end} = \frac{2\pi\rho D_r}{t(D_r - D_i)} K_{ring} \tag{5.18}$$

where K_{ring} is a correction factor for the wide of the end rings given by:

$$K_{ring} = N_p \left[\frac{1 + \left(\frac{D_i}{D_r}\right)^{2N_p}}{1 - \left(\frac{D_i}{D_r}\right)^{2N_p}}\right] \left(1 - \frac{D_i}{D_r}\right) \tag{5.19}$$

with:

- $D_i = 2r_2$: the end-ring internal diameter;
- D_r : the interrotor bar pitch circle diameter;
- $t = 10\,\text{mm}$: the thickness of the end-rings.

Practice shows that the bar resistance is doubled due to the end winding resistances (if $L_{ax} = 100\,\text{mm}$). It is evident that its influence decreases when the axial length of the machine is increased. The equivalent three phase resistance of the interrotor can now be calculated as (Vandevelde et al., 2014):

$$Res_2 = \frac{N_2}{3} Res_{bar,equiv} \tag{5.20}$$

5.5 Flux and inductances matrix

The previous section calculates the phase resistance without use of the field solution. As in this paper a non-linear machine model is studied, the inductances can not be calculated without the knowledge of the field distribution in the machine. Only when the field distribution is known the flux linkage to each winding can be calculated and the inductance matrix is derived.

5.5.1 Flux

The flux density is the rotation of the magnetic vector potential. The flux through a winding equals the surface integral over the winding. By means of Stokes' theorem, the flux can also be computed

as the line integral of the magnetic vector potential:

$$\Psi = \int_S \boldsymbol{B} \cdot \boldsymbol{n} \, \mathrm{d}S = \int_S \nabla \times \boldsymbol{A} \, \mathrm{d}S = \int_{\partial S} \boldsymbol{A} \, \mathrm{d}l \tag{5.21}$$

Consequently, in a two dimensional model, the flux coupled with stator and rotor winding is directly calculated if the magnetic field in the machine is solved.

$$\Psi_{i,j} = \frac{\int_{\Omega+_{i,j}} A_z \, \mathrm{d}\Omega - \int_{\Omega-_{i,j}} A_z \, \mathrm{d}\Omega}{q \, Scu_i} \frac{\xi_i \, w_i}{N_p} L_{ax} \tag{5.22}$$

with $\Omega+_{i,j}$ and $\Omega-_{i,j}$ respectively the positive and negative current slots of the i-th part and the j-th phase. The flux linkage for the interrotor is calculated in a different way. The three phase flux linkage is directly calculated if the average vector potential over $\frac{N_2}{2N_p m_2} (= \frac{10}{3})$ slots is evaluated:

$$\Psi_{2u} = \left[\left(\frac{1}{6} A_{39} + A_{40} + A_1 + A_2 + \frac{1}{6} A_3 \right) - \left(\frac{1}{6} A_9 + A_{10} + A_{11} + A_{12} + \frac{1}{6} A_{13} \right) \right] \frac{w_2 \, \xi_{2,eq}}{q_{2,eq}} L_{ax} \tag{5.23a}$$

$$\Psi_{2v} = \left[\left(\frac{3}{6} A_6 + A_6 + A_8 + \frac{5}{6} A_3 \right) - \left(\frac{3}{6} A_{16} + A_{17} + A_{18} + \frac{5}{6} A_{19} \right) \right] \frac{w_2 \, \xi_{2,eq}}{q_{2,eq}} L_{ax} \tag{5.23b}$$

$$\Psi_{2w} = \left[\left(\frac{5}{6} A_{13} + A_{14} + A_{15} + \frac{3}{6} A_{16} \right) - \left(\frac{5}{6} A_3 + A_4 + A_5 + \frac{3}{6} A_6 \right) \right] \frac{w_2 \, \xi_{2,eq}}{q_{2,eq}} L_{ax} \tag{5.23c}$$

With A_i the average vector potential over slot number i:

$$A_i = \frac{\int_{\Omega_i} A \, \mathrm{d}\Omega}{Scu_2} \tag{5.24}$$

Note that the flux calculation based on the magnetic field potential includes all harmonic components and assigns them to the first harmonic. Consequently, the flux is to high and thus a more detailed harmonic analysis is required in order to obtain a better estimate.

5.6 Torque calculation

Section 4.7 gives an overview of different torque calculation methods in literature. In this section, those methods are applied to the EVT.

5.6.1 Maxwell stress tensor

The Maxwell stress tensor is probably the easiest method to calculate torque in an electrical device. It only requires the magnetic field for its computations. COMSOL contains a built-in function which evaluates the Maxwell stress tensor in each element. The torque on each part can then be calculated as the integral of the tensor over the corresponding elements.

One can verify these results performing a manual calculation. In general, the electromagnetic torque is obtained as a surface integral:

$$\boldsymbol{T_e} = \oint_S \boldsymbol{r} \times \boldsymbol{\sigma}\, \mathrm{d}S \tag{5.25a}$$

$$= \oint_S \boldsymbol{r} \times \left\{ \frac{1}{\mu_0}(\boldsymbol{B}\cdot\boldsymbol{n})\boldsymbol{B} - \frac{1}{2\mu_0}\boldsymbol{B}^2\boldsymbol{n} \right\} \mathrm{d}S \tag{5.25b}$$

where $\boldsymbol{\sigma}$ is the Maxwell stress tensor.

When eq. (5.25) is applied to the electrical variable transmission, a closed integration surface in the airgaps must be chosen. In a two-dimensional model, the surface integral is reduced to a line integral. If a circle of radius r is taken as integration path, the torque is obtained from:

$$T_e = \frac{L_{ax}}{\mu_0} \int_0^{2\pi} r^2 B_r B_\phi \, \mathrm{d}\phi \tag{5.26}$$

B_r and B_ϕ are respectively the radial and tangential flux distribution along the airgaps. The torque on the separated parts can now be evaluated as:

$$T_1 = -T_{e,12} \tag{5.27a}$$

$$T_2 = T_{e,12} - T_{e,23} \tag{5.27b}$$

$$T_3 = T_{e,23} \tag{5.27c}$$

If the solutions were exact, the value of the torque calculated from eq. (5.26) would be independent of the radius r when r varies between the inner and outer radii of the airgaps. However, a finite element solution is always an approximation of reality and thus the torque is not independent of the integration path. Table 5.2 shows the torque variation along the inner airgap.

r_{23} [mm]	69.6	69.7	69.8	69.9
T_3 [Nm]	-21.11	-20.52	-20.71	-20.72

Table 5.2: Torque variation along the airgap

Section 4.7 explains that the cause of the variation lies in the discretization of the airgap. Fig. 5.7 displays a close-up of the magnetic field in the inner airgap. The flux density under the rotor teeth is radial. On the other hand, the flux between the teeth has a large tangential component. Since the stress tensor of eq. (5.26) includes a multiplication of the radial and axial components, spikes are generated in the elementary torque density in the airgap. Fig. 5.8 displays the torque density around the rotor. The figure confirms the predicted torque spikes along the airgap. In order to retrieve an accurate integrated torque value, each spike must contain at least several mesh point, which requires an accurate mesh triangulation in the airgap.

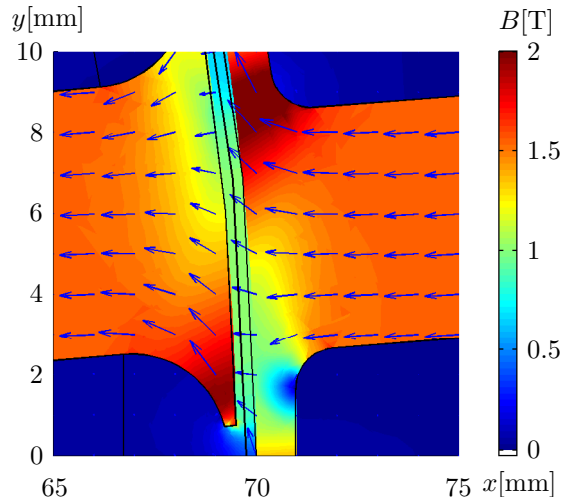

Figure 5.7: Close up of magnetic field solution along inner airgap

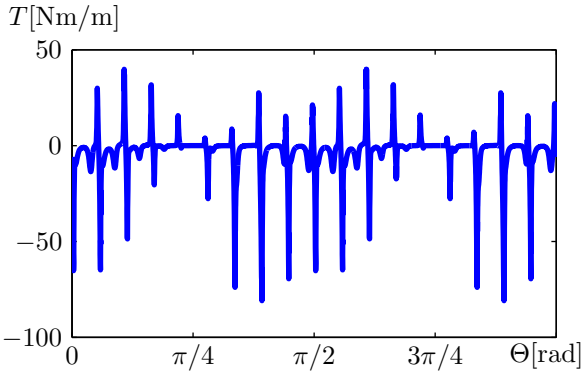

Figure 5.8: Torque density along inner airgap

5.6.2 Arkkio

The torque values in Table 5.2 can be improved by averaging them. Another method is proposed by Arkkio et al. (1987). The two-dimensional line integral of eq. (5.26) is replaced by a surface integral.

$$T_e\,(R_o - R_i) = \int_{R_i}^{R_o} T_e \,\mathrm{d}r \tag{5.28}$$

$$= \frac{L_{ax}}{\mu_0} \int_{R_i}^{R_o} \left\{ \int_0^{2\pi} r^2 B_r B_\phi \,\mathrm{d}\phi \right\} \tag{5.29}$$

$$= \frac{L_{ax}}{\mu_0} \int_{S_{ag}} r B_r B_\phi \,\mathrm{d}S \tag{5.30}$$

where r_o and r_i are the outer and inner radii of the airgap respectively and S_{ag} the cross sectional area of the airgap. The electromagnetic torque is now obtained by a surface integral over the airgap:

$$T_e = \frac{L_{ax}}{\mu_0 (R_o - R_i)} \int_{S_{airgap}} r B_r B_\phi \, \mathrm{d}S \tag{5.31}$$

5.6.3 Maxwell stress harmonic filter

A last method which is used to calculate the torque in the device is proposed by Popescu (2006) and already briefly explained in section 4.7.4: the Maxwell stress harmonic filter (HFT). The method includes a direct torque derivation of the flux density components from an analytical expression of the airgap magnetic vector potential. Two concentric circles of radii R_{gi} and R_{go} are defined inside the airgaps and used as non-homogeneous Dirichelet boundary conditions, with values determined by the magnetic vector potential solution. The circles are shown in Fig. 5.9 in the case of a synchronous motor. The magnetic vector potential enclosed between the circles R_{gi} and R_{go} can

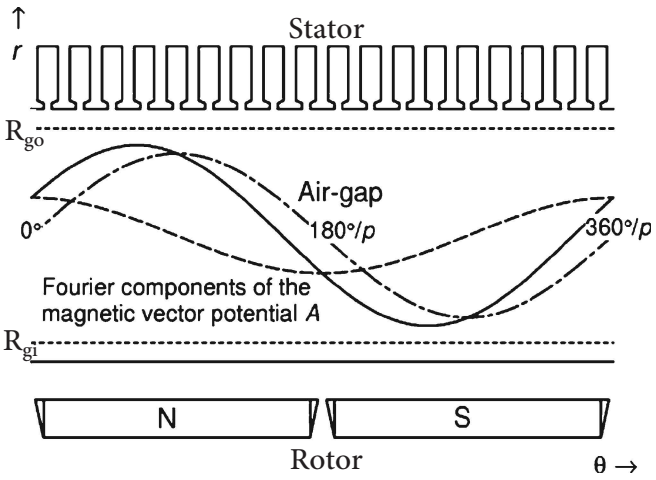

Source: Popescu (2006, page 2).

Figure 5.9: Maxwell HFT method for computing torque

analytically be described as (Popescu, 2006):

$$A(r,\theta) = \sum_{n=1}^{\infty} \left[\left(c_n r^n + d_n r^{-n} \right) \left(g_n \cos(n\theta) + h_n \sin(n\theta) \right) \right] \tag{5.32}$$

In this equation, four coefficients need to be identified. Therefore, the magnetic vector potential is recorded along two boundaries in the airgap by making use of the solution obtained by finite element analysis. The magnetic vector potential on those boundaries can be expressed as a Fourier

series:

$$A(R_{gi},\theta) = \sum_{n=1}^{\infty} \left[a_{n1}\cos(n\theta) + b_{n1}\sin(n\theta)\right] \tag{5.33a}$$

$$A(R_{go},\theta) = \sum_{n=1}^{\infty} \left[a_{n2}\cos(n\theta) + b_{n2}\sin(n\theta)\right] \tag{5.33b}$$

Writing the above equations in the form of eq. (5.32) the following coefficients are derived:

$$c_n g_n = \frac{1}{\delta_n}\left[a_{n1}\left(\frac{R_1}{R_2}\right)^n - a_{n2}\right] \tag{5.34a}$$

$$c_n h_n = \frac{1}{\delta_n}\left[b_{n1}\left(\frac{R_1}{R_2}\right)^n - b_{n2}\right] \tag{5.34b}$$

$$d_n g_n = \frac{1}{\delta_n}\left[a_{n2} - a_{n1}\left(\frac{R_2}{R_1}\right)^n\right] \tag{5.34c}$$

$$d_n h_n = \frac{1}{\delta_n}\left[b_{n2} - b_{n1}\left(\frac{R_2}{R_1}\right)^n\right] \tag{5.34d}$$

where:

$$\delta_n = \left(\frac{R_{gi}}{R_{go}}\right)^n - \left(\frac{R_{go}}{R_{gi}}\right)^n \tag{5.35}$$

The magnetic flux density components are calculated by derivation of the magnetic vector potential (eq. (5.32)):

$$B_r = \frac{\partial A}{r\,\partial\theta}; \quad B_\theta = -\frac{\partial A}{\partial r}; \tag{5.36}$$

Substitution of these equations into eq. (5.26) returns into a hybrid analytical-numerical computational formula for the electromagnetic torque (Popescu, 2006, eq. 14):

$$T_e = N_p \frac{2\pi\, L_{ax}}{\mu_0} \sum_{n=0}^{\infty} \frac{n^2\left(a_{n2}b_{n1} - a_{n1}b_{n2}\right)}{\delta_n} \tag{5.37}$$

Table 5.3 gives an overview of the different methods presented above. All values are relatively equal. Based on this analysis, one can conclude that the constructed model works properly.

Method	COMSOL	Maxw (avg.)	Arkkio	HFT	Flux
T_2 [Nm]	20.12	19.83	19.73	19.76	19.99
T_3 [Nm]	-20.71	-20.76	-20.71	-20.73	-20.70

Table 5.3: Comparison of torque calculation methods

5.7 Torque control on a double rotor induction machine

In previous sections, a straight torque calculation is performed, i.c. when the currents are inserted in the model, the torque can be derived. In order to control the torque, the inverse is required. This means that when the torque is known, the model must be able to derive the corresponding currents in the machine. Section 5.5.1 notes that the parameters of the machine model strongly depend on the operation point, since a non-linear model is studied. Consequently, a simple inversion of the straight procedure can not be used for torque control. This section presents a torque control model for the double rotor induction machine. Firstly, a simplified linear model by Druant et al., 2014 is explained. Furthermore, some adaptation are presented in order to include non-linear effects and an iterative procedure is discussed in order to include the model into FE.

5.7.1 System model of the linear machine

Druant et al. (2014) consider the EVT in its qd-reference frame rotating with the synchronous magnetic field. In this instantaneously synchronous reference frame, all currents are DC-currents. The relations between thermal voltages and winding currents yield:

$$\begin{cases} V_{1q} = R_1 I_{1q} + p\Psi_{1q} - \omega\Psi_{1d} \\ V_{1d} = R_1 I_{1d} + p\Psi_{1d} + \omega\Psi_{1q} \end{cases} \tag{5.38a}$$

$$\begin{cases} V_{2q} = 0 = R_2 I_{2q} + p\Psi_{2q} - s_2\omega\Psi_{2d} \\ V_{2d} = 0 = R_2 I_{2d} + p\Psi_{2d} + s_2\omega\Psi_{2q} \end{cases} \tag{5.38b}$$

$$\begin{cases} V_{3q} = R_3 I_{1q} + p\Psi_{3q} - s_3\omega\Psi_{3d} \\ V_{3d} = R_3 I_{1d} + p\Psi_{3d} + s_3\omega\Psi_{3q} \end{cases} \tag{5.38c}$$

ω is the pulsation of the magnetic field in a two-pole representation. For each rotor, the slip can be defined as the relative difference between the rotational speed and the speed of the magnetic field:

$$s_2 = \frac{\omega - \omega_2}{\omega} \tag{5.39a}$$

$$s_3 = \frac{\omega - \omega_3}{\omega} \tag{5.39b}$$

with ω_2 and ω_3 the interrotor and rotor pulsation respectively. As the EVT is a turbo-machine, the relationships between the magnetic flux and winding currents for both q- and d-axes are equal. Moreover, because slot effects are neglected, the inductance matrix representing the magnetic behaviour of the machine is restricted to a 3×3-matrix:

$$\begin{bmatrix} \boldsymbol{\Psi_1} \\ \boldsymbol{\Psi_2} \\ \boldsymbol{\Psi_3} \end{bmatrix} = \begin{bmatrix} L_{11} & L_{12} & L_{13} \\ L_{12} & L_{22} & L_{23} \\ L_{13} & L_{23} & L_{33} \end{bmatrix} \begin{bmatrix} \boldsymbol{I_1} \\ \boldsymbol{I_2} \\ \boldsymbol{I_3} \end{bmatrix} \tag{5.40}$$

The flux vectors linked to the stator, interrotor and rotor respectively, considered in a synchronous reference frame, are defined as:

$$\begin{cases} \boldsymbol{\Psi_i} = \Psi_{iq} + j\,\Psi_{id} \\ \boldsymbol{I_i} = I_{iq} + j\,I_{id} \end{cases} \tag{5.41}$$

with $i \in \{1, 2, 3\}$. Similar to single rotor electrical machines, the torque on the rotating parts is expressed as following:

$$\begin{cases} T_2 = \frac{3}{2} N_p \left(I_{2q}\Psi_{2d} - I_{2d}\Psi_{2q}\right) \\ T_3 = \frac{3}{2} N_p \left(I_{3q}\Psi_{3d} - I_{3d}\Psi_{3q}\right) \end{cases} \tag{5.42}$$

Since the magnitude of the electromagnetic torque depends on both the magnitude of the magnetic flux and winding currents, but also on their relative angle, the torque can be controlled using field oriented control (FOC).

Similar to torque control in induction machines, the torque-current ratio on the interrotor of the EVT can be maximized when the relative angle between the vector current and the vector flux is 90°. The relative phase of the *qd*-reference frame for FOC can be chosen freely. Druant et al. (2015) choose the interrotor flux Ψ_2 along the negative d-axis, which is also a typical convention in FOC for asynchronous machines.

$$\Psi_{2q} \equiv 0 \tag{5.43}$$

From eq. (5.42), the torque on the interrotor is simplified as:

$$T_2 = \frac{3}{2} N_p\, \Psi_{2d} I_{2q} \tag{5.44}$$

The torque in the interrotor is thus the multiplication of two orthogonal components Ψ_{2d} and I_{2q}. Combining eqs. (5.40) and (5.43) an expression for the q-axis current in the interrotor is obtained:

$$I_{2q} = \frac{-1}{L_{22}} \left(L_{12} I_{1q} + L_{23} I_{3q}\right) \tag{5.45}$$

In order to control the interrotor torque, the flux is required. The combination eqs. (5.38b) and (5.44) delivers following constraint:

$$p\Psi_{2d} = -R_2 I_{2d} \tag{5.46}$$

meaning that the resistive voltage drop in the interrotor equals the induced interrotor voltage. This is the result of the fact that the interrotor is short-circuited. Using this and the definition of the interrotor flux (eq. (5.40)) yields:

$$\Psi_{2d} = \frac{L_{12} I_{1d} + L_{23} I_{3d}}{1 + p\frac{L_{22}}{R_2}} \tag{5.47}$$

Note that the flux can not be changed instantaneously. Therefore, the flux is kept constant in both regime operation as transient operation. Moreover, from eqs. (5.45) and (5.47), both the interrotor current and the interrotor flux can be written in function of stator and rotor quantities, and thus

the interrotor torque in eq. (5.44) can also be written in function of stator and rotor quantities.

5.7.2 Field oriented control of the linear machine

With the expressions above, it is possible to derive a control scheme which controls the torque on both rotors. To this end, the controller needs to select at every instant a set of currents satisfying eqs. (5.40) and (5.42). Since there are only two constraints to be fulfilled (T_2,T_3) and four unknowns (I_{1q},I_{1d},I_{2q},I_{2d}), two degrees of freedom remain. An additional constraint is formed when the interrotor flux Ψ_{2d} is controlled. According to Druant et al. (2015), there are multiple reasons to monitor the interrotor flux along with the current:

- The flux can not be changed instantaneously, which is a fundamental law of electromagnetism (see eq. (5.47)). In order to have a fast transient torque response, the flux is held at a certain value, whereas the currents are instantaneously changed.
- The inductance parameters used in eq. (5.40) are not only constant parameters in a linear model, but also in a non-linear model, the parameters are constant in a certain operating point. Because the flux determines the degree of saturation, the magnetization state can not deviate too far from this point for correct torque control.
- Controlling the flux limits the currents for a certain torque. From eq. (5.44) it is seen that a higher flux decreases the torque-forming current component I_{2q}. On the other hand, the flux-forming component I_{2d} increases. An appropriate balance between the torque-forming and flux-forming current components in the interrotor can certainly reduce the joule losses in the device.
- The voltage applied to the terminals of the machine is limited by the DC-bus voltage. As the magnitude of the flux determines the back-emf of the machine, the flux can not be to high.

Summarized, the field orientation controller needs to select stator and rotor currents according to the following set of equations:

$$\begin{cases} \tau_2 = Ł_{12} I_{1q} + L_{23} I_{3q} \\ \tau_3 = Ł_{31} I_{1q} I_{3q} + I_{3d} \left(L_{13} I_{1q} + L_{23} I_{2q} \right) \\ \Psi_{2d} = Ł_{12} I_{1d} + L_{23} I_{3d} \end{cases} \tag{5.48}$$

with $\tau_2 = \frac{-2L_{22}}{3N_p \Psi_{2d}} T_2$ and $\tau_3 = \frac{2}{3N_p} T_3$ known. I_{2q} is calculated in eq. (5.45), while I_{2d} is zero in steady state, as explained in the previous section. Reorganization of these equations leads to an equivalent set of equations:

$$\begin{cases} I_{3q} = \frac{\tau_2}{L_{23}} - \frac{L_{12}}{L_{23}} I_{1q} \\ I_{3d} = \frac{\Psi_{2d}}{L_{23}} - \frac{L_{12}}{L_{23}} I_{1d} \\ I_{1q} - a_2 I_{Id} = a_1 \end{cases} \tag{5.49a}$$

with

$$\begin{cases} a_1 = -\frac{L_{23}\tau_3 + L_{23}\Psi_{2d}I_{2q}}{L_{13}\Psi_{2d}} \\ a_2 = \frac{L_{13}\tau_2 + L_{12}L_{23}I_{2q}}{L_{13}\Psi_{2d}} \end{cases} \tag{5.49b}$$

Eq. (5.49) shows that there is still one degree of freedom left. An additional equation is made if the joule losses are minimized. The joules losses are defined by:

$$P_j = \frac{3}{2}\left[R_1\left(I_{1q}^2 + I_{1d}^2\right) + R_2\left(I_{2q}^2 + I_{2d}^2\right) + R_3\left(I_{3q}^2 + I_{3d}^2\right)\right] \tag{5.50}$$

Since the interrotor current is not a variable (fixed by interrotor flux and torque, eq. (5.44)), the cost function equals (including eq. (5.49a)):

$$\text{minimize } R_1\left(I_{1q}^2 + I_{1d}^2\right) + R_3\left(\left(\frac{\tau_2}{L_{23}}\frac{L_{12}}{L_{23}}I_{1q}\right)^2 + \left(\frac{\Psi_{2d}}{L_{23}}\frac{L_{12}}{L_{23}}I_{1d}\right)^2\right) \tag{5.51a}$$

subjected to the following constraint:

$$I_{1q} - a_2 I_{Id} = a_1 \tag{5.51b}$$

The optimization problem defined by eq. (5.51) is solved using Lagrange multipliers. The solution is given by Druant et al. (2015):

$$\begin{cases} I_{3q} = \frac{\tau_2}{L_{23}} - \frac{L_{12}}{L_{23}}I_{1q} \\ I_{3d} = \frac{\Psi_{2d}}{L_{23}} - \frac{L_{12}}{L_{23}}I_{1d} \\ I_{1q} = \frac{1}{h_1}(\lambda + h_2) \\ I_{1d} = \frac{1}{h_1}(-a_2\lambda + h_3) \end{cases} \tag{5.52a}$$

with

$$\begin{cases} h_1 = 2R_1 + 2\left\{\frac{L_{12}}{L_{23}}\right\}^2 R_3 \\ h_2 = 2\frac{L_{12}}{L_{23}^2}R_3\tau_2 \\ h_3 = 2\frac{\Psi_{2d}L_{12}}{L_{23}^2}R_3 \\ \lambda = \frac{a_1h_1 - h_2 + a_2h_3}{1+a_2^2} \end{cases} \tag{5.52b}$$

These equations fix all currents in both stator and rotor in the *qd*-reference frame. In order the calculate the corresponding phase currents, the orientation of the qd-frame needs to be known. To do so, Druant et al. (2015) employ an indirect field oriented control scheme. The so-called slip equation is used to synchronize the currents with the field. Using eq. (5.38b), the pulsation of the interrotor field with respect to the interrotor (slip-pulsation) is calculated as:

$$s_2\omega = \frac{R_2 I_{2q}}{\Psi_{2d}} \tag{5.53}$$

The choice of the interrotor flux and the DC-bus voltage is the subject of Druant et al. (2015). A linear EVT machine model shows that, when the maximum tooth flux density is limited to 1.6 T, the d-axis interrotor flux is restricted to 0.042 Wb. Hereafter, this value is used in all simulations.

$$\Psi_{2d,set} = 0.042\,\mathrm{Wb} \tag{5.54}$$

5.7.3 Field oriented control including a non-linear machine model

In the previous section, a linear model is studied. In this paragraph, core saturation is included. The EVT is represented by its linearised model, i.e. inductances are calculated as in a linear model (the quotient of flux and current) but the inductance matrix is dependent on the saturation state of the machine.

As the FE model is a close approximation of the reality, it also includes slot and cross-saturation effects. In other words, in the linearised model, the q- and d-axis fluxes are formed by the complete inductance matrix instead of the reduced form from eq. (5.40).

$$\boldsymbol{\Psi_{123qd}} = \mathsf{L}_{\mathsf{ind}}\ \boldsymbol{I_{123qd}} \tag{5.55}$$

with

$$\boldsymbol{\Psi_{123qd}} = \begin{bmatrix} \Psi_{1q} & \Psi_{2q} & \Psi_{3q} & \Psi_{1d} & \Psi_{2d} & \Psi_{3d} \end{bmatrix}^T \tag{5.56a}$$

$$\boldsymbol{I_{123qd}} = \begin{bmatrix} I_{1q} & I_{2q} & I_{3q} & I_{1d} & I_{2d} & I_{3d} \end{bmatrix}^T \tag{5.56b}$$

$$\mathsf{L}_{\mathsf{ind}} = \begin{bmatrix} L_{11qq} & L_{12qq} & L_{13qq} & L_{11qd} & L_{12qd} & L_{13qd} \\ L_{21qq} & L_{22qq} & L_{23qq} & L_{21qd} & L_{22qd} & L_{23qd} \\ L_{31qq} & L_{32qq} & L_{33qq} & L_{31qd} & L_{32qd} & L_{33qd} \\ L_{11dq} & L_{12dq} & L_{13dq} & L_{11dd} & L_{12dd} & L_{13dd} \\ L_{21dq} & L_{22dq} & L_{23dq} & L_{21dd} & L_{22dd} & L_{23dd} \\ L_{31dq} & L_{32dq} & L_{33dq} & L_{31dd} & L_{32dd} & L_{33dd} \end{bmatrix} \tag{5.56c}$$

The matrix $\mathsf{L}_{\mathsf{ind}}$ can be composed out of four 3×3-matrices.

$$\mathsf{L}_{\mathsf{ind}} = \begin{bmatrix} \mathsf{L}_{\mathsf{qq}} & \mathsf{L}_{\mathsf{qd}} \\ \mathsf{L}_{\mathsf{dq}} & \mathsf{L}_{\mathsf{dd}} \end{bmatrix} \tag{5.57}$$

Due to reciprocity of fluxes and currents, the matrices L_{qq} and L_{dd} are symmetrical, and L_{qd} equals ${\mathsf{L}_{\mathsf{dq}}}^T$. L_{qq} and L_{dd} are the inductance matrices in the q- and d-axis respectively. In the linear model, these matrices are equal since the EVT is a turbo machine. Due to saturation, the matrices slightly differ as the saturation state of the machine depends on both q- and d- axis currents. Consequently, a q-axis current influences the flux through the d-axis and vice versa. This phenomenon is called cross-saturation or inter-saturation.

If slot effects are neglected, as in section 5.7.2, the matrices $\mathsf{L_{qd}}$ and $\mathsf{L_{dq}}$ are zero matrices and the q- and d-axes are decoupled (i.e. a d-axis current does not cause a q-axis flux and vice versa). Practice shows that these matrices have non-zero values. Although its influence is small in comparison to the cross-saturation effect, it is taken into account in the proposed linearised model.

In order to control torque using the linearised model, the controller still needs to select stator and rotor currents subjected to eqs. (5.42) and (5.43). In fact, the optimization problem defined by eq. (5.51) is transformed into a multi-constraint problem:

$$\text{minimize } R_1\left(I_{1q}^2 + I_{1d}^2\right) + R_3\left(I_{3q}^2 + I_{3d}^2\right) \tag{5.58a}$$

subjected to following constraints:

$$\Psi_{2q} = 0 \tag{5.58b}$$

$$\Psi_{2d} = \Psi_{2d,set} \tag{5.58c}$$

$$I_{3q}\Psi_{3d} - I_{3d}\Psi_{3q} = \tau_3 \tag{5.58d}$$

According to eq. (5.58), both q-axis and d-axis flux are controlled, which correspond to eqs. (5.43) and (5.54). Because the set value of the interrotor torque in an input parameter, the currents in the interrotor is fixed by eq. (5.44). The resulting Lagrangian function yields:

$$L = R_1\left(I_{1q}^2 + I_{1d}^2\right) + R_3\left(I_{3q}^2 + I_{3d}^2\right) + \lambda\left(\Psi_{2q}\right) + \mu\left(\Psi_{2d} - \Psi_{2d,set}\right) + \nu\left(I_{3q}\Psi_{3d} - I_{3d}\Psi_{3q} - \tau_3\right) \tag{5.59}$$

with variables $I_{1q}, I_{1d}, I_{3q}, I_{3d}$ and Lagrange multipliers λ, μ, ν.

An explicit solution of the problem is not possible any more, since the problem in highly non-linear. Instead, a numerical solution can be provided. According to the theorem of Lagrange, the derivatives with respect to each variable of eq. (5.59) and the Lagrange multipliers are taken, resulting in the following set of equations:

$$0 = 2R_1 I_{1d} + \lambda L_{21dd} + \mu L_{21qd} + \nu\left(I_{3q}L_{31dd} - I_{3d}L_{31qd}\right) \tag{5.60a}$$

$$0 = 2R_1 I_{1q} + \lambda L_{21dq} + \mu L_{21qq} + \nu\left(I_{3q}L_{31dq} - I_{3d}L_{31qq}\right) \tag{5.60b}$$

$$\begin{aligned} 0 = {} & 2R_3 I_{3d} + \lambda L_{23dd} + \mu L_{23qd} + \nu\left(I_{3q}L_{33dd} - I_{3d}L_{33qd}\right. \\ & \left. - \left(L_{31qq}I_{1q} + L_{32qq}I_{2q} + L_{33qq}I_{3q} + L_{31qd}I_{1d} + L_{32qd}I_{2d} + L_{33qd}I_{3d}\right)\right) \end{aligned} \tag{5.60c}$$

$$\begin{aligned} 0 = {} & 2R_3 I_{3q} + \lambda L_{23dq} + \mu L_{23qq} + \nu\left(I_{3q}L_{33dq} - I_{3d}L_{33qq}\right. \\ & \left. + \left(L_{31dq}I_{1q} + L_{32dq}I_{2q} + L_{33dq}I_{3q} + L_{31dd}I_{1d} + L_{32dd}I_{2d} + L_{33dd}I_{3d}\right)\right) \end{aligned} \tag{5.60d}$$

$$0 = L_{21qq}I_{1q} + L_{22qq}I_{2q} + L_{23qq}I_{3q} + L_{21qd}I_{1d} + L_{22qd}I_{2d} + L_{23qd}I_{3d} \tag{5.60e}$$

$$\Psi_{2d,set} = L_{21dq}I_{1q} + L_{22dq}I_{2q} + L_{23dq}I_{3q} + L_{21dd}I_{1d} + L_{22dd}I_{2d} + L_{23dd}I_{3d} \tag{5.60f}$$

$$\begin{aligned} \tau_3 = {} & I_{3q}\left(L_{31dq}I_{1q} + L_{32dq}I_{2q} + L_{33dq}I_{3q} + L_{31dd}I_{1d} + L_{32dd}I_{2d} + L_{33dd}I_{3d}\right) \\ & - I_{3d}\left(L_{31qq}I_{1q} + L_{32qq}I_{2q} + L_{33qq}I_{3q} + L_{31qd}I_{1d} + L_{32qd}I_{2d} + L_{33qd}I_{3d}\right) \end{aligned} \tag{5.60g}$$

The first four equations of eq. (5.60) are the derivatives with respect to I_{1q}, I_{1d}, I_{3q} and I_{3d} respectively. The last three equations represent the constraints of eq. (5.58). The set of equations is solved using a numerical solver in MATLAB (Trust-Region Dogleg Method[2]) for variables $I_{1q}, I_{1d}, I_{3q}, I_{3d}$ and Lagrange multipliers λ, μ, ν. The initial values of the stator and rotor currents are based on the linear method described in section 5.7.2. Because q-axis fluxes are mainly caused by q-axis currents, initial q-axis currents (I_{1q} and I_{3q}) are calculated performing the linear FOC using $\mathsf{L_{qq}}$. For similar reasons, the initial d-axis currents are evaluated using inductance matrix $\mathsf{L_{dd}}$ in the linear FOC algorithm.

Practice shows that the proposed method gives fast and accurate results for both torque and flux equations.

5.7.4 Iterative field oriented torque control using a non-linear model

In the section above, a FOC model is built in order to control the torque in the machine precisely. The algorithm can only be proceeded if the complete inductance matrix from eq. (5.56c) is known beforehand. Since this matrix is strongly dependent on the saturation state of the material and thus of the operating point, it is not known in advance. In order to perform the FOC method using the FE model, an iterative procedure is constructed, as shown in Fig. 5.10. Firstly, the geometric model is build, as explained in sections 5.1 and 5.2. In parallel, the currents in the machine are calculated performing the non-linear torque control based on an estimated initial inductances. Subsequently, the finite element model is solved using COMSOL and flux, torque and updated inductances are calculated respectively. If the torque error is less than 2 % of its set-point, the method is stopped. If not, the model is updated using the new inductance matrix and another iteration is executed. The set-point torque of the example in section 5.4 equals 20 Nm and -20.5 Nm for interrotor and rotor respectively, whereas the resulting torque calculated by the finite element analysis yields 19.98 Nm and -20.70 Nm. It is clear that the proposed torque control algorithm functions properly.

5.8 Copper and Iron losses

Copper losses are already presented in eq. (5.50). Using the field orientation method described in section 5.7, it is possible to calculate iron losses in the device. Iron losses mainly depend on the magnetic polarisation and the pulsation of the flux density in the material. Kowal et al. (2011) study the influence of the core material on the performance of PS synchronous machines for wind turbine applications. The paper includes both saturation and hysteresis losses. The saturation characteristics for two different materials (M235-35A and M800-65A) are listed in Fig. 5.11.

The first three digits of the name stand for the maximal value of the specific loss at 50 Hz and 1.5 T (e.g. M235 $\rightarrow$ 2.35 W/kg), wheras the last two digits depict the thickness of the laminations (e.g. 35A $\rightarrow$ 0.35 mm thickness). As seen on Fig. 5.11, steel M235-35A has a higher permeability and a

[2]for more information: `http://nl.mathworks.com/help/optim/ug/equation-solving-algorithms`

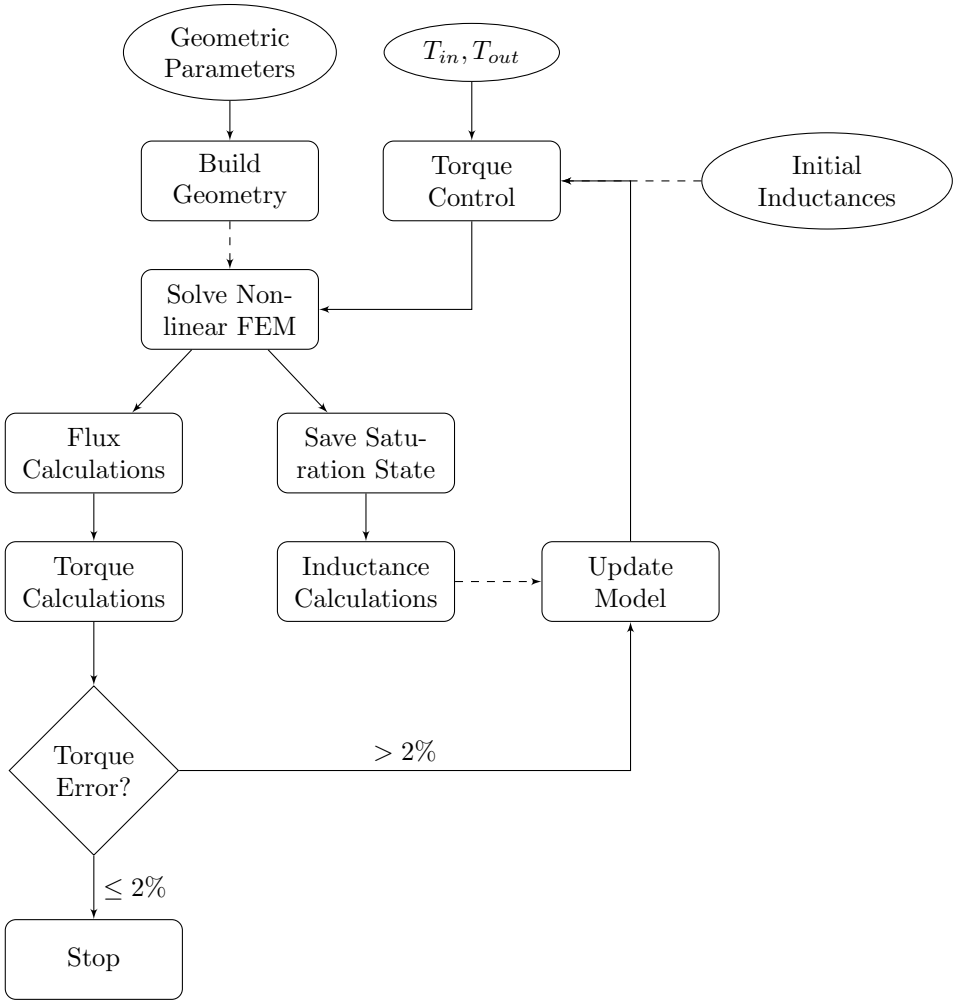

Figure 5.10: Flowchart of iterative field oriented torque control algorithm

lower saturation level than M800-65A. The higher permeability makes M235-35A more favourable for machines operating mostly at partial load (Kowal et al., 2011). In vehicle applications, the transmission system is only occasionally fully loaded. Consequently, steel M235-35A is chosen. Bertotti (1998) presents in his book a semi-empirical formulas based on statistical loss theory in order to calculate the core losses. The theory relies on the principle of loss separation into hysteresis, classical and excess losses. According to this study, the core loss can be described by:

$$P_{fe} = m_{fe} \left[a\, B^{\alpha}\, f + b\, B^2\, f^2 + c\, B\, f \left(\sqrt{1 + d\, B\, f} - 1 \right) \right] \tag{5.61}$$

with:

- $B = \frac{\Psi}{w\, S_{yoke}}$: the peak induction in corresponding iron core yoke;
- f: the pulsation frequency in the corresponding iron core;
- a, α, b, c and d: material parameters derived on statistical basis. Table 5.4 presents the values

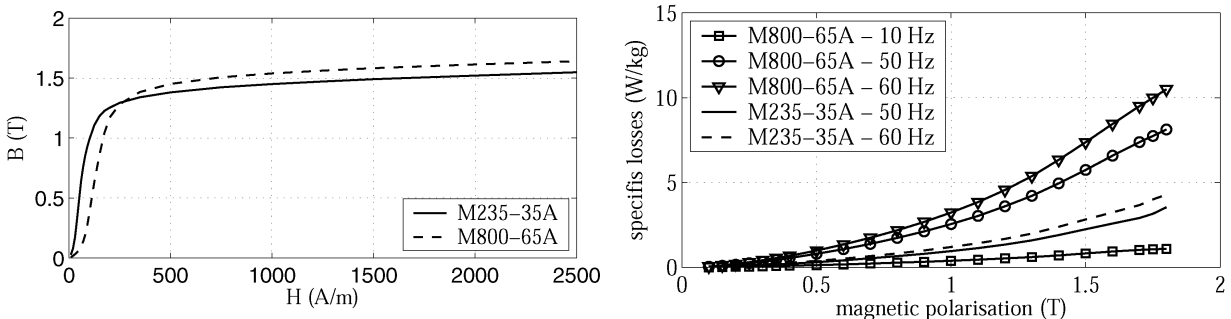

(a) BH-characterisic **(b)** specific losses

Source: Kowal et al. (2011).

Figure 5.11: Magnetization characteristics of two material grades

of these parameters for M235-35A steel.

	a	α	b	c	d
M235-35A	0.0178	2.0000	4.7018×10^{-5}	0.1075	0.0005

Source: Kowal et al. (2011).

Table 5.4: M235-35A core loss parameter

The first part of eq. (5.61) represents static hysteresis losses, which are a linear function of the frequency and an exponential function of the magnetic flux density. The second part presents the classical losses, which include dynamic eddy-current effects, and the last part corresponds to an excess loss which is basically an empirical correction factor for the theoretical model.

The slip-pulsations of both the rotor and the interrotor can be derived using eq. (5.53). The stator pulsation is evaluated as:

$$\omega = N_p \, \Omega_2 + s_2 \omega \tag{5.62}$$

The slip in interrotor and rotor can now be calculated:

$$s_2 = \frac{s_2 \omega}{\omega} \tag{5.63a}$$

$$s_3 = \frac{\omega - N_p \, \Omega_3}{\omega} \tag{5.63b}$$

Consequently, the pulsation frequency of the magnetic flux density is known.

$$f_1 = \frac{\omega}{2\pi} \tag{5.64a}$$

$$f_2 = \frac{s_2 \omega}{2\pi} \tag{5.64b}$$

$$f_3 = \frac{s_3 \omega}{2\pi} \tag{5.64c}$$

Because the pulsation frequency in the interrotor is low, interrotor iron losses are neglected in the coming analyses.

Chapter 6

EVT geometrical optimization

The previous chapter presents the finite element model of the EVT. This chapter describes the results of several simulations. A geometrical optimization is performed in function of the interrotor inner and outer radii. The optimization algorithm is executed on both the fixed stator (classical) topology and the moving stator (inverted) topology. In the latter, the stator functions as the input shaft, whereas the rotor is fixed and functions as the housing of the device. The reasons for the inversion of the mechanical connections are listed in the corresponding paragraphs.

6.1 Geometrical optimization

This section describes the simulation model of a geometrical optimization of the EVT. The optimization is executed for a specific operating point. Druant et al. (2015) study a similar machine using a linear model. The authors conclude that the operating point with maximal efficiency is located at 1300 rpm (N_{out}) and 20 Nm (T_{out}). Consequently, the output speed and torque are fixed in this simulation. The input speed (connected to the ICE) is set at 1500 rpm (N_{in}), which is a typical value for a diesel ICE. In order to meet the power balance, the below procedure calculates the corresponding input torque:

- Firstly, the device is assumed lossless. The corresponding input torque can be written as:

$$T_{in,ini} = \frac{N_{out}}{N_{in}} T_{out} \tag{6.1}$$

- Subsequently, the FOC algorithm (section 5.7) can be performed since both input and output torque/speed are known. The torque control results in currents, fluxes and slip pulsations in both the stator, the interrotor and the rotor. Therefore, copper (P_{cu}) and iron (P_{fe}) losses can be calculated.

- In a following iteration the input torque is updated taking into account the losses:

$$P_{in,i+1} = P_{out} + P_{cu,i} + P_{fe,i} \tag{6.2a}$$

$$T_{in,i+1} = \frac{P_{in,i+1}}{\frac{2\pi}{60} N_{in}} \tag{6.2b}$$

- The procedure is stopped when the input torque deviation between two succeeding iterations is less than 0.1 %.

$$Dev = \left| \frac{T_{in,i+1} - T_{in,i}}{T_{in,i+1}} \right| < 0.1\,\% \tag{6.3}$$

The above method evaluates for both the input and output torque of the machine. Consequently, the iterative FOC presented in Fig. 5.10 can be started. Once the solution is converged, the efficiency of the machine is evaluated as:

$$\eta = \frac{P_{out}}{P_{in}} \tag{6.4}$$

This procedure is executed for an inner interrotor radius (r_2) between 55 and 85 mm, and an outer interrotor radius (R_2) between 60 and 90 mm. Additionally, the thickness of the interrotor is enclosed between 5 mm and 20 mm.

6.1.1 Moving stator topology

As mentioned in the introduction, a second topology is studied as well. In this topology, the inner core -previously called the rotor- is fixed, while the outer core -previously called the stator- is connected to the input shaft. There are several reasons to switch the functions of stator and rotor:

- Unlike a single rotor induction machine, the torque acting on the stator is mostly much smaller than on the rotors. Based on the third law of Newton, the torques acting on the stator and rotor of a single rotor induction machine are equal. In the EVT, a double rotor induction machine, the torque acting on the stator is the difference between rotor and interrotor torque. Consequently, the stator torque is much smaller and the corresponding currents in the stator are thus smaller as well. Fig. 6.1 represents the slot surface of both stator, interrotor and rotor in function of the interrotor inner and outer radii. The stator slot surface is a single function of the interrotor outer radius, whereas the rotor slot surface is only dependent on the interrotor inner radius. The interrotor slot surface is dependent on both quantities. As expected, the interrotor slot surface increases with increasing radii and increasing interrotor width. Fig. 6.1 shows that the surface area range of the stator is larger than that of the rotor. Since the copper resistance and thus the losses are inversely related tot the slot surface, it is advantageous to fix the inner rotor. In this way, the losses are more equally distributed between stator and rotor, and overall losses are likely to be lower.

- Because the internal losses significantly reduces, an inverted EVT requires potentially a smaller cooling system.

- For automotive applications, a rotating stator has also a mechanical advantage. It increases the inertia connected to the engine. This yields that the additional engine inertia can be reduced or even removed, which is advantageous for the overall powertrain efficiency.

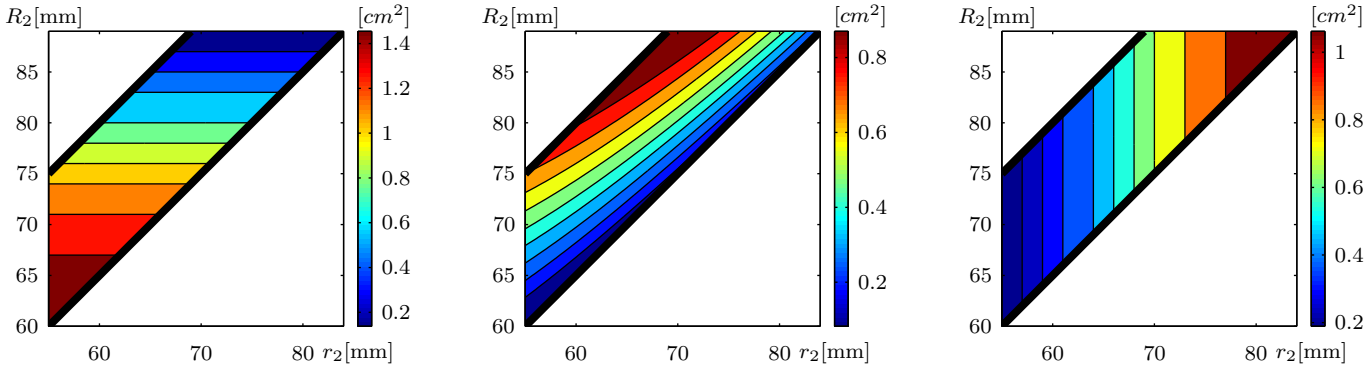

(a) stator **(b)** interrotor **(c)** rotor

Figure 6.1: Slot surface area in function of inner and outer interrotor radii (9 kW IM-based EVT)

- Finally, a moving stator topology resembles the hydraulic torque converter more than a moving rotor topology.

6.2 Optimal geometry of the fixed stator topology

This section presents the results of the geometrical optimization of the EVT connected in the classical way, i.c. fixed stator and rotating rotor. Because the simulation model includes the iterative FOC algorithm, both magnetic and electric machine parameters can be evaluated for each geometry.

6.2.1 Currents and fluxes

Figs. 6.2 and 6.3 show respectively the current distribution and self-inductances for both stator, interrotor and rotor. Fig. 6.2 shows the magnitude of the current field vector in both stator (Fig. 6.2a) and rotor (Fig. 6.2b). Due to FOC, the current in the interrotor cage is fixed along the negative q-axis having a value of $158,7$ A. It is clear that the current in the stator decreases with increasing radii, whereas the current in the rotor increases with increasing radii, caused by the minimization of the losses in the FOC method. Since the number of turns of the stator equals that of the rotor, both currents can be added in order to have an idea about the total current in the machine. The total current in presented in Fig. 6.2c. The total current is decreasing with increasing radii. Because the torque on the interrotor and rotor is constant with increasing radii, the total airgap force decreases due to the increased radii. Consequently, the currents are expected to be lower. Additionally the quotient of the airgap width and the (inter)rotor diameter decreases with increasing radii. Therefore, stator, interrotor and rotor are magnetically more coupled for increasing radii. The latter can be verified looking to Fig. 6.3. The figure presents the average of the q- and d-axis self-inductances in both stator, interrotor and rotor. The values of those inductances express both the level of saturation and the coupling between the rotors and stator. The absolute value depends

on the total number of turns of the windings and is thus less relevant. However, relative values are of great importance.

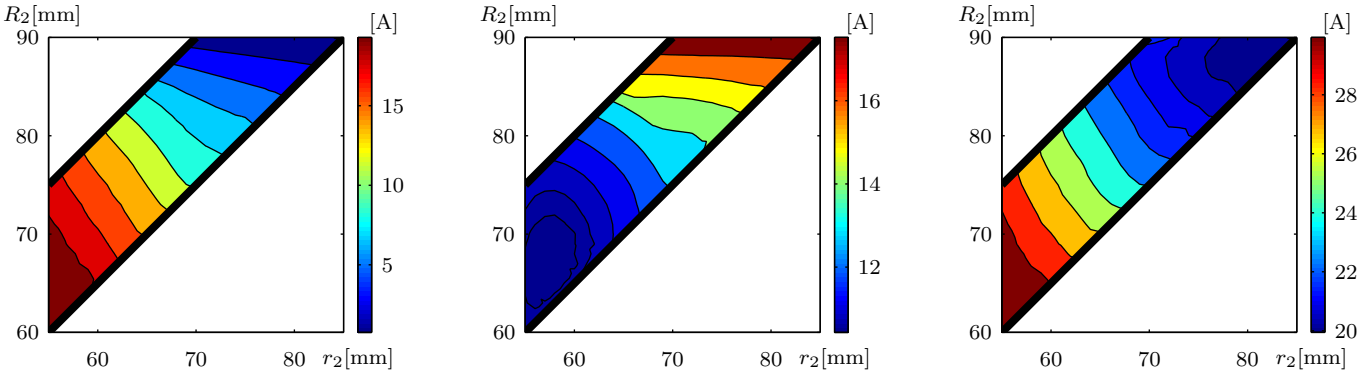

(a) stator **(b)** rotor **(c)** total(stator+rotor)

Figure 6.2: Currents in function of the variable radii (9 kW IM-based EVT, fixed stator)

The self-inductances of both the stator, interrotor and rotor have a maximum around $r_2 = 70\,\text{mm}$ and $R_2 = 80\,\text{mm}$. To understand this phenomenon, three different magnetic fields are plotted for increasing radii in Fig. 6.4. The figure shows that the saturation level in both the stator and the rotor are relatively similar for intermediate radii (Fig. 6.4b). For lower radii (Fig. 6.4a), the saturation level of the stator increased since the magnetic path through the stator is long and the currents in the stator are high. Because the core material saturates very fast when the field is increased above 1.5 T, the required magnetic field intensity is increased as well. Therefore, inductances are generally lower. For higher radii (Fig. 6.4c), a similar reasoning can be made. According to the above argumentation, the maximum inductances should be located where the magnetic path is both stator and interrotor are equal. Fig. 6.4b contradicts this statement. The inductances are also influenced by the coupling between stator, interrotor and rotor. Because the relative airgap width is decreasing for increasing radii, the linkage between the iron cores is increased. Consequently, the maximum inductances are pushed towards higher internal radii of the machine.

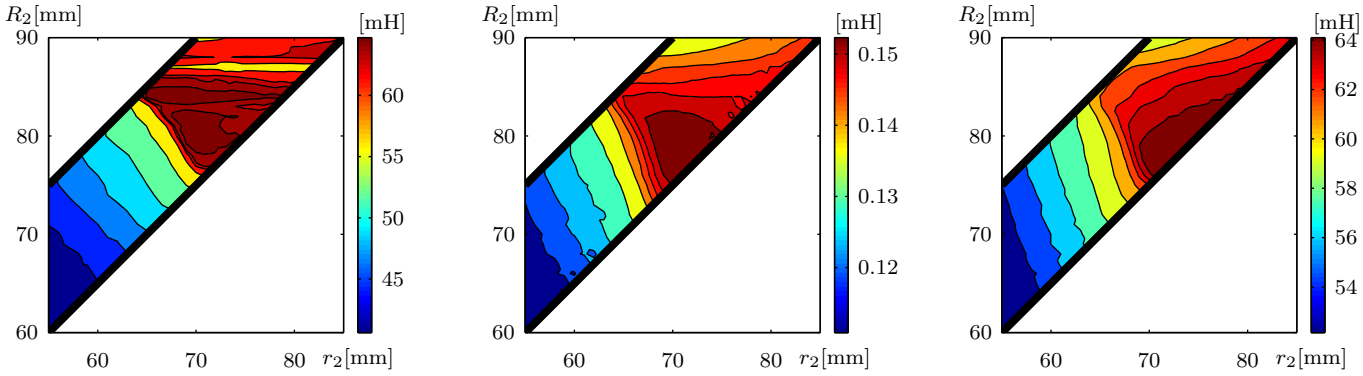

(a) stator **(b)** interrotor **(c)** rotor

Figure 6.3: Average self-inductances in function of the geometry (9 kW IM-based EVT, fixed stator)

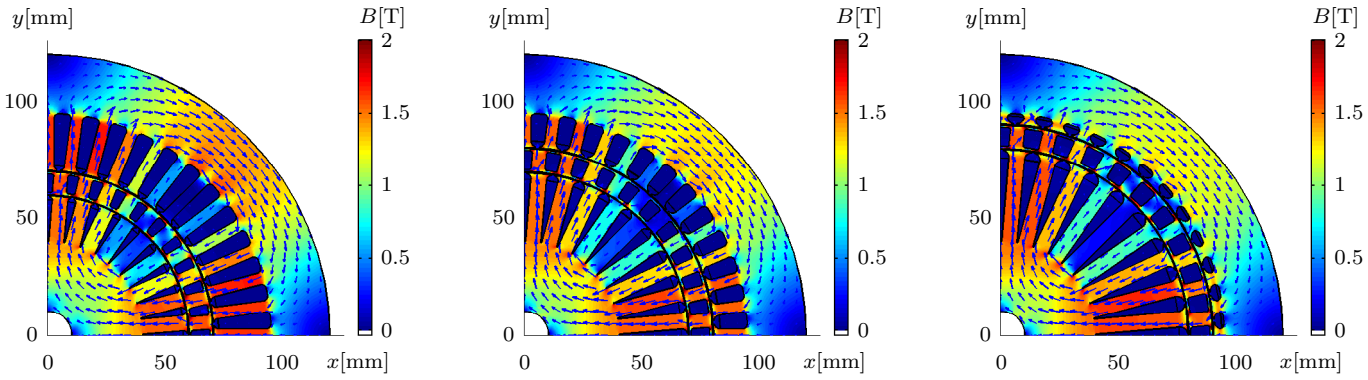

(a) $r_2 = 60\,\text{mm}, R_2 = 70\,\text{mm}$ **(b)** $r_2 = 70\,\text{mm}, R_2 = 80\,\text{mm}$ **(c)** $r_2 = 80\,\text{mm}, R_2 = 90\,\text{mm}$

Figure 6.4: Magnetic field for different geometries (9 kW IM-based EVT, fixed stator)

6.2.2 Losses and overall efficiency

Figs. 6.5 and 6.6 represent the losses in the EVT. Fig. 6.5 shows the total losses (copper plus iron losses) in each part, whereas Fig. 6.6 shows the copper and iron losses separately over the complete device. Fig. 6.6b concludes that iron losses are of small importance as the losses are only 10 % of the

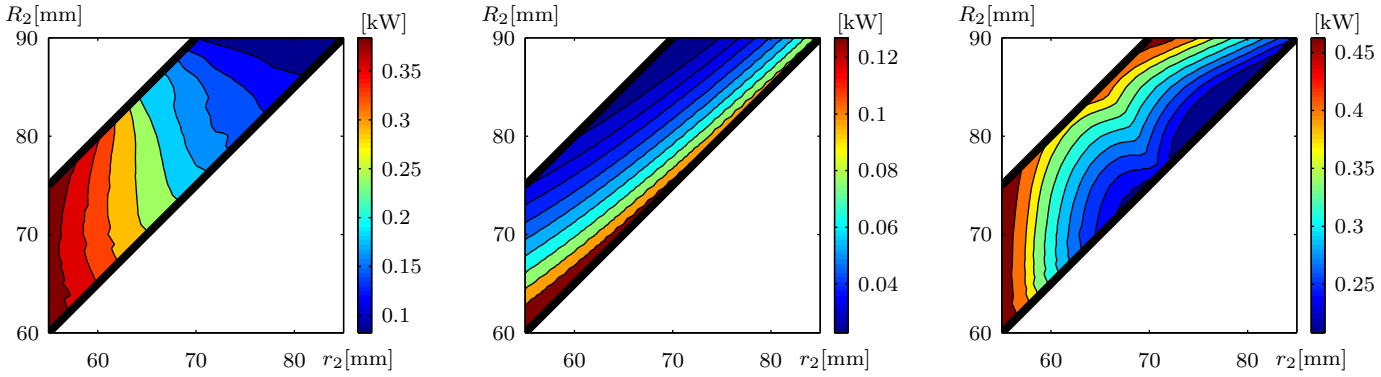

(a) stator **(b)** interrotor **(c)** rotor

Figure 6.5: Loss distribution in function of the variable radii (9 kW IM-based EVT, fixed stator)

corresponding copper losses. The figure also demonstrates that iron losses decrease with increasing radius. Due to the better coupling for higher radii, the flux density level in the machine is decreased causing less iron losses. Since the fraction if the iron losses is small, the losses in Figs. 6.5a to 6.5c can be completely assigned to copper losses. Copper losses are strongly influenced by the slot area of the corresponding winding. Despite the decreasing stator slot area, the stator losses are decreasing for higher radii as consequence of the strongly decreased stator current. The loss distribution of the interrotor has the same course as the interrotor surface because the interrotor current is constant. Unlike the stator, the total losses in the rotor are not uniformly increasing with increasing radii. The shape of Fig. 6.5c can be assigned to two competing effects. On the one hand, copper losses are decreasing due to the increasing copper section. On the other hand, iron losses are increasing due to the increasing iron section. The cave around (70 mm, 75 mm) is caused by the high inductance

values, which cause both a decreased flux and current level in the rotor.

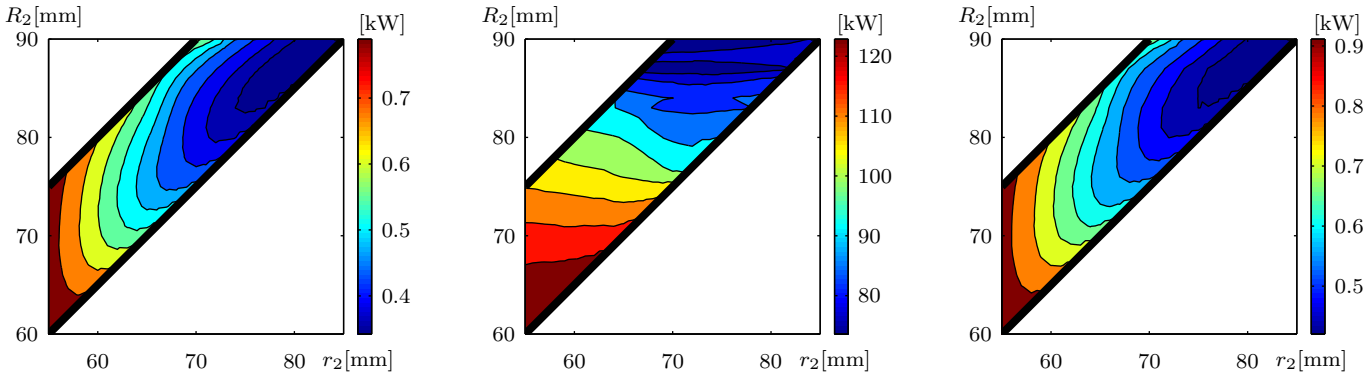

(a) copper losses **(b)** iron losses **(c)** total losses

Figure 6.6: Losses in function of the variable radii (9 kW IM-based EVT, fixed stator)

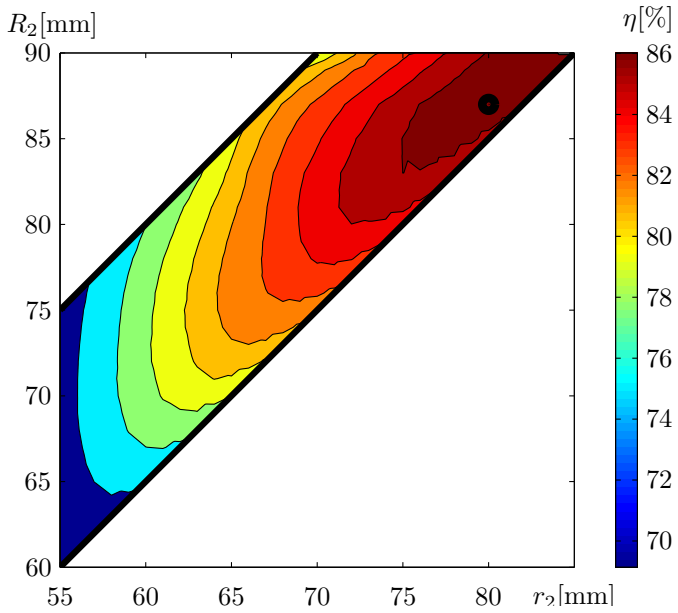

Figure 6.7: Geometric efficiency of 9 kW IM-based EVT (fixed stator)

In conclusion, it can be stated that the total losses in the EVT are composed by the complex interaction of currents and fluxes. The total losses are smaller for higher radii. When the inner and outer radii reaches their maximum values, the losses start to increase again due to the very small copper section of the stator and the decreasing inductances in both the interrotor and the rotor. These conclusions are verified using Fig. 6.7 which represents the overall electromagnetic efficiency of the device. The efficiency is the smallest for the smallest radii (69 %). The maximum efficiency is reached at $r_2 = 80$ mm and $R_2 = 87$ mm having a value of 86.6 %. Note that this optimal point is determined without taking into account mechanical constraints. Because the interrotor width is only 7 mm, it is possible to have mechanical strength issues. This strength analysis is a subject for a mechanical study of the EVT and is not treated in this master thesis. Nevertheless, the optimal

geometry denoted on Fig. 6.7 is used in the following of this paper.

6.3 Optimal geometry of the moving stator topology

This section discusses similar graphs as in the previous section for the moving stator topology. The stator functions as the input shaft, whereas the rotor functions as the housing and is fixed.

6.3.1 Currents and fluxes

Figs. 6.8 and 6.9 are equivalent to Figs. 6.2 and 6.3 of the previous section. Because moving stator topology is geometrically optimized for the same working point, the torque on the interrotor is still 20 Nm and thus the interrotor current is still $158,7\,\mathrm{A}$. Similar to the fixed stator topology, the currents in the stator are decreasing for increased radii, whereas the currents in the rotor are increasing. However, the absolute values differ from the previous study. Since the torque on the stator is high compared to the classical topology, the stator currents are higher as well. For the same reasons the rotor current is lower than in section 6.2.1. Note that however the torque on the stator is multiplied by a factor five, the currents in the stator are only a bit higher than in the fixed stator topology. The reason for this divergence yields the relative high radius of the airgap transforming the input torque. Similar conclusions are made for the rotor current. The range of the total current (i.c stator plus rotor current), presented in Fig. 6.8c, is relatively smaller compared to Fig. 6.2c. The maximum total current is decreased from 32 A to 26 A. Moreover, the minimal total current region is not any more located at the largest radii. Instead, in the region around $(70\,\mathrm{mm}, 80\,\mathrm{mm})$, the total current is minimized. Additionally, it can be seen that the region of low total current is larger than the same region for the fixed stator topology. Due to the low total current in the $(70\,\mathrm{mm}, 80\,\mathrm{mm})$-region the corresponding self-inductances of both stator, rotor and interrotor presented in Fig. 6.8 are high. For the same reasons as in the previous section, the maximum inductances are pushed outwards. Since the currents in the rotor are smaller than in last section, the corresponding saturation level is somewhat decreased and consequently the inductances are a bit higher than for the fixed stator topology.

6.3.2 Losses and overall efficiency

Figs. 6.11a to 6.11c reveal the losses in each part of the machine. Similar to the fixed stator topology, the interrotor losses follow the same course as the interrotor copper section. On the other hand, the course of both stator and rotor are completely different compared to Fig. 6.5. The stator currents are decreased less rapidly with increasing radii, which results in very high losses when the stator copper section is low (for high radii). The minimal stator loss is also increased due to the higher currents. Additionally, the minimum is located at the middle of the inner interrotor diameter range because stator loss formation consist of a competition of two factors:

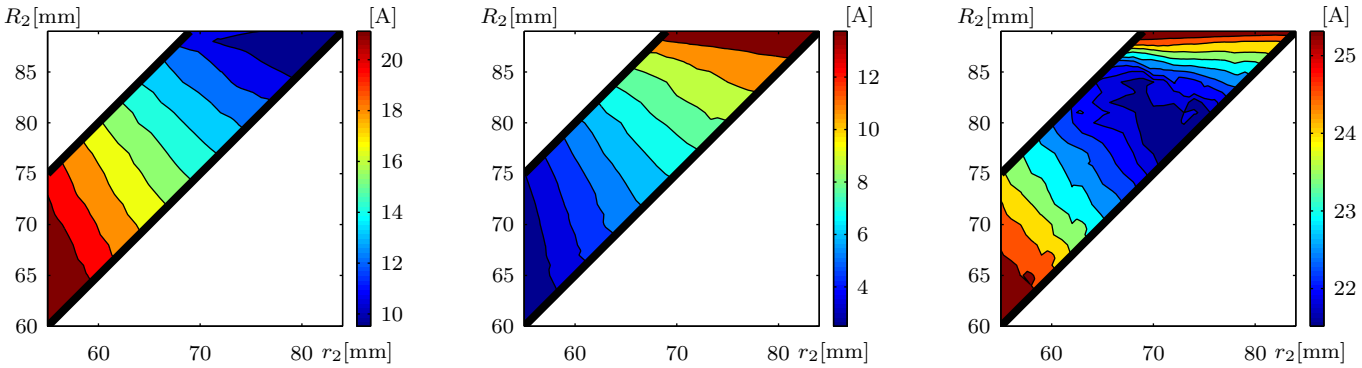

(a) stator **(b)** rotor **(c)** total(stator+rotor)

Figure 6.8: Currents in function of the variable radii (9 kW IM-based EVT, moving stator)

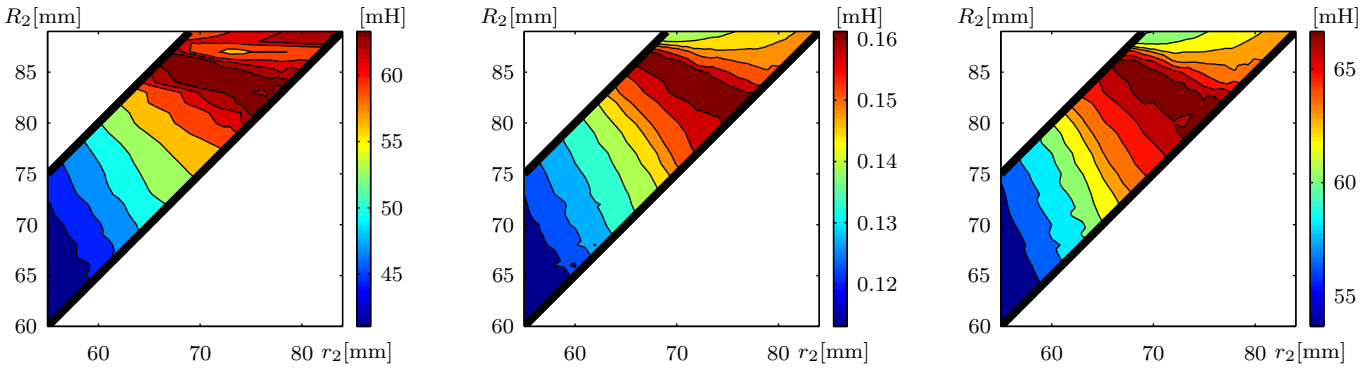

(a) stator **(b)** interrotor **(c)** rotor

Figure 6.9: Average self-inductances in function of the geometry (9 kW IM-based EVT, moving stator)

- Lower stator currents, but also a smaller copper section for larger radii;
- Higher stator currents, but also a larger copper section for smaller radii.

Rotor losses are increasing with increasing radii. Because rotor currents increase strongly with increasing radii, the total rotor loss raises, even if the rotor copper section is increased as well. Note that there is a large region in Fig. 6.11c wherein the rotor losses are relatively low. Taking into account these considerations, the total loss is presented on Fig. 6.12c. Since the stator currents are higher compared to the classical topology the geometry of least losses is not any more located at very high radii. Instead, the balance between stator, interrotor and rotor losses is located more in the middle of the radius' ranges. Because the pulsation of the magnetic field in the heaviest part (stator) is much lower than in the fixed stator design (slip pulsation vs. supply frequency), the total iron losses are much lower as well. Compared to Fig. 6.6b the maximum core loss is halved. Moreover, the course of the losses is inverted, due to the lower mass of the part with highest pulsation (fixed rotor), which also tents to lower the radius of minimal losses.

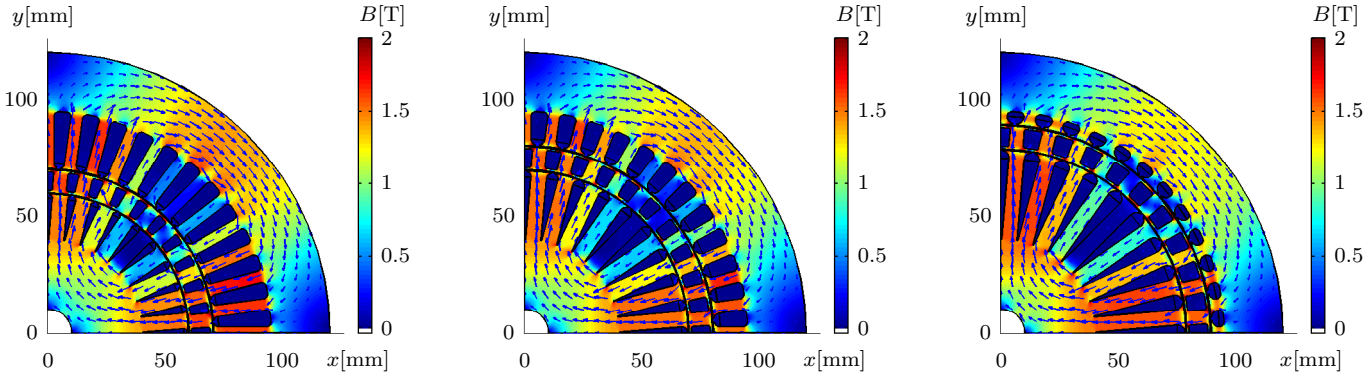

(a) $r_2 = 60\,\text{mm}, R_2 = 70\,\text{mm}$ **(b)** $r_2 = 70\,\text{mm}, R_2 = 80\,\text{mm}$ **(c)** $r_2 = 80\,\text{mm}, R_2 = 90\,\text{mm}$

Figure 6.10: Magnetic field for different geometries (9 kW IM-based EVT, moving stator)

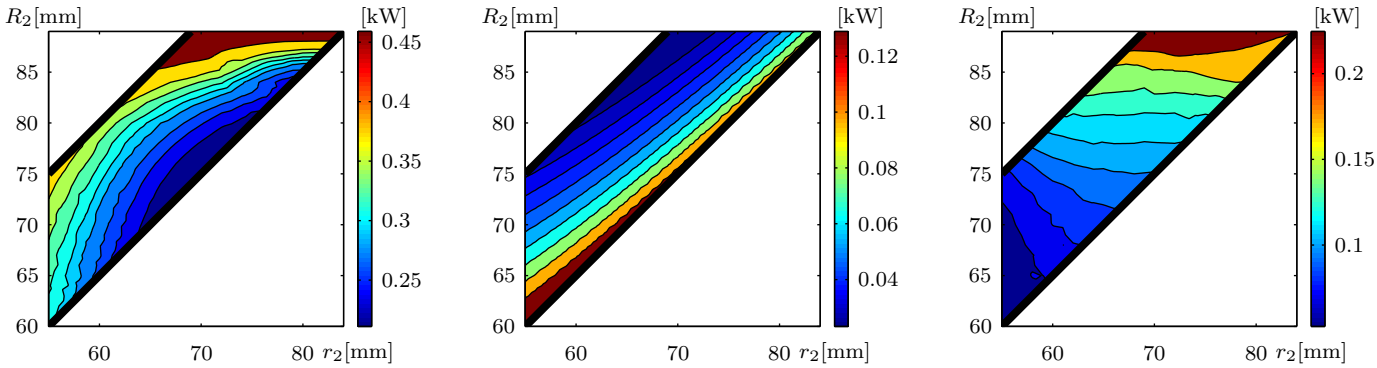

(a) stator **(b)** interrotor **(c)** rotor

Figure 6.11: Loss distribution in function of the variable radii (9 kW IM-based EVT, moving stator)

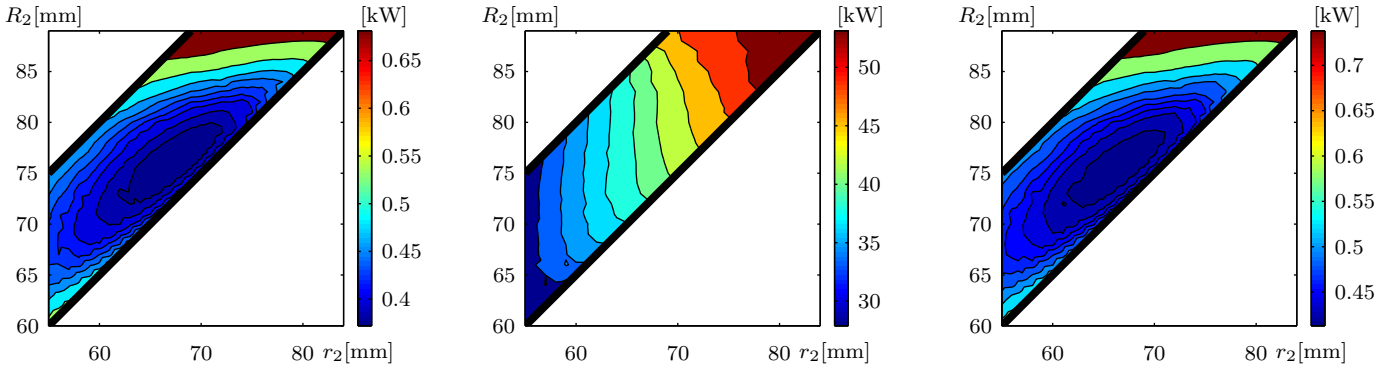

(a) copper losses **(b)** iron losses **(c)** total losses

Figure 6.12: Losses in function of the variable radii (9 kW IM-based EVT, moving stator)

Fig. 6.13 shows the corresponding efficiency of the moving stator topology. As already mentioned above, the maximal efficiency point is located in the middle of the radius' ranges. The corresponding optimal radii are: $r_2 = 60\,\text{mm}$ and $R_2 = 76\,\text{mm}$. The efficiency of the optimal geometry is 86.8 %. Even if this value is only a little higher than for the fixed stator topology, the high efficiency region in Fig. 6.13 is much larger than in Fig. 6.7. Consequently, when adaptations have to be made

for constructive or mechanical strength reasons, the corresponding adapted geometry would have a higher efficiency, compared to the fixed stator topology.

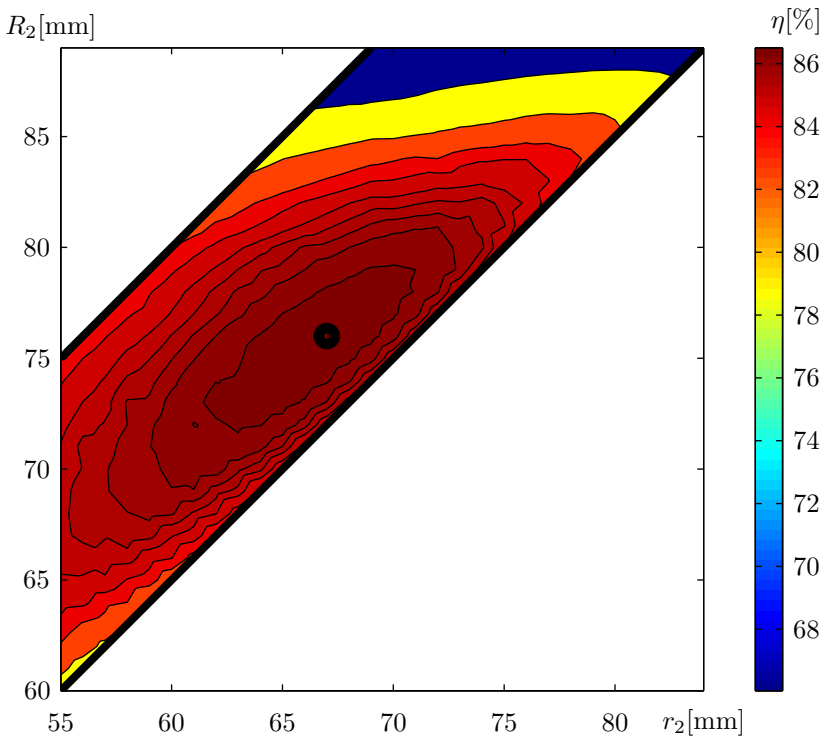

Figure 6.13: Geometric efficiency of 9 kW IM-based EVT (moving stator)

6.4 Comparison of topologies

This section gives an overview of the parameters of the optimal geometry found in previous sections. Table 6.1 includes all mechanical and electrical parameters of both the fixed and moving stator topologies. Additionally, eqs. (6.5a) and (6.5b) contain the complete inductance matrix of the corresponding optimal geometry. As already mentioned, there is almost no difference in total loss for both topologies. Consequently, both topologies seems to be as efficient. On the other hand, looking to the internal (i.c. interrotor and rotor) currents and losses, it is clear that the moving stator topology has the advantage. The rotor current and rotor losses of the latter are smaller compared to the fixed stator topology. It is believed that stator heat can be removed more easily than rotor heat, even if the stator is rotating. The inverted topology requires thus a smaller cooling system. Moreover, as explained in section 6.3, the region of high efficiency is larger in function of the interrotor inner and outer radius. Therefore, the geometry can be adapted without extensively increasing electrical losses in the device. The latter also favours the use of the moving stator system. Finally, the stator has a higher inertia than a the rotor. Connected to an ICE, the inverted topology could significantly stabilize ICE operation. On the other hand, the biggest advantage of the fixed

stator design is its simplicity. In this case, the stator functions also as the casting whereas the inverted topology requires an additional casting.

In conclusion, based on this geometrical analysis for a single operation point, the winning topology is not clear. Both cases have their own advantages and have, although their optimized geometry differs a lot, similar efficiencies. The choice of the topology is thus dependent on the operational limits of the device studied in next chapter. Note that only the radii are investigated in this paper. If a more detailed geometrical study is required, the airgaps, the stator and rotor yoke, the saturation bridges and other geometrical parameters should be included in the optimization analysis.

	Classic	Inverted
r_2 [mm]	80	67
R_2 [mm]	87	76
Scu_1 [mm^2]	28.70	100.3
Scu_2 [mm^2]	34.72	35.75
Scu_3 [mm^2]	123.5	57.78
Res_1 [Ω]	2.360	.6453
Res_2 [Ω]	.0019	.0018
Res_3 [Ω]	.5446	1.094
N_{in} [rpm]	1500	1500
N_{out} [rpm]	1300	1300
T_{in} [Nm]	−20.02	−19.96
T_{out} [Nm]	20	20
$I_1\,(q,d)$ [A]	$(-.1266, -3.312)$	$(-8.002; -13.23)$
$I_2\,(q,d)$ [A]	$(-158, 7, 0)$	$(-158.7; 0)$
$I_3\,(q,d)$ [A]	$(-7, 784, -14.99)$	$(-.0362; -6.629)$
$\Psi_1\,(q,d)$ [Wb]	$(-.0073; -.8139)$	$(.0386; -0.91)$
$\Psi_2\,(q,d)$ [Wb]	$(0; -0.042)$	$(0; -0.042)$
$\Psi_3\,(q,d)$ [Wb]	$(.0364; -.9238)$	$(-.0043; -.8532)$
$P_{cu,1}$ [W]	38.88	$231, 6$
$P_{cu,2}$ [W]	71.85	68.23
$P_{cu,3}$ [W]	233.1	72.13
$P_{fe,1}$ [W]	72.04	8.90
$P_{fe,2}$ [W]	0	0
$P_{fe,3}$ [W]	4.32	31.92
P_{cu} [W]	343.0	372
P_{fe} [W]	76.4	40.8
P_{loss} [W]	420.2	412.8
P_{in} [W]	3143	3135
P_{out} [W]	2723	2723
η [%]	86.63	86.83

Table 6.1: Optimal geometric parameters for 9 kW IM-based EVT

$$\mathsf{L}_{\mathsf{ind,classic}}\,[\mathrm{mH}] = \begin{bmatrix} 65.09 & 2.87 & 55.02 & 0.96 & 0.03 & -2.38 \\ 2.87 & 0.16 & 3.05 & 0.01 & .002 & -0.13 \\ 55.02 & 3.05 & 71.87 & 0.82 & 0.05 & 1.58 \\ 0.96 & 0.01 & 0.82 & 60.03 & 2.42 & 41.20 \\ 0.03 & .002 & 0.05 & 2.42 & 0.13 & 2.26 \\ -2.38 & -0.13 & 1.58 & 41.20 & 2.26 & 54.81 \end{bmatrix} \tag{6.5a}$$

$$\mathsf{L}_{\mathsf{ind,inverted}}\,[\mathrm{mH}] = \begin{bmatrix} 68.35 & 2.93 & 47.06 & 2.58 & 0.02 & 0.60 \\ 2.93 & 0.15 & 2.56 & -0.17 & .003 & 0.08 \\ 47.06 & 2.56 & 67.79 & -2.90 & 0.08 & 1.34 \\ 2.58 & -0.17 & -2.90 & 55.51 & 2.06 & 33.57 \\ 0.02 & .003 & 0.08 & 2.06 & 0.13 & 2.18 \\ 0.60 & 0.08 & 1.34 & 33.57 & 2.18 & 60.56 \end{bmatrix} \tag{6.5b}$$

Chapter 7

EVT operating analysis

As section 5.7.4 explains, the iterative field oriented control procedure is capable of controlling both the input and the output torque of the EVT. Additionally, using the procedure explained in section 6.1, the input torque is adapted such that the power balance is consistent.

The previous chapter presents simulations dealing with the geometry of the EVT for the two different topologies. In this chapter, the same simulation model is used to investigate the performance of the machines in function of the output torque and speed. The main goal of this chapter is to provide an efficiency map of the EVT.

7.1 Efficiency map of the fixed stator topology

In order to understand the working principle of the EVT, the operating modes of the power-split transmission of section 2.3 are adapted to the EVT. Fig. 7.1 shows schematically the reference powerflow directions in the EVT. These reference directions are chosen positive in the power-split mode of the PS-CVT. In this non-regenerative mode, the powerflow is straight forward and is explained as the following:

- The power enters the EVT through the rotor. Consequently, the input power equals:

$$P_{in} = \Omega_{in} * T_{in} \tag{7.1}$$

- The rotor functions as a power-split device. A part of the power leaves the rotor electrically through the converters ($P_{el,in}$), another part ($P_{f,in}$) leaves the rotor electromagnetically through the inner airgap, whereas a third part ($P_{loss,3}$) of the input power is lost due to iron and copper losses. The inner airgap power and electrical power leaving the rotor are calculated as:

$$P_{f,in} = \frac{\omega}{N_p} * T_{in} \tag{7.2}$$

$$P_{el,in} = \left(\Omega_{in} - \frac{\omega}{N_p}\right) * T_{in} - P_{loss,3} \tag{7.3}$$

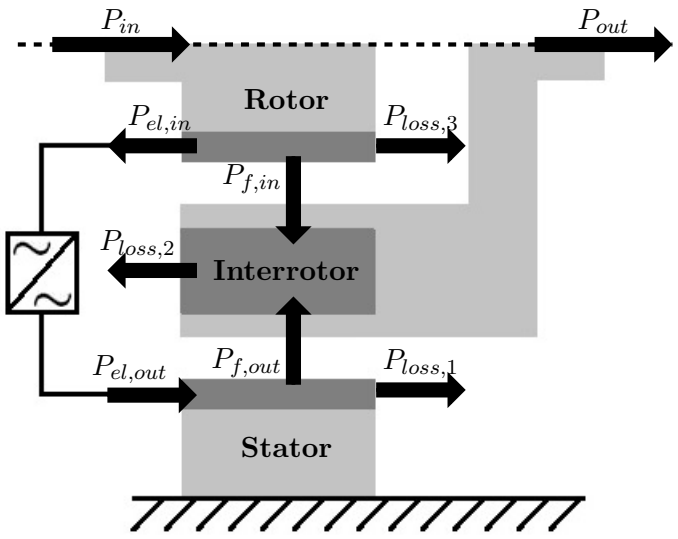

Figure 7.1: Powerflow references in the EVT (fixed stator)

with ω the electrical pulsation of the field. The rotor is regarded as an induction machine in generation mode. The rotor speed is higher than the speed of the magnetic field in order to produces electricity.

- As explained in Chapter 5, losses in the converters are neglected. The input power of the converters equals the output power of the converters:

$$P_{el,out} = P_{el,in} \tag{7.4}$$

  Note that the power loss in the converters can easily be included in the analysis, if the corresponding losses are assigned to the stator and/or rotor windings.

- The stator accepts power coming from the converters and transforms it into electromagnetic power in the outer airgap by means of its winding.

$$P_{f,out} = P_{el,out} - P_{loss,1} \tag{7.5}$$

- In the interrotor, the inner and outer airgap power are added. This power, subtracted by the interrotor losses, is transferred through the interrotor to the output shaft of the EVT.

$$P_{out} = P_{f,in} + P_{f,out} - P_{loss,2} \tag{7.6}$$

  Since the interrotor accepts electromagnetic power through both the inner and the outer airgap, the interrotor functions as an induction machine in motor mode. Due to the FOC on the interrotor, the slip of the interrotor is positive and thus the interrotor rotates at a lower speed than the magnetic field.

When the speed of the interrotor exceeds the speed of the rotor, the slip on the rotor turns positive. In this case, the interrotor functions as a generator and sends power to the converters. In the rotor, the power from converters is added to the input power and electromagnetically transferred through the inner airgap. Therefore, both $P_{el,out}$, $P_{el,in}$ and $P_{f,out}$ have negative values.

7.1.1 Power and efficiency

The efficiency map of the 9 kW IM-based EVT (fixed stator topology) is plotted in Fig. 7.2. As expected, the highest efficiency occurs at 1500 rpm. The speed of the rotor equals the speed of the interrotor. The maximum electromagnetic efficiency is near 90 %. This value approaches the total efficiency of an induction machine of the same size. In practice, the total efficiency is somehow lower than 90 %, since the total efficiency also includes mechanical and cooling losses. Furthermore, the efficiency decreases when the interrotor speed is decreased. Because a lower interrotor speed increases slip in the rotor, the rotor losses are increased. A higher interrotor speed turns the machine into its regenerative mode. Since the variator (the converter) is assumed to be lossless, the efficiency decreases in the same way as for a reduced interrotor speed.

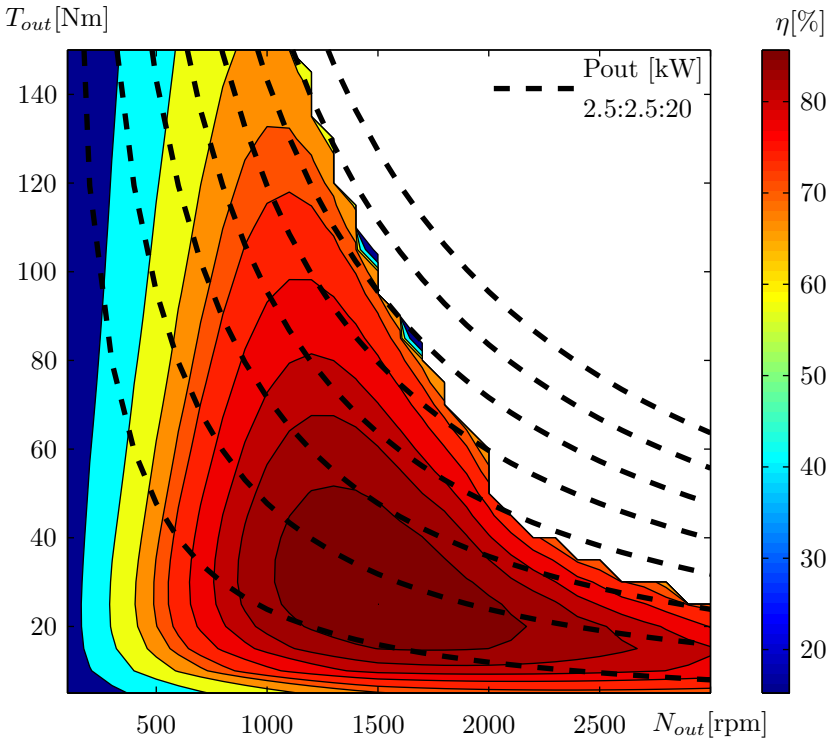

Figure 7.2: Efficiency map of 9 kW IM-based EVT ($N_{in} = 1500$ rpm, fixed stator)

The interface between the white region and the coloured region represents a power limit. For a constant output speed, the demanded power increases with increasing output torque. Since the input speed is constant as well, the rotor torque increases more than proportional with the output power due to internal losses. Therefore, the power balance can not be satisfied any more for high

power demand. Fig. 7.3 presents the machine input, output and power loss in function of the input torque for three different operating points. The output speed is fixed at 2000 rpm, whereas the output torque is varied between 60 and 80 Nm. The total machine loss is only a little dependent on the output torque, because the torque variation at the input is much higher. The power loss has a quadratic course. Furthermore, since the input speed is fixed, the input power is linear. The operating point of the machine is the intersection between the full and dash-dotted lines. For $T_{out} = 60\,\text{Nm}$ and 70 Nm, there is an intersection point. Consequently, the input power can be transmitted. For $T_{out} = 80\,\text{Nm}$, the intersection point does not longer exist because the output power exceeds the dash-dotted line. The very abrupt stability limit is caused by the quadratic course of the losses. Since the dash-dotted line is the difference between the input power and the power loss, the line relatively flat around its maximum. Therefore, when the output power is increased only a bit, the machine is not able to transfer the demanded power any more.

It is evident that the stability region for lower output speeds is much higher. The machine losses are more or less independent of the output speed. If it is assumed, in a first stage, that the machine losses do not depend on the output torque too, the stability line on Fig. 7.2 would agree with a constant powerline. However, in practice, the losses are dependent on the output torque. The stability line, thus, deviates form the constant powerlines. Fig. 7.4 presents the input power, machine losses and output power on a constant powerline of Fig. 7.2. The losses are plotted in function of the input torque and output speed. Since the output power is held constant, the green, blue and red full lines are on the same hight. The graph shows that the losses increase when the output speed increases. Therefore, the stability line exceeds the power line for relatively low speeds, whereas the order is reversed for higher speeds.

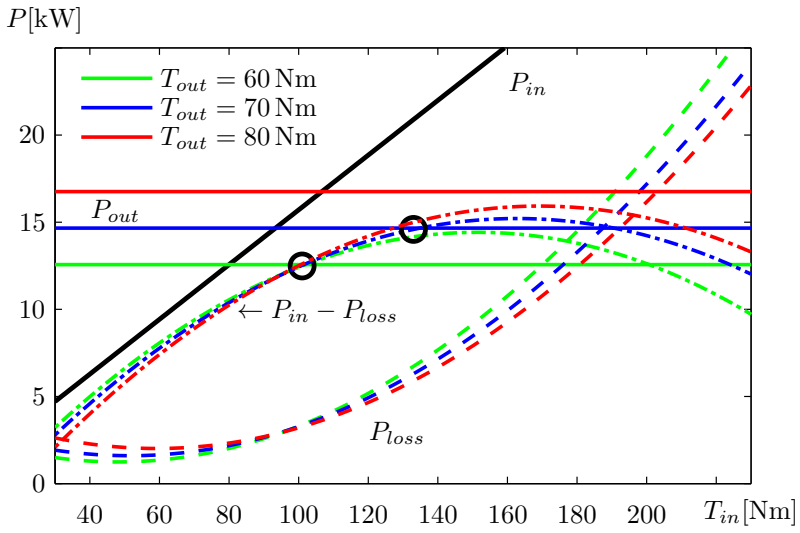

Figure 7.3: Power limits at $N_{in} = 1500\,\text{rpm}$ and $N_{out} = 2000\,\text{rpm}$ (fixed stator)

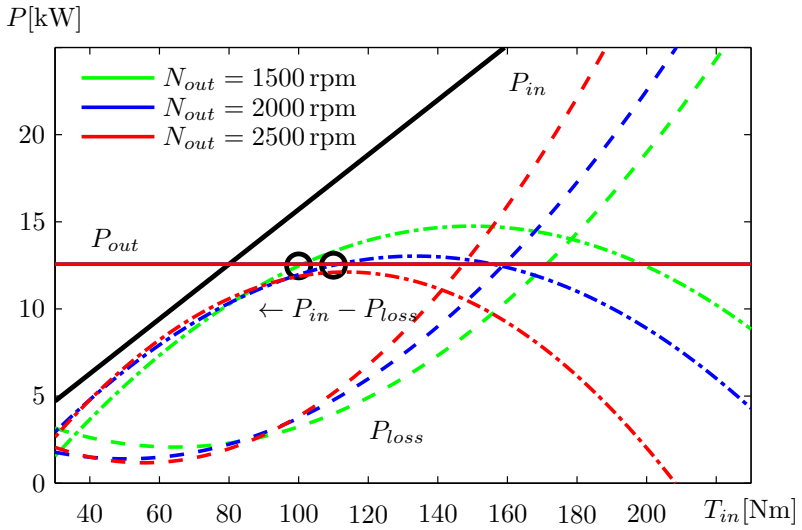

Figure 7.4: Power limit at $N_{in} = 1500\,\text{rpm}$ and $P_{out} = 12.5\,\text{kW}$ (fixed stator)

Figs. 7.5a to 7.5c represent respectively the stator supply frequency, the slip in the interrotor and the slip in the rotor. As expected, the supply frequency mainly varies with the output speed. The interrotor slip is proportional interrotor torque, which agrees with the slip equation (eq. (5.53)). Additionally, because the interrotor flux is constant, the slip is inversely proportional to the supply frequency. The rotor slip, presented on Fig. 7.5c, has basically the same course as the supply frequency because the rotor speed is kept constant. As already highlighted in the beginning of this section, the rotor slip is negative in power-split mode since the rotor functions as a electricity generator (for low output speeds). In overdrive mode the slip turns positive as the rotor function a motor and adds the power from the converters to the input power of the driving axis.

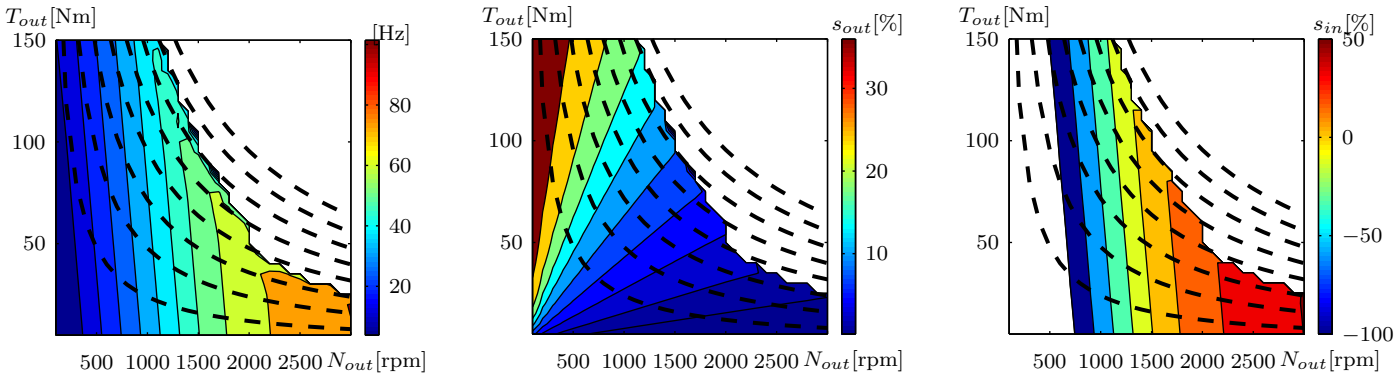

(a) supply frequency (stator) **(b)** output slip (interrotor) **(c)** input slip (rotor)

Figure 7.5: Supply frequency, input and output slip (9 kW IM-based EVT, fixed stator)

In the following figures the electrical power through the converters is plotted conform to the references of Fig. 7.1. The electrical power is positive when the interrotor speed is below the rotor speed (negative rotor slip). The maximum power through the converters is obtained at very low speed

and high torque. Since this situation only occurs sporadically in vehicle applications, converters with a low relatively nominal power can be chosen. Fig. 7.6b scales the electrical power with the input power. Since the EVT is an output-coupled PS transmission, the electrical power fraction in 100 % at standstill. Because the simulation is started from a minimum speed of 100 rpm, the standstill situation is not shown on the figure. The maximum electrical power fraction on Fig. 7.6b yields 60 %. It is clear that the electrical power fraction decreases very fast with the output speed of the EVT. It is also observed that the electrical fraction is mainly a function of the output speed, as it is strongly related to the rotor slip. I.c. for speed range between 500 and 2000 rpm, the power through the converters is included between −50 % and 50 % of the total power through the device. Concluding, the rated power of the converters is halved with respect to the serial electrical machine connection, presented in section 2.2.3.

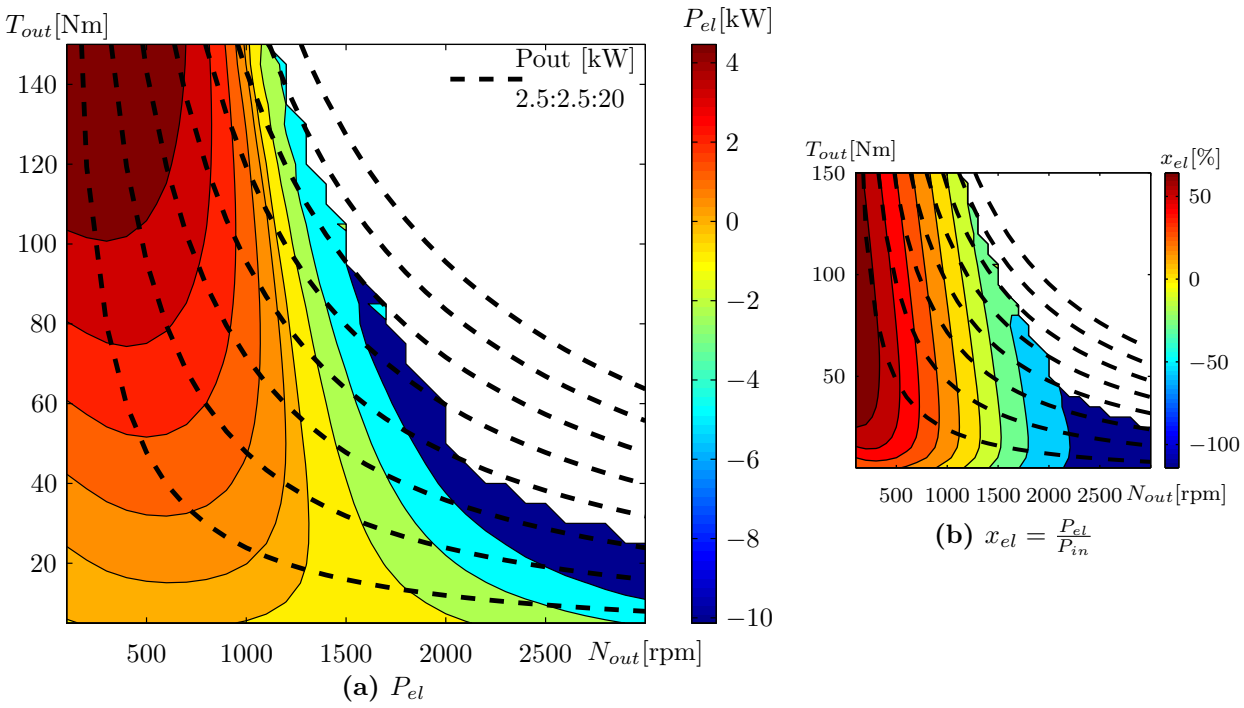

Figure 7.6: Electrical power (fraction) through the converters (9 kW IM-based EVT, fixed stator)

7.1.2 Currents and Losses

In the previous section, the main characteristics of the efficiency map are presented along with a verification of the theoretical operation principles in both operation modes. This section discusses more in detail the currents, and thus the losses, in the device. It is of great importance to understand the causes of the losses in order to optimize the design and the operating limits.

In the subsequent figures, the currents in each winding are presented. The interrotor current is a single function of the output torque, because of the field oriented torque control. The stator currents clearly reach a minimum in the low slip region, since electrically transferred power is minimal. In

that region, the rotor torque equals the interrotor torque. Therefore, torque on the stator almost zero. Note that this situation is impossible in conventional induction machines since the stator current is required to provide the rotor flux level. In an EVT the interrotor flux is built by both the stator and the rotor. Consequently, one of the field currents can build the flux on its own. Additionally, the stator current tents to increase very fast for high torque and low speed, whereas rotor currents mainly depend on the output power.

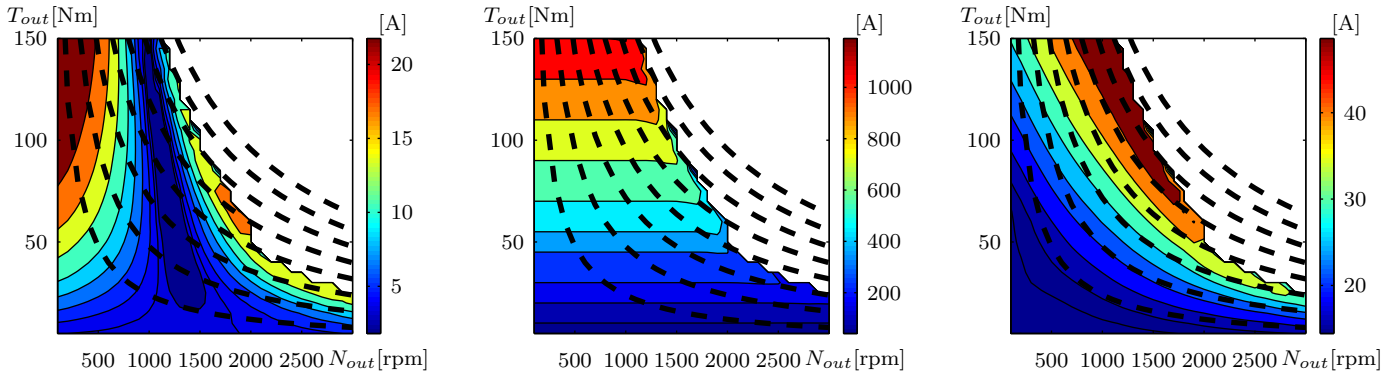

(a) stator **(b)** interrotor **(c)** rotor

Figure 7.7: Currents in function of the operating point (9 kW IM-based EVT, fixed stator)

The total losses in both stator, interrotor and rotor are shown in Fig. 7.8. Because the losses are mainly composed of resistive losses, the course of the losses almost equals the course of the corresponding currents. Note that the order of magnitude of the power losses in both stator, interrotor and rotor is equal. However, for high output torque, the losses in the interrotor significantly exceed losses in stator and rotor. In Fig. 7.9, copper and iron losses are plotted separately. Similar to the geometrical optimization, the iron losses are only a fraction of the total losses. Additionally, the iron losses are proportional to the pulsation of the magnetic flux density in both stator and rotor. Consequently, they are minimal in the direct-drive region. Fig. 7.9c presents the total losses of the device in function of the operating point. It is clear that the losses increase mainly with the output torque and that the losses are minimised around the direct-drive mode.

Using Fig. 7.9c, the rated power of the machine is estimated. The rated power depends on a thermal analysis which is out of the scope for this research. However, it may be estimated, assuming that the rated losses may not exceed the rated losses of a typical induction motor of 9 kW. The rated losses of 9 kW induction motor are evaluated as following:

$$P_{loss,rated} = (1 - \eta_{rated}) * P_{rated} \tag{7.7}$$

using the WEG[1] online catalogue, the total efficiency of a typical induction motor is 91 %. The corresponding total losses are 830 W. The red line on Fig. 7.9c presents such a power loss and thus the regime operation region is limited by the red curve. The corresponding rated maximal output

[1] `http://catalogo.weg.com.br/tec_cat/tech_motor_sel_web.asp`

power is 5.5 kW and the corresponding efficiency is 87.5 % which is very close to the maximum electromagnetic efficiency of 87.8 %.

Note that this is a very simplified approach in which it is assumed that the heat dissipation of the EVT is as efficient as in a usual induction motor. In practice, this is not be the case, since the machine is composed out of two airgaps. Furthermore, the total efficiency of an electrical device includes also ventilation and mechanical losses, whereas the electromagnetic efficiency only includes electromagnetic losses (copper and iron losses). In order to obtain a better estimate of the rated power, a more detailed thermal study is required. Additionally, the power limit presented in this section is based on a forced air-cooled IM. It is believed that other cooling systems, such as water cooling, are possible as well. Due to the increased cooling capacity, water cooling could certainly increase the thermal power limit of the device.

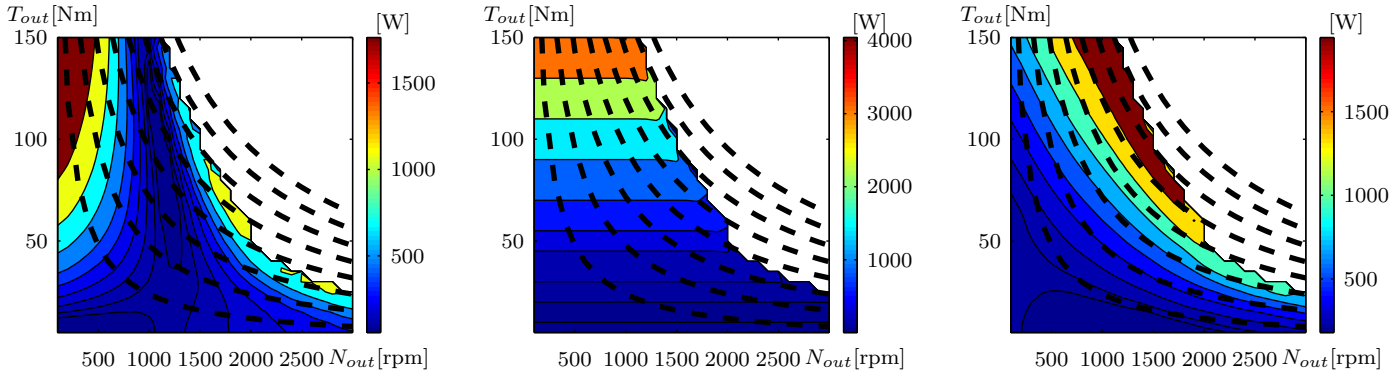

(a) stator **(b)** interrotor **(c)** rotor

Figure 7.8: Loss distribution in function of the working point (9 kW IM-based EVT, fixed stator)

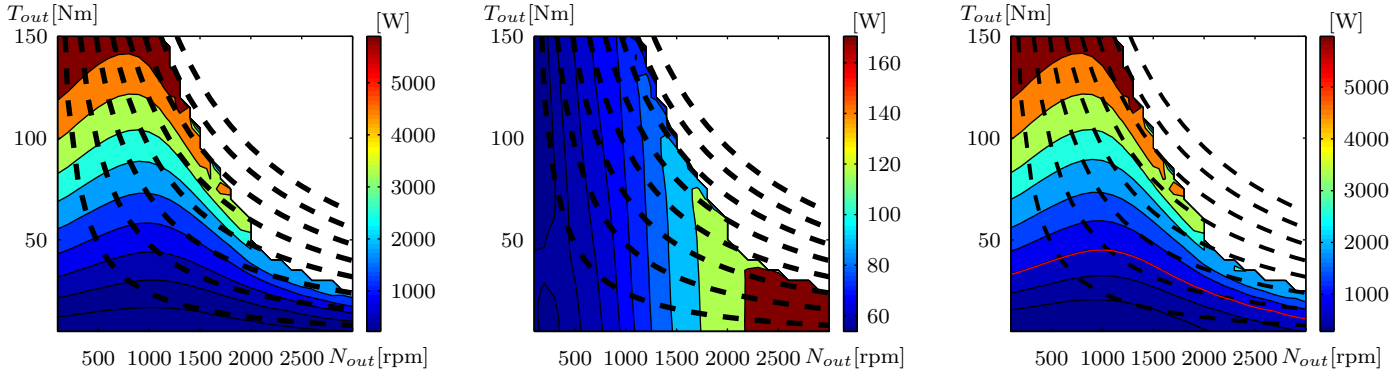

(a) copper losses **(b)** iron losses **(c)** total losses

Figure 7.9: Losses in function of operating point (9 kW IM-based EVT, fixed stator)

7.2 Efficiency map of the moving stator topology

Similar to the fixed stator topology, the efficiency map of the moving stator topology is simulated as well. In the previous chapter, a geometrical analysis concludes that there is no significant

difference between the two topologies for the given working point. In this section, both topologies are compared based on their operating limits and operating efficiency. The powerflow references for the moving stator topology are presented in Fig. 7.10. The relations between all powerflows are similar to eqs. (7.1) to (7.6) if subscript 1 is replaced by 3 and vice versa.

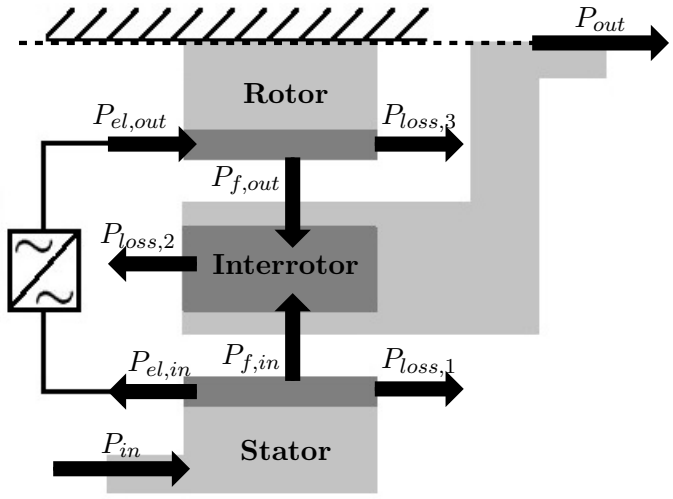

Figure 7.10: Powerflow references in the EVT (moving stator)

The efficiency map is plotted in the following figures. The maximal efficiency is located at $N_{out} = 1500\,\text{rpm}$ and $T_{out} = 25\,\text{Nm}$ and yields 88.4 %. There is thus only a small difference in efficiency between the two topologies. On the other hand, the stability region has significantly increased compared to previous design.

In Fig. 7.12, the stability limits are investigated for $N_{out} = 2000\,\text{rpm}$. It is observed that the losses are reduced compared to the fixed stator topology. For example, at $T_{in} = 200\,\text{Nm}$ the total machine loss yields 12 kW. For the same input torque the losses in Fig. 7.3 are over 15 kW. Because of the lower losses, a higher output torque can be transferred and the stability region is enlarged significantly. Fig. 7.13 plots a close-up of the magnetic field around the interrotor. The presented figures correspond to an output speed of 1300 rpm. The magnetic field density increases along the tooth tips. By consequence, the tooth tips and interrotor bridges saturate more for increased torque. For $T_{out} = 20\,\text{Nm}$, the interrotor bridges do not saturate a lot. Consequently, there is a considerable leakage flux through the bridges and the efficiency of the device decreases. When the torque is high, all interrotor bridges are saturated. Therefore, interrotor magnetic leakage is low. On the other had, the saturation level of the teeth is increased as well. A larger magnetic field intensity, and thus more current, is required to produce the same flux level. In conclusion, the efficiency of the EVT is the result the complex interaction between magnetic leakage and saturation level of the iron cores and has its maximum for intimidate torque levels. Note that similar results can be concluded for the fixed stator topology of the previous section.

The frequency and slip have, apart from the larger stability region, equal courses in both fixed and

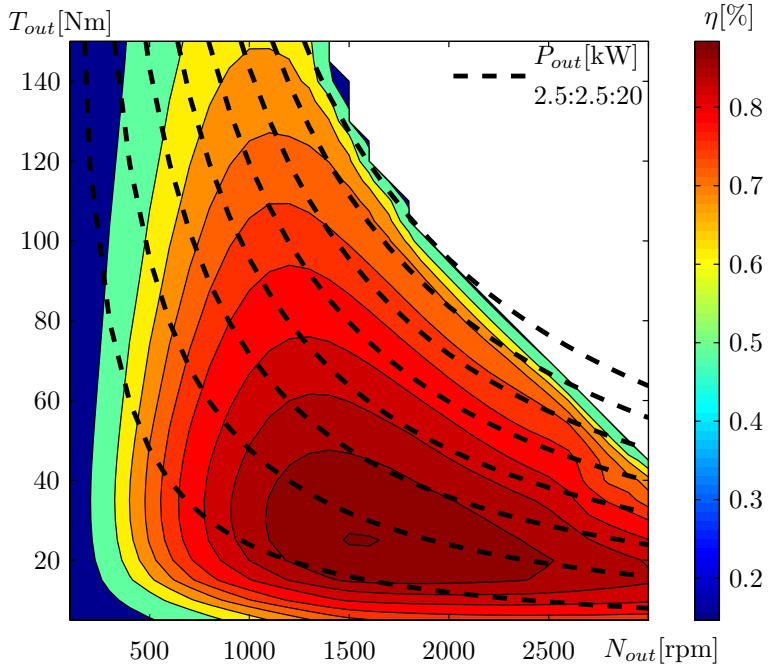

Figure 7.11: Efficiency map of 9 kW IM-based EVT (moving stator)

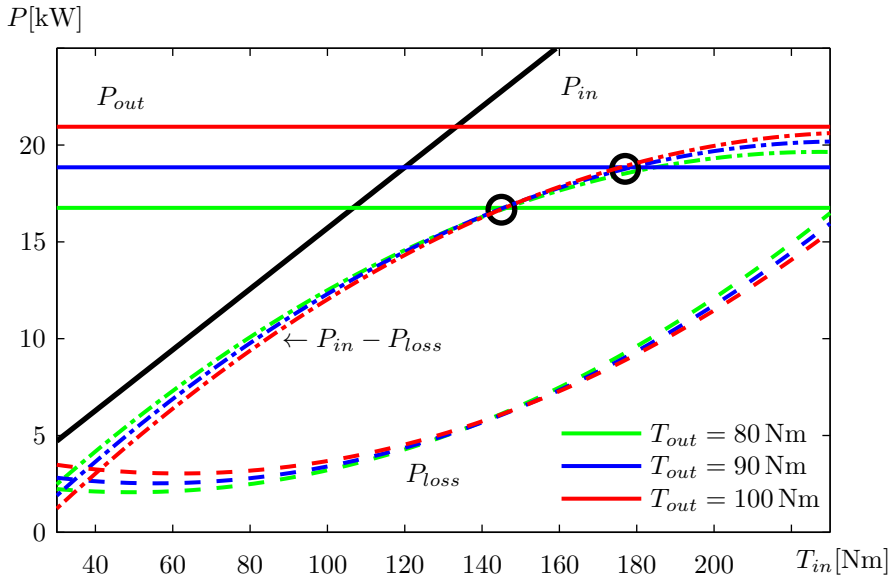

Figure 7.12: Power limit at $N_{in} = 1500$ rpm and $N_{out} = 2000$ rpm (moving stator)

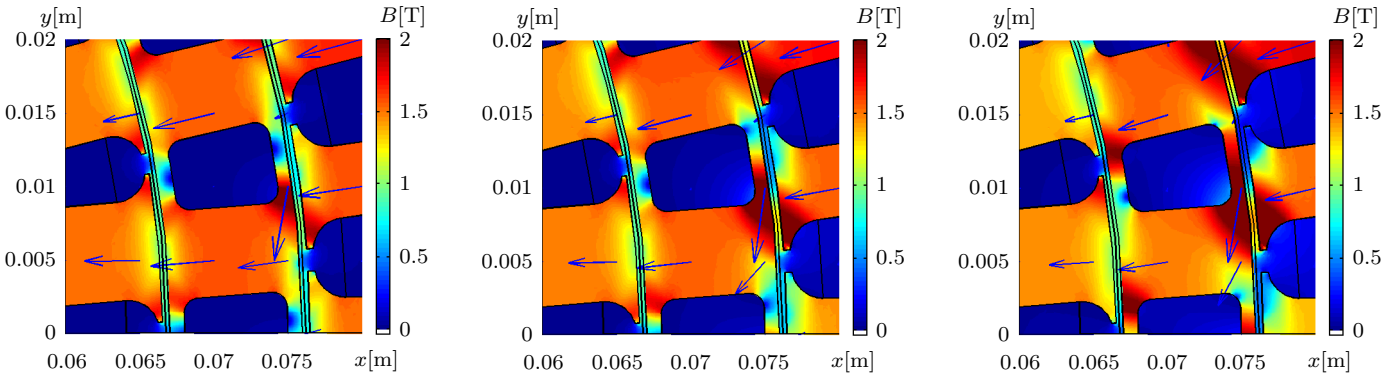

(a) $T_{out} = 20$ **(b)** $T_{out} = 60$ **(c)** $T_{out} = 100$

Figure 7.13: Magnetic field for increasing output torque ($N_{out} = 1300$ rpm, moving stator)

moving stator topologies. The stator supply frequency is decreasing for lower interrotor speed and slowly increasing for higher torque, since more slip is required to produce high torque. In the low speed region, the slip in the stator (Fig. 7.14c) is strongly negative due to the constant ICE speed (values beyond -1 are not shown).

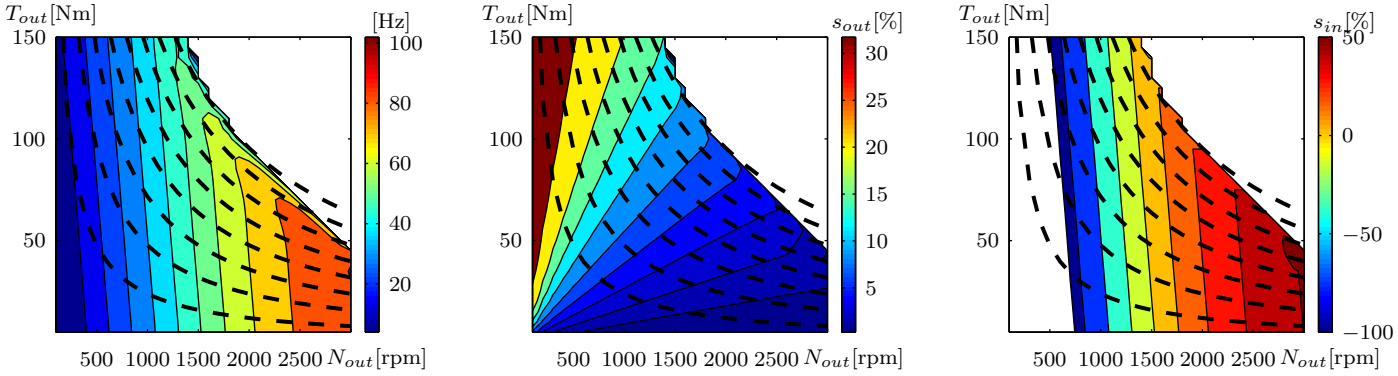

(a) supply frequency (fixed rotor) **(b)** output slip (interrotor) **(c)** input slip (moving stator)

Figure 7.14: Supply frequency, input and output slip (9 kW IM-based EVT, moving stator)

The maximal power through the converters yields 6 kW as shown on Fig. 7.15a located at $N_{out} = 700$ rpm and $T_{out} = 150$ Nm. Note that the electrical power showed on the figure is enclosed between -10 and 5 kW. Because the electrical power is strongly negative (lower than -10 kW) close to the stability line, those values are not displayed (and thus white). Similar to the fixed stator topology, it is concluded that the power through the converters is halved in a broad speed range compared to a serial electrical machine connection (Fig. 7.15b).

7.2.1 Currents and losses

It is clearly seen in Fig. 7.16 that the function of the stator and rotor is inverted compared to the fixed stator topology. Losses in the rotor are low in a very large operating region. This can be advantageous, since it is difficult to remove rotor losses. Note that close to the stability line, currents

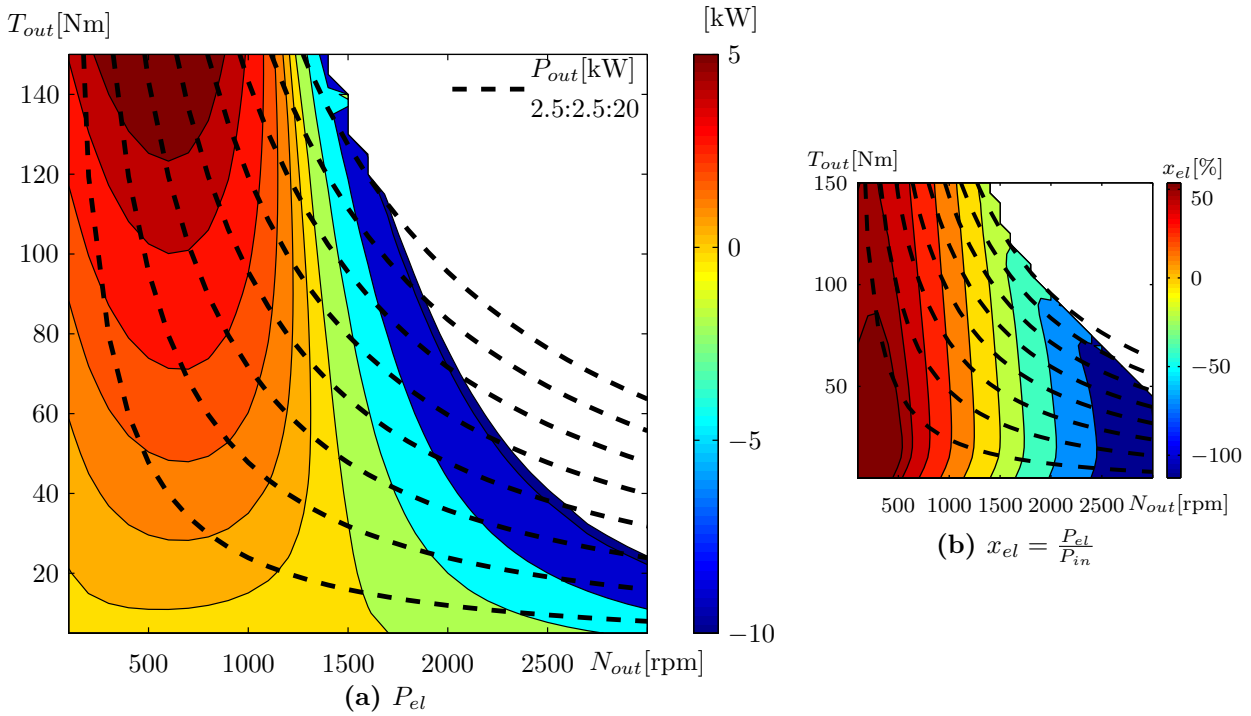

(a) P_{el} **(b)** $x_{el} = \frac{P_{el}}{P_{in}}$

Figure 7.15: Electrical power (fraction) through the converters (9 kW IM-based EVT, moving stator)

in both stator and rotor are increasing very fast. Consequently, the operation of the machine in this region has to be avoided, even during transients.

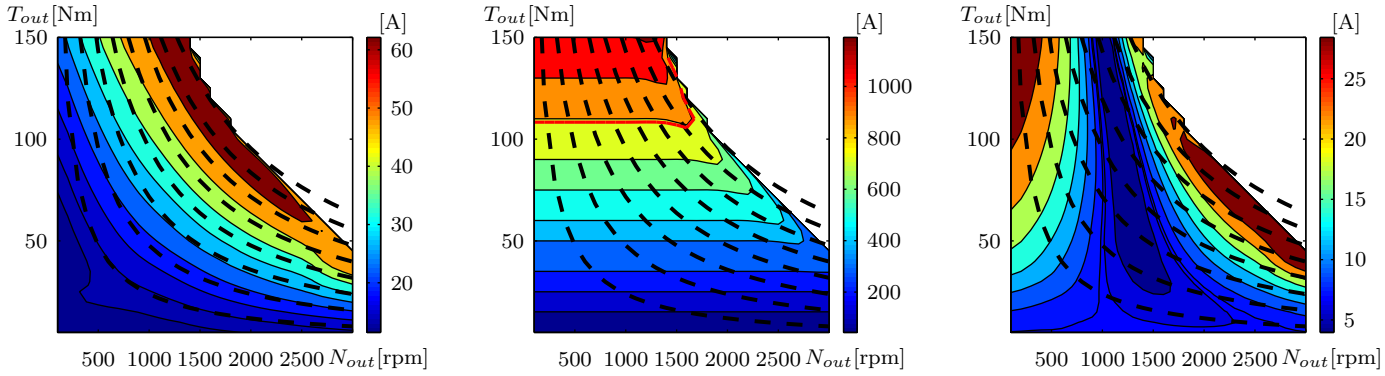

(a) stator **(b)** interrotor **(c)** rotor

Figure 7.16: Currents in function of the operating point (9 kW IM-based EVT, moving stator)

Unlike iron losses in the fixed stator topology, the iron losses in the moving stator topology are not monotonically increasing with the output speed. Instead, there is a minimum around the input speed as the slip frequency in the stator is low and thus iron losses are low. The course of the figure is caused by the fact that the losses in both the stator and the rotor are of the same order. I.c for low speed, the slip frequency in the stator is high and losses increase; for high speed, the supply frequency in the rotor is high and iron losses increase as well. The total losses are presented in Fig. 7.18c. Due to the increased efficiency of the moving stator topology, the maximum rated loss

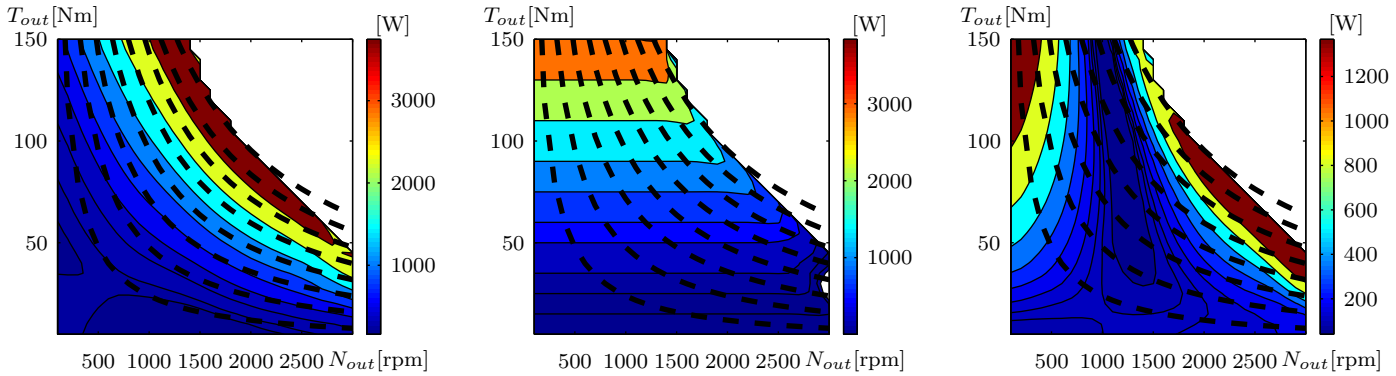

(a) stotor **(b)** interrotor **(c)** rotor

Figure 7.17: Loss distribution in function of operating point (9 kW IM-based EVT, moving stator)

line is moved upwards compared to Fig. 7.9c. Nevertheless, the difference is very small. The rated power of the air-cooled inverted topology, consequently, equals 6 kW.

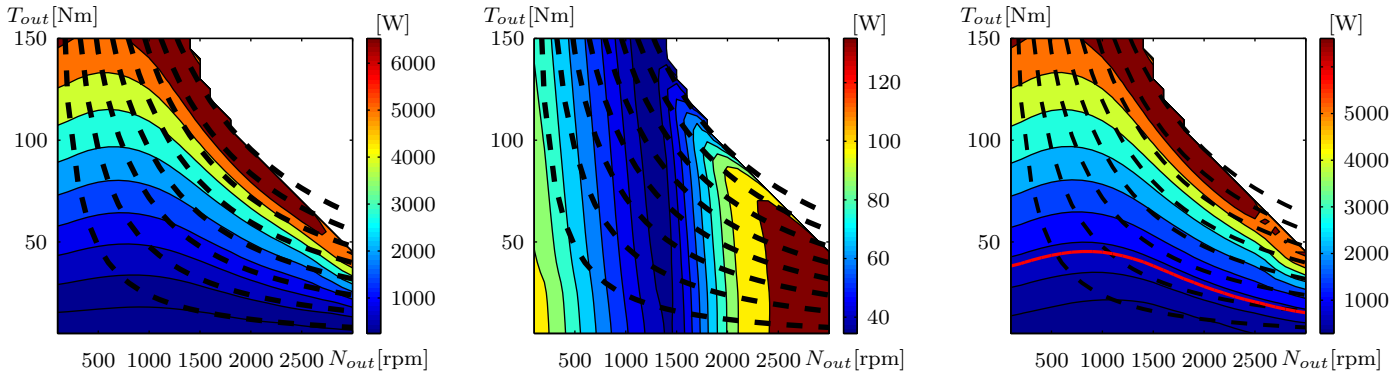

(a) copper losses **(b)** iron losses **(c)** total losses

Figure 7.18: Losses in function of operating point (9 kW IM-based EVT, moving stator)

7.3 Comparison of classical and inverted topologies

In the previous and this chapter, a geometric and an operating analysis is made of the 9 kW-based EVT. Although, on the first sight, the potential advantage of the inverted topology was estimated large, it seems out of the previous discussion that the two topologies are competing in performance. Chapter 6 shows that the optimal geometry is totally different if the function of the stator and rotor is inverted. Moreover, section 6.3, concludes that the efficiency of the inverted topology is less dependent on the geometrical parameters. In this chapter, it is concluded that the operating efficiency is increased by 2 % for the inverted design. Moreover, due to lower losses in both stator and rotor, the device is capable to transfer more power compared to its classical equivalent. At $N_{out} = 2000$ rpm, the maximal output power yields 20 kW, whereas previously the EVT was limited to 12.5 kW. Based in this remarks it is concluded that the inverted topology is more suited for applications which require high transient power in the overdrive region. In

automotive application, this is the case when one wants to accelerate fast at relatively high speed. For off-highway applications, the advantage is likely not to be used as mostly only high power is required at low speed.

Chapter 8

An EVT as a replacement of a Dana-Spicer torque converter

Chapter 9

Concluding remarks

9.1 Conclusion

The design of an electrical variable transmission was considered in this work. The first part of this study was dedicated to transmission systems. A broad range of transmission systems was studied, which resulted in a detailed overview of their working principles, advantages and disadvantages. It was concluded that continuous variable transmission systems have several advantages over conventional gearbox systems, including: a broader range of transmission ratio and, thus, a more optimal use of the ICE. As emphasised in Chapter 2, this leads to tremendous fuel savings. Moreover, power-split transmission enable to overcome some of the inherent disadvantages of CVT systems. The power-split allows on the one side to extend the operating region of the CVT. On the other side, it allows to enhance the transmission's efficiency, since a highly efficient mechanical power path is added.

Section 2.3 discussed several PS-CVT example systems focussing on hydraulic variators. Both the Fendt Vario and the Dana Rexroth HVT were described. It was shown that output-coupled as well as input-coupled PS-CVT systems are already present on the market. The choice of the topology is mainly dependent on the application. Output-coupled systems allow a complete shiftless transmission system, but require high power variable units. On the other hand, the power through the input-coupled PS-CVT system is much lower and thus the size of the variable units is decreased. However, this advantage is weakened due to the need of an additional gearbox in the transmission system.

Chapter 3 analysed several electromagnetic PS-CVT systems. Advantages of these kind of power-split transmissions over others include: very high efficiency of the electrical devices, no maintenance of hydraulic components and immense steering flexibility. The chapter also discussed the induction machine based EVT which was studied in this work. Although the IM-based EVT requires sliprings on the rotor, it requires only two airgaps which is the principal advantage over other EVT system. Moreover, cage systems are relatively cheap and robust compared to their PM equivalents.

The consequent chapters were dedicated to a FE analysis of the IM-based EVT. After a short introduction to finite element modelling, an overview of several studies was given, together with some modelling principles. By means of the gathered information, a coupled-circuit finite elements

model was composed in Chapter 5. The geometry was parametrized such that different geometrical parameters could be studied.

Chapters 6 and 7 described a geometrical optimization and operational analysis of a 9 kW IM-based EVT. It was concluded that both fixed and moving stator topologies have several benefits. The fixed stator topology has a simple design and is compact from mechanical point of view, since no additional casting is required. On the other hand, the use of the moving stator topology increases the electromagnetic efficiency of the device by a few percent. Moreover, the geometrical dependency of the efficiency is reduced and the electromagnetic power limit is increased by 20 %.

In Chapter 8, the feasibility of an electrical torque converter was studied. In the first part of the chapter the geometry was optimised. The outer dimensions of the EVT were chosen similar to a 250kW Dana torque converter. It was concluded that the optimal geometries of both fixed and moving stator topologies have an electromagnetic efficiency of about 95 %. Note that in this simulation some approximations were made. In the first place, three dimensional effects such as end-winding leakage were neglected. Secondly, skin effects and eddy currents in the iron core were not included in the simulations. And finally, ventilation and mechanical losses were neglected. Consequently, the total efficiency of the EVT could be a few percent lower.

In the second part of the chapter an operating analysis was performed including the optimal powerline of an ICE. It was concluded that there is only a small operating difference between the fixed and moving stator topologies. Unlike the smaller EVT studied in Chapter 7, the power transfer of the EVT in this chapter is not limited by the device itself. Due to the torque limit of the ICE, losses do not increase as fast as in a constant speed situation. Therefore, the maximum power transmitted by the transmission system is limited by the ICE. On the other hand, the lower losses in the inverted topology cause an increase by 20 % of the rated power to 120 kW for an air-cooled device. In practice, other cooling methods are possible as well. Although cooling methods were not studied in this paper, the rated power could be increased to more than 250 kW if an appropriate water/oil cooling system is designed. Since the rated power of the reference hydraulic torque converter is 250 kW as well, an EVT with similar dimensions is able to transfer the same amount of power. Moreover, it was concluded that the power size of the converters is only half of the power size of a serial electrical machine connection.

In the last part of the chapter, the electromagnetic torque converter was integrated in an existing transmission system. It was shown that even without changes to the gearbox, the operation of the EVT is limited to the very high efficiency region. The global efficiency of the torque converter has increased by 10 % due to the very high efficiency of the electrical machine. Moreover, since the EVT enables to reduce speed at partial load, the fuel consumption can be significantly reduced. In the studied acceleration curve, the reduction counts for 20 %. Moreover, at the vehicle's top speed, fuel savings are even higher due to the large efficiency difference between the electric and hydraulic torque converters at partial load.

Overall, it was concluded that an electrical torque converter is a very feasible adaptation for off-highway transmission systems. The obtained fuel savings are competing with the Dana Rexroth

HVT. The main advantages of an electrical system over a hydraulic system are:

- Increased efficiency of the electrical device;
- Control flexibility;
- Very fast torque response time;
- No hydraulic leakage;
- Compactness.

The main concerns towards the maximal power that can be transmitted are related to heat dissipation. Since this was not the subject of this master thesis, a more detailed study is required to investigate the thermal power limit.

9.2 Recommendations for future research

This work focused on the electromagnetic design of induction machine based EVT only. The entire design of the machine requires a thermal and mechanical study as well.

The mechanical issues are mainly caused by construction limits of the interrotor. It was shown in Chapter 6 that the optimal thickness of the interrotor is only 10 mm for a rated torque transfer of 25 Nm. Furthermore, the double rotor induction machine requires very good bearings to reach the required small airgap widths. Additionally, next to the electromagnetic losses, mechanical losses in the bearings due to friction and ventilation losses in the machine due the cooling system should be included in the overall performance of the EVT.

The thermal design of the machine is an important issue as well. If the power losses are not sufficiently conveyed to the surroundings of the machine, local temperature spikes affect the electromagnetic performance as well as the mechanical properties of the machine. **??** concluded that an air-cooling system may not provide sufficient cooling potential to cover the full operating range of the EVT. Especially during low speed operation, the electrical losses are considerably higher compared to an induction machine of the same size. The thermal design has to take into account different heat transport mechanisms: conduction, convection and radiation. In particular, heat convection in the moving stator topology is possibly difficult.

Also in the electromagnetic design, there are still many possibilities for improvement. As this work focused on a feasibility study, not all geometrical parameters were studied. Future research should include other design factors such as: airgap width, teeth thickness, yoke hight and so on. Due to the development of a parametrized finite element model in the context of this master thesis, the model can easily be adapted to include other geometrical parameters. Moreover, a scaling option was

integrated in the program. The option enables to investigate a very large range of different machine sizes. Additionally, not only geometrical parameters can be changed, also operating constraints, such as the optimal powerline of an ICE, are easily included into the model. Finally, although a transient study is not performed in this research, the model was constructed in a way that a time-dependent analysis is possible as well.

Concluding, the research possibilities based on presented FE model, developed in the framework of this master thesis, are immense and much more results can be obtained in the future than presented here.

Bibliography

Abdel-Razek, AA et al. (1981). "The calculation of electromagnetic torque in saturated electric machines within combined numerical and analytical solutions of the field equations". In: *Magnetics, IEEE Transactions on* 17.6, pp. 3250–3252.

Andersen, O.W. (2002). "Finite Element Analysis of Induction Motors". In: *International Conference on Electrical Machines*. Bruges: ICEM.

Arkkio, Antero et al. (1987). *Analysis of induction motors based on the numerical solution of the magnetic field and circuit equations*. Helsinki University of Technology.

Backx, PW (2008). *Prototype Testing of the Electric Variable Transmission*.

Beachley, N.H. and A.A. Frank (1979). *Continuously variable transmissions: theory and practice*. California Univ., Livermore (USA). DOI: 10.2172/5529813. URL: http://www.osti.gov/scitech/servlets/purl/5529813.

Belmans, Ronnie, R De Weerdt, and E Tuinman (1993). "Combining field analysis techniques and macroscopic parameter simulation for describing the behaviour of medium sized squirrel-cage induction motors fed with an arbitrary voltage". In: *Power Electronics and Applications, 1993., Fifth European Conference on*. IET, pp. 413–418.

Bertotti, Giorgio (1998). *Hysteresis in magnetism: for physicists, materials scientists, and engineers*. Academic press.

Boglietti, Aldo et al. (2011). "Induction motor design methodology based on rotor diameter progressive growth". In: *Energy Conversion Congress and Exposition (ECCE), 2011 IEEE*. IEEE, pp. 3104–3111.

Bonsen, Bram et al. (2003). "Analysis of slip in a continuously variable transmission". In: *ASME 2003 International Mechanical Engineering Congress and Exposition*. American Society of Mechanical Engineers, pp. 995–1000.

Brown, J.E., K.P. Kovacs, and P. Vas (1983). "A Method of Including the Effects of Main Flux Path Saturation in the Generalized Equations of A.C. Machines". In: *Power Apparatus and Systems, IEEE Transactions on* PAS-102.1, pp. 96–103. ISSN: 0018-9510. DOI: 10.1109/TPAS.1983.318003.

Chen, Li et al. (2011). "Design and analysis of an electrical variable transmission for a series–parallel hybrid electric vehicle". In: *Vehicular Technology, IEEE Transactions on* 60, pp. 2354–2363.

Chitroju, Rathna (2009). "Improved performance characteristics of induction machines with non-skewed symmetrical rotor slots". Licentiate Thesis. SE-100 44 Stockholm, Sweden: Royal Institute of Technology (KTH).

Dolinar, Drago et al. (1997). "Calculation of two-axis induction motor model parameters using finite elements". In: *Energy Conversion, IEEE Transactions on* 12.2, pp. 133–142.

Dolinar, Drago, Gorazd Stumberger, and Bojan Grcar (1998). "Calculation of the linear induction motor model parameters using finite elements". In: *Magnetics, IEEE Transactions on* 34.5, pp. 3640–3643.

Druant, Joachim et al. (2014). "Modeling and control of an induction machine based electric variable transmission". eng. In: *Young Researchers Symposium, Proceedings*. Ghent, Belgium, p. 5.

— (2015). "Field Oriented Control for an Induction Machine Based Electrical Variable Transmission". eng. In: *IEEE Transactions on Vehicular Technology [submitted]*. Ghent, Belgium.

Duan, Yao and Ronald G Harley (2011). "A novel method for multiobjective design and optimization of three phase induction machines". In: *Industry Applications, IEEE Transactions on* 47.4, pp. 1707–1715.

Escarela-Perez, R, E Melgoza, and E Campero-Littlewood (2008). "Time-Harmonic Modeling of Squirrel-Cage Induction Motors: A Circuit-Field Coupled Approach". In: *Proceedings of the COMSOL Conference, Boston*.

Faiz, Jawad et al. (2002). "A complete lumped equivalent circuit of three-phase squirrel-cage induction motors using two-dimensional finite-elements technique". In: *Energy Conversion, IEEE Transactions on* 17.3, pp. 363–367.

Fu, WN, SL Ho, and Ho-ching Chris Wong (2001). "Design and analysis of practical induction motors". In: *Magnetics, IEEE Transactions on* 37.5, pp. 3663–3667.

Gerling, Dieter (2005). "Comparison of Different FE Calculation Methods for the Electromagnetic Torque of PM Machines". In: *NAFEMS Seminar. Numerical Simulations of Electromechanical Systems*.

GmbH, AGCO (2010). *The 200 Vario: true greatness in operation*. Brochure. URL: `http://www.fendt.com/int/pdf/10057700_FE_200_GB_Inter.pdf`.

Gyimesi, I and Dale Ostergaard (1999). "Inductance computation by incremental finite element analysis". In: *Magnetics, IEEE Transactions on* 35.3, pp. 1119–1122.

Hanafy, Hanafy Hassan, Tamer Mamdouh Abdo, and Amr Amin Adly (2014). "2D finite element analysis and force calculations for induction motors with broken bars". In: *Ain Shams Engineering Journal* 5.2, pp. 421–431.

He, Yi-Kang and T.A. Lipo (1984). "Computer Simulation of an Induction Machine with Spatially Dependent Saturation". In: *Power Apparatus and Systems, IEEE Transactions on* PAS-103.4, pp. 707–714. ISSN: 0018-9510. DOI: `10.1109/TPAS.1984.318316`.

Hoeijmakers, Martin J and Marcel Rondel (2004). "The electrical variable transmission in a city bus". In: *Power Electronics Specialists Conference, 2004. PESC 04. 2004 IEEE 35th Annual*. Vol. 4. IEEE, pp. 2773–2778.

Hoeijmakers, Martin J and Jan A Ferreira (2006). "The electric variable transmission". In: *Industry Applications, IEEE Transactions on* 42, pp. 1092–1100.

Honsinger, Vernon B (1959). "Theory of end-winding leakage reactance". In: *Power Apparatus and Systems, Part III. Transactions of the American Institute of Electrical Engineers* 78.3, pp. 417–424.

Hsu, You-Chiuan, Min-Fu Hsieh, and Richard A McMahon (2009). "A general design method for electric machines using magnetic circuit model considering the flux saturation problem". In: *Power Electronics and Drive Systems, 2009. PEDS 2009. International Conference on*. IEEE, pp. 625–630.

Huang, Surong et al. (1998). "A general approach to sizing and power density equations for comparison of electrical machines". In: *Industry Applications, IEEE Transactions on* 34.1, pp. 92–97.

Ide, K et al. (1999). "Analysis of saturated synchronous reactances of large turbine generator by considering cross-magnetizing reactances using finite elements". In: *Energy Conversion, IEEE Transactions on* 14.1, pp. 66–71.

Idoughi, L. et al. (2011). "Thermal Model With Winding Homogenization and FIT Discretization for Stator Slot". In: *Magnetics, IEEE Transactions on* 47.12, pp. 4822–4826. ISSN: 0018-9464. DOI: 10.1109/TMAG.2011.2159013.

Ito, M. et al. (1981). "Analytical Model for Magnetic Field Analysis of Induction Motor Performance". In: *Power Apparatus and Systems, IEEE Transactions on* PAS-100.11, pp. 4582–4590. ISSN: 0018-9510. DOI: 10.1109/TPAS.1981.316798.

Jianhui, Hu, Zou Jibin, and Liang Weiyan (2003). "Finite element calculation of the saturation DQ-axes inductance for a direct drive PM synchronous motor considering cross-magnetization". In: *Power Electronics and Drive Systems, 2003. PEDS 2003. The Fifth International Conference on*. Vol. 1. IEEE, pp. 677–681.

Kabashima, Takefumi, Atsushi Kawahara, and Tadahiko Goto (1988). "Force calculation using magnetizing currents". In: *Magnetics, IEEE Transactions on* 24.1, pp. 451–454.

Kank, A, GB Kumbhar, and SV Kulkarni (2006). "Coupled magneto-mechanical field computations". In: *Power Electronics, Drives and Energy Systems, 2006. PEDES'06. International Conference on*. IEEE, pp. 1–4.

Kautzmann, Timo et al. (2010). *Self-optimizing machine management*. Institute for Mobile Machines, Karlsruhe Institute of Technology (KIT).

Knechtges, Herman J (2003). "Trends bei Traktoren und Transportfahrzeugen". In: *Landtechnik* 58.6, pp. 370–372.

Kowal, D. et al. (2011). "Influence of the Electrical Steel Grade on the Performance of the Direct-Drive and Single Stage Gearbox Permanent-Magnet Machine for Wind Energy Generation, Based on an Analytical Model". In: *Magnetics, IEEE Transactions on* 47.12, pp. 4781–4790. ISSN: 0018-9464. DOI: 10.1109/TMAG.2011.2158846.

Le Besnerais, Jean et al. (2009). "Optimal slot numbers for magnetic noise reduction in variable-speed induction motors". In: *Magnetics, IEEE Transactions on* 45.8, pp. 3131–3136.

Lee, Ki-sik et al. (1991). "Coupling finite elements and analytical solution in the airgap of electric machines". In: *Magnetics, IEEE Transactions on* 27.5, pp. 3955–3957.

Linares, P, V Méndez, and H Catalán (2010). "Design parameters for continuously variable power-split transmissions using planetaries with 3 active shafts". In: *Journal of Terramechanics* 47.5, pp. 323–335.

Liu, Yulong, SL Ho, and WN Fu (2014). "Novel Electrical Continuously Variable Transmission System and its Numerical Model". In: *Magnetics, IEEE Transactions on* 50, pp. 757–760.

Lu, Zhijian (1998). "Acceleration simulation of a vehicle with a continuously variable power split transmission". PhD thesis. West Virginia University.

Macor, Alarico and Antonio Rossetti (2011). "Optimization of hydro-mechanical power split transmissions". In: *Mechanism and Machine Theory* 46.12, pp. 1901–1919.

Marignetti, Fabrizio, V Delli Colli, and Yuri Coia (2008). "Design of axial flux PM synchronous machines through 3-D coupled electromagnetic thermal and fluid-dynamical finite-element analysis". In: *Industrial Electronics, IEEE Transactions on* 55.10, pp. 3591–3601.

Martinez, Javier, Anouar Belahcen, and Antero Arkkio (2012). "A 2d fem model for transient and fault analysis of induction machines". In: *Przeglad Elektrotechniczny* 88.7B, pp. 157–160.

Melkebeek, Jan (2013). *Electrical Drives (course text)*. Ghent University, EESA, EELAB.

— (2014). *Dynamics of Electrical Machines and Drives (course text)*. Ghent University, EESA, EELAB.

Mizia, J et al. (1988). "Finite element force calculation: comparison of methods for electric machines". In: *Magnetics, IEEE Transactions on* 24.1, pp. 447–450.

Munoz, Alfredo R and Thomas A Lipo (1999). "Complex vector model of the squirrel-cage induction machine including instantaneous rotor bar currents". In: *Industry Applications, IEEE Transactions on* 35.6, pp. 1332–1340.

Niu, Shuangxia, SL Ho, and WN Fu (2013). "Design of a novel electrical continuously variable transmission system based on harmonic spectra analysis of magnetic field". In: *Magnetics, IEEE Transactions on* 49, pp. 2161–2164.

Ojo, Joseph O and Thomas A Lipo (1989). "An improved model for saturated salient pole synchronous motors". In: *Energy Conversion, IEEE Transactions on* 4.1, pp. 135–142.

Polinder, Henk et al. (2003). "Modeling of a linear PM machine including magnetic saturation and end effects: Maximum force-to-current ratio". In: *Industry Applications, IEEE Transactions on* 39.6, pp. 1681–1688.

Popescu, Mircea (2006). "Prediction of the electromagnetic torque in synchronous machines through Maxwell stress harmonic filter (HFT) method". In: *Electrical Engineering* 89.2, pp. 117–125.

Renius, Karl Th and Rainer Resch (2005). *Continuously variable tractor transmissions*. American Society of Agricultrual Engineers.

Ryu, W. and H. Kim (2008). "CVT ratio control with consideration of CVT system loss". English. In: *International Journal of Automotive Technology* 9.4, pp. 459–465. URL: `http://search.proquest.com/docview/229680457?accountid=11077`.

Sasaki, S (1998). "Toyota's newly developed hybrid powertrain". In: *Power Semiconductor Devices and ICs, 1998. ISPSD 98. Proceedings of the 10th International Symposium on*. IEEE, pp. 17–22.

Shafai, Esfandiar et al. (1995). "Model of a continuously variable transmission". In: *Proceedings of IFAC 1st Workshop on Advances in Automotive Control, U. Kiencke and L. Guzzella, eds*, pp. 105–113.

Shima, Kazumasa, Kazumasa Ide, and Miyoshi Takahashi (2002). "Finite-element calculation of leakage inductances of a saturated salient-pole synchronous machine with damper circuits". In: *Energy Conversion, IEEE Transactions on* 17.4, pp. 463–470.

Silwal, Bishal et al. (2012). "Computation of eddy currents in a solid rotor induction machine with 2-D and 3-D FEM". MA thesis. Aalto Univercity.

Sprooten, Jonathan, Johan Gyselinck, and Jean-Claude Maun (2007). "Finite Element and Electrical Circuit Modelling of Faulty Induction Machines-Study of Internal Effects and Fault Detection". Master Thesis. Universite Libre de Bruxelles.

Sun, Chengyan et al. (2010). "Hydrostatic-Mechanical Power Split CVT". MA thesis. Tampere Univercity of Technology.

Sun, Xikai et al. (2009). "Optimal design of double-layer permanent magnet dual mechanical port machine for wind power application". In: *Magnetics, IEEE Transactions on* 45.10, pp. 4613–4616.

Sun, Xikai et al. (2013). "Application of electrical variable transmission in wind power generation system". In: *Industry Applications, IEEE Transactions on* 49, pp. 1299–1307.

Sundaram, M and P Navaneethan (2011). "On the Influence of Stator Slot shape on the Energy Conservation Associated with the Submersible Induction Motors". In: *American Journal of Applied Sciences* 8.4, pp. 393–399.

Tarnhuvud, T and K Reichert (1988). "Accuracy problems of force and torque calculation in FE-systems". In: *Magnetics, IEEE Transactions on* 24.1, pp. 443–446.

Trickey, P.H. (1936). "Induction motor resistance ring width". In: *Electrical Engineering* 55.2, pp. 144–150. ISSN: 0095-9197. DOI: 10.1109/EE.1936.6540574.

Vandevelde, Lieven and Jan Melkebeek (2014). *Electrical Machine Design (course text)*. Ghent University, EESA, EELAB.

Verhelst, Sebastiaan (2013). *Autotechniek (course text)*. Ghent University, Faculty of Engineering and Architecture.

Vukosavic, Slobodan N. (2013). *Electrical Machines*. English. New York: Springer. ISBN: 978-1-4614-0399-9.

Weili, Li et al. (2007). "Finite-element analysis of field distribution and characteristic performance of squirrel-cage induction motor with broken bars". In: *Magnetics, IEEE Transactions on* 43.4, pp. 1537–1540.

Williamson, S and JW Ralph (1983). "Finite-element analysis of an induction motor fed from a constant-voltage source". In: *IEE Proceedings B (Electric Power Applications)*. Vol. 130. IET, pp. 18–24.

Williamson, S and MC Begg (1985a). "Analysis of cage induction motors-A combined fields and circuits approach". In: *Magnetics, IEEE Transactions on* 21.6, pp. 2396–2399.

— (1985b). "Calculation of the bar resistance and leakage reactance of cage rotors with closed slots". In: *IEE Proceedings B (Electric Power Applications)*. Vol. 132. IET, pp. 125–132.

— (1986). "Calculation of the resistance of induction motor end rings". In: *IEE Proceedings B (Electric Power Applications)*. Vol. 133. IET, pp. 54–60.

Williamson, S, LH Lim, and AC Smith (1990). "Transient analysis of cage-induction motors using finite-elements". In: *Magnetics, IEEE Transactions on* 26.2, pp. 941–944.

Williamson, S and MJ Robinson (1991). "Calculation of cage induction motor equivalent circuit parameters using finite elements". In: *IEE Proceedings B (Electric Power Applications)*. Vol. 138. IET, pp. 264–276.

Xie, Ying (2012). *Investigation of Broken Rotor Bar Faults in Three-Phase Squirrel-Cage Induction Motors*. INTECH Open Access Publisher.

Yamazaki, Katsumi (1999). "Induction motor analysis considering both harmonics and end effects using combination of 2D and 3D finite element method". In: *Energy Conversion, IEEE Transactions on* 14.3, pp. 698–703.

Yasodha, S, K Ramesh, and P Ponmurugan (2012). "Evolutionary Multiobjetive Optimization Algorithms For Induction Motor Design–A Study". In: *International Journal of Emerging Technology and Advanced Engineering* 2.11.

Zhou, Ping et al. (1998). “Finite element analysis of induction motors based on computing detailed equivalent circuit parameters”. In: *Magnetics, IEEE Transactions on* 34.5, pp. 3499–3502.